Title
Stochastically forced zonal flows /

Author
Srinivasan, Kaushik

Publication Date
2013

UNIVERSITY OF CALIFORNIA, SAN DIEGO

Stochastically forced zonal flows

A dissertation submitted in partial satisfaction of the
requirements for the degree
Doctor of Philosophy

in

Oceanography

by

Kaushik Srinivasan

Committee in charge:

William R. Young, Chair
George Carnevale
Bruce Cornuelle
Dan Dubin
Stefan Llewellyn Smith
Rick Salmon

2013

The dissertation of Kaushik Srinivasan is approved, and it is acceptable in quality and form for publication on microfilm and electronically:

Chair

University of California, San Diego

2013

DEDICATION

To the memory of Gopal Krishna Srinivasan.

TABLE OF CONTENTS

Signature Page iii

Dedication iv

Table of Contents v

List of Figures viii

Acknowledgements xi

Vita, Publications, and Fields of Study xiii

Abstract of the Dissertation xiv

1 Introduction 1
  1.1 Reynolds stresses and eddy-driven zonal jets 1
  1.2 Zonal jets, eddies and Rossby waves 5
  1.3 Structure of forcing in the barotropic model 8
  1.4 Tracer diffusion due to eddies in a background mean flow 9

2 Zonostrophic instability 13
  2.1 Introduction 14
  2.2 The eddy-mean decomposition and quasilinear (QL) dynamics . . . 19
    2.2.1 Quasilinear (QL) dynamics 19
    2.2.2 Stochastic closure versus cumulant expansion 22
  2.3 Dynamics of correlations: CE2 23
    2.3.1 Correlation functions: kinematics 23
    2.3.2 Correlation functions: dynamics 24
    2.3.3 Collective coordinates 25
    2.3.4 The zonal mean flow equation 26
  2.4 Zonostrophic instability of a spatially homogeneous and isotropic base-state flow 26
    2.4.1 The spatially homogeneous basic state 26
    2.4.2 The dispersion relation of inviscid and isotropic flow 28
    2.4.3 Ring forcing 29
    2.4.4 Approximations to the neutral curve with large and small β_* 32
    2.4.5 The small wavenumber structure of the growth rate 33
  2.5 Isotropy and zero eddy viscosity 34
    2.5.1 A solution of the correlation equation 35
    2.5.2 The Reynolds stresses 36
    2.5.3 The kinetic energy density 37
    2.5.4 Discussion 38

2.6 Zonation in QL and NL solutions 38
  2.6.1 The onset of zonation in NL and QL solutions 40
  2.6.2 Zonostrophically stable NL solutions 41
  2.6.3 The jet scale 43
  2.6.4 The small drag regime 46
  2.6.5 Discussion of the eddy-eddy nonlinearity 48
2.7 Discussion and conclusion 49
2.A Implementation of the random forcing $\xi(\boldsymbol{x}, t)$ 50
2.B Rapid temporal decorrelation: derivation of (2.25) 52
2.C Derivation of the dispersion relation (2.45) 53
2.D The function $Q(\chi, n)$ 56
2.E The neutral curve 57
  2.E.1 Approximation of the marginal curve, $\beta \gg 1$ and $\chi_0 \ll 1$ . . 57
  2.E.2 Approximation of the marginal curve, $\beta \ll 1$ and $\chi_0 \gg 1$ . . 58
  2.E.3 The small-m expansion 59

3 Meridionally drifting zonal jets on the β-plane 60
3.1 Introduction 60
3.2 Statistical properties of the forcing 62
  3.2.1 Exchange symmetry 63
  3.2.2 Mirror symmetry 63
  3.2.3 The anisotropic ring forcing 64
3.3 Numerical solutions of the barotropic vorticity equation 66
  3.3.1 Forcing with broken mirror-symmetry: Drifting jets 66
  3.3.2 The effect of varying μ_* and β_* 68
  3.3.3 Mirror-symmetric forcing 70
3.4 Quasi-linear dynamics and a CE2-based theory 72
  3.4.1 CE2 theory for a slowly varying mean flow 73
3.5 Conclusion 78
3.A The perturbation expansion 79
3.B Solution of perturbed equation by iteration 81

4 Reynolds stress and eddy diffusivity of β-plane shear flows 83
4.1 Introduction 84
4.2 Correlation functions and statistical symmetries 86
  4.2.1 A remark on scale separation and homogeneity in y 87
  4.2.2 Statistical properties of the solution 87
  4.2.3 Exchange symmetries 88
  4.2.4 Reflexion symmetry 88
  4.2.5 The stochastic forcing 89
4.3 Statistical Galilean invariance 89
4.4 Power integrals 91
  4.4.1 Enstrophy 91

- 4.4.2 Energy . . . 92
- 4.4.3 Tracer variance . . . 92
- 4.4.4 Covariance of tracer and vorticity . . . 93
- 4.4.5 A bound on the Reynolds stress . . . 93
- 4.4.6 Bounds on the eddy diffusivity . . . 93

4.5 Reynolds stress and anisotropy . . . 94
- 4.5.1 Reynolds stress . . . 95
- 4.5.2 The vorticity flux of a slowly varying mean flow . . . 97
- 4.5.3 Eddy kinetic energy and enstrophy . . . 97
- 4.5.4 Velocity anisotropy . . . 99
- 4.5.5 Tenacity of isotropy . . . 100

4.6 The eddy diffusivity $\kappa_{\mathrm{e}}(\alpha_c, \beta, \gamma, \mu)$ . . . 100
- 4.6.1 The case $\gamma = \beta = 0$ . . . 101
- 4.6.2 The suppression factor, S . . . 102
- 4.6.3 The case $\gamma = 0$ . . . 102
- 4.6.4 Comparison with Klocker, Ferrari & LaCasce (2012) . . . 104
- 4.6.5 The case $\beta = 0$ . . . 106
- 4.6.6 Large shear . . . 107

4.7 Discussion and conclusion . . . 110

4.A A bound on eddy diffusivity . . . 112

4.B Details of the $\mathcal{Z}$ solution . . . 113
- 4.B.1 A polar representation of $\tilde{\Xi}$ . . . 113
- 4.B.2 The Reynolds stress . . . 113
- 4.B.3 Anisotropy . . . 114
- 4.B.4 Two angular integrals . . . 115

4.C Properties of F_1 and F_2 . . . 116

4.D Details of the solution for κ_{e} . . . 116

4.E Tracer diffusivity in the limit $\gamma/\mu \to \infty$ . . . 118

References . . . 120

LIST OF FIGURES

Figure 1.1: A schematic depicting the formation of the mid-latitude eddy driven jet from *Vallis* [2006]. 2
Figure 1.2: Snapshots of the vorticity field obtained from equilibriated runs of the forced barotropic vorticity equation, overlaid by the instantaneous zonal-mean velocity 3
Figure 1.3: The zonal mean flow of the jupiter calculated from NASA's *Cassini* mission. From *Heimpel et al.* [2005]. 5
Figure 1.4: Two dimensional spectra of equilibriated runs of the barotropic vorticity equation from Chapter 2. 7
Figure 1.5: (a) Noodle modes: Snapshot of upper layer potential vorticity showing initial stages of evolution of baroclinic instability for a background with zonally oriented vertical shear (b) The same but for a flow whose vertical shear is aligned at an angle $\pi/4$. . 9
Figure 1.6: (a) Snapshot of equilibrated vorticity from a zonal jet run for $\mu_* = 0.00182$ and $\beta_* = 1$ from Chapter 2 with overlaid zonal-mean velocity (thick white line). (b) The corresponding snapshot of the passive scalar field. 11

Figure 2.1: Nonlinear (NL) zonal jets. 16
Figure 2.2: Quasilinear (QL) zonal jets. 17
Figure 2.3: (a) Hovmöller diagram of the zonal mean velocity $U(y,t)$ obtained by solution of the full nonlinear (NL) system in (2.3). . . 20
Figure 2.4: The growth rate s as a function of m for $\mu_* = 0.15$ and five values of β_* indicated on the curves. 31
Figure 2.5: (a) The critical curve, $\mu_*^{\mathrm{c}}(\beta_*)$ (solid line); linear zonostrophic instability occurs in the region below the critical curve. (b) The wavenumber on the critical curve, $m^{\mathrm{c}}(\beta_*)$ (solid line) i.e., the most linearly unstable wavenumber. 32
Figure 2.6: The time-averaged zonal mean energy fraction $\langle \mathrm{zmf} \rangle$ as a function of μ_*, with β_* fixed as indicated in the bottom right corner of each panel. QL simulations are indicated by $\circ$ and NL solutions by $*$. 39
Figure 2.7: Snapshots of the vorticity $\zeta(x,y,t)$ with overlaid zonally averaged vorticity $-U_y(y,t)$ (solid white curve) with (a) $\mu_* = 0.309$ and, (b) $\mu_* = 0.0545$. 41
Figure 2.8: The upper panels show the zonal spectrum, $E_{\mathrm{Z}}(k_y/k_f)$, for QL and NL solutions with $\beta_* = 1$. The lower panels show the residual spectrum $E_{\mathrm{R}}(k/k_f)$, defined as the angularly averaged spectrum after removal of the "zonal modes" with $k_x = 0$. . . . 42
Figure 2.9: A summary of zonal wavenumbers (jet scales) for solutions with (a) $\beta_* = 0.5$ and (b) $\beta_* = 1$. 44

Figure 2.10: Hovmöller diagrams for the (a) NL and (b) QL runs with β_*=1.0 and $\mu_* = 0.0545$. 45
Figure 2.11: Comparison of zonal mean velocity profiles of the $\beta_* = 1$ NL and QL runs in Figures 2.1 and 2.2. 47
Figure 2.12: Comparison of time-averaged zonal-mean velocity profiles (thin lines) of QL runs. 49
Figure 2.13: Comparison of the ring forcing, $\delta k \to 0$ (solid line) and the narrow-band forcing with $\delta k = k_f/4$ (dashed line). 52

Figure 3.1: The left panels show the anisotropic ring correlation function Ξ in (3.14) and the right panels show corresponding snapshots of the forcing ξ. 65
Figure 3.2: Turbulent drifting jets: Hovmöller diagrams of the zonal-mean velocity when the forcing breaks mirror symmetry. 67
Figure 3.3: Hovmöller diagrams of the zonal-mean velocity when the forcing breaks mirror symmetry as the drag parameter is varied. Here $\alpha_c = 0$ and $\alpha_s = 1$. 68
Figure 3.4: Hovmöller diagrams of the zonal-mean velocity when the forcing breaks mirror symmetry as the drag parameter is varied. 70
Figure 3.5: (a) Non-dimensional jet-drift at fixed $\beta_* = 1$, as a function of μ_* for the non-linear (filled-circles) and quasi-linear runs (crosses). 71
Figure 3.6: (a) Snapshot of the vorticity $\zeta(x, y)$, obtained from the nonlinear barotropic model at $2\mu t = 50$ for $\alpha_c = 0$, $\alpha_s = 1$, $\beta_* = 1$, $\mu_* = 0.0046$ corresponding to the run shown in Figure 3.3 (b). (b) The same but obtained from the quasi-linear model. 72
Figure 3.7: Hovmöller diagrams of the zonal-mean velocity subject to a mirror symmetric forcing ($\alpha_s = 0$) and two extremal values of α_c, (a) $\alpha_c = -1$, (b) $\alpha_c = 1$. The flow parameters are $\mu_* = 0.036$ and $\beta_* = 1$. 72
Figure 3.8: Quasi-linear drifting jets: Hovmöller diagrams of the quasi-linear zonal-mean velocity when the forcing breaks mirror symmetry. 74

Figure 4.1: The left panels show the anisotropic ring correlation function Ξ in (4.19) and the right panels show corresponding snapshots of the forcing ξ. Panels (a) and (d) show $\alpha_c = -1$; (b) and (e) show the isotropic case $\alpha_c = 0$; panels (c) and (f) show $\alpha_c = +1$. 90
Figure 4.2: F_1 in (4.42) as a function of the non-dimensional shear γ/μ. The dashed curve is the approximation $F_1(\gamma/\mu) = 4\mu/\gamma + O(\mu/\gamma)^2$. 96
Figure 4.3: (a) The non-dimensional eddy kinetic energy as a function of γ/μ, calculated from (4.48). (b) The non-dimensional meridional velocity variance as a function of γ/μ. 98

Figure 4.4: (a) The function $F_2(\gamma/\mu)$ defined in (4.50). The dashed curve is the asymptotic approximation $(16\mu^2/\gamma^2)[\ln(\gamma/4\mu) - \gamma_E]$, where $\gamma_E = 0.57721\cdots$ is Euler's constant. (b) The index aniso in (4.51), with $\alpha = -1$, 0 and 1. 99
Figure 4.5: (a) The non-dimensional $\gamma = 0$ tracer diffusivity in (4.66) as a function of $\tilde{\beta} = \beta/(2\mu k_f)$. (b) The suppression factor, S defined in (4.69). 103
Figure 4.6: (a) The non-dimensional tracer diffusivity as a function of γ/μ with β=0 and different values of α. (b) The corresponding suppression factor defined in (4.63). 107
Figure 4.7: (a) The function $B_1(\pi\tilde{\beta})$ given in (4.83) shown as a function of $\tilde{\beta}$. The large $\tilde{\beta}$ approximation is the dashed curve. 108
Figure 4.8: (a) The numerically computed non-dimensional tracer diffusivity as a function of γ/μ, with different values of β, and isotropic forcing $\alpha = 0$. 109

ACKNOWLEDGEMENTS

Bill Young has been an awesome thesis advisor and a very positive influence over my research attitudes formed during the course of the my PhD program. I am extremely grateful for his patience, persistence and instruction over a wide very variety of scientific subjects. Thanks to him, my general book-keeping and scientific writing have also come a long way, especially with matters concerning the judicious use (or lack thereof) of pronouns and adverbs!

Rick Salmon was a constant source of inspiration and I am greatly indebted to him for his support and faith in my abilities, that I rarely shared. His physical insights and unique perspectives have significantly added to this dissertation and my scientific perspectives in general. Entertaining and useful discussions with George Carnevale were also of great value. I also wish to thank the rest of my committee: Bruce Cornuelle, Stefan Llewellyn Smith and Dan Dubin.

The assistance of Dana Dahlbo and the SIO grad office was invaluable, especially considering my tendency for last-minute mayhem. Phil Moses was always around to address any computing issues I had and for myriad conversations on the California outdoors.

I have had the pleasure of making a lot of wonderful friends during my time here at Scripps. Dian, Peter, Anais, San, Gordy, Yvonne, Aneesh, Donata and Ben have been awesome company in times of mirth and a balm in times of woe. Its hard for me to overstate the value of their companionship in the successful completion of this dissertation.

Maria and I shared a lot of wonderful moments over the years and even though we stand apart now, her love and support was one of the pillars of my happiness during my time at Scripps.

My mum, Gita and sister, Supraja are an important fixture in my life and I would not have made it this far without them, and I owe any success, albeit minor, to them.

Chapter 2, in full, is a reproduction of the material as it appears in *Srinivasan and Young* [2012], *J. Atmos. Sci,*, **69**, 1633. The dissertation author was

the primary investigator and author of this work.

Chapter 3 is currently being prepared for submission for publication of the material. The dissertation author was the primary investigator and author of this material. W.R Young supervised and directed this research.

Chapter 4 has been accepted for publication in the *Journal of Atmospheric Sciences*. The dissertation author was the primary investigator and author of this material. W.R Young supervised and directed this research.

VITA

2003	B.Tech. in Aerospace Engineering, Indian Institute of Technology Kanpur
2007-2013	Graduate Student Researcher Scripps Institution of Oceanography University of California, San Diego
2013	Ph.D. in Oceanography, University of California, San Diego

PUBLICATIONS

Srinivasan, Kaushik, and W. R. Young. “Zonostrophic instability.” *Journal of the Atmospheric sciences* **69** (2012), 1633-1656.

Srinivasan, Kaushik, and W. R. Young. “Reynolds stress and eddy diffusivity in β-plane shear flows.” *Journal of the Atmospheric sciences* (in press).

FIELDS OF STUDY

Major Field: Physical Oceanography

Studies in Applied Mathematics
Professors G. R. Ierley and W. R. Young

Studies in Fluid Dynamics and Turbulence
Professors C. D. Winant and R. Salmon

Studies in Geophysical Fluid Dynamics
Professors P. Cessi and R. Salmon

Studies in Linear and Nonlinear Waves
Professors M. C. Hendershott, and R. T. Guza

Studies in Data Analysis
Professors R. Pinkel, D. L. Rudnick, S. T. Gille

Studies in Physical Oceanography
Professors L. D. Talley, M. C. Hendershott, and D. Roemmich

ABSTRACT OF THE DISSERTATION

Stochastically forced zonal flows

by

Kaushik Srinivasan

Doctor of Philosophy in Oceanography

University of California, San Diego, 2013

William R. Young, Chair

This thesis investigates the dynamics of multiple zonal jets, that spontaneously emerge on the barotropic β-plane, driven by a homogenous and rapidly decorrelating forcing and damped by bottom drag. Decomposing the barotropic vorticity equation into the zonal-mean and eddy equations, and neglecting the eddy-eddy interactions, defines the quasi-linear (QL) system. Numerical solution of the QL system shows zonal jets with length scales comparable to jets obtained by solving the nonlinear (NL) system. Starting with the QL system, one can construct a deterministic equation for the evolution of the two-point single-time correlation function of the vorticity, from which one can obtain the Reynolds stress that drives the zonal mean flow. This deterministic system has an exact nonlinear solution, which is a homogenous eddy field with no jets. When the forcing is also isotropic

in space, we characterize the linear stability of this jetless solution by calculating the critical stability curve in the parameter space and successfully comparing this analytic result with numerical solutions of the QL system. But the critical drag required for the onset of NL zonostrophic instability is up to a factor of six smaller than that for QL zonostrophic instability.

The constraint of isotropic forcing is then relaxed and spatially anisotropic forcing is used to drive the jets. Meridionally drifting jets are observed whenever the forcing breaks an additional symmetry that we refer to as mirror, or reflexional symmetry. The magnitude of drift speed in our results shows a strong variation with both μ and β: while the drift speed decreases almost linearly with decreasing μ, it actually increases as β decreases. Similar drifting jets are also observed in QL, with the same direction (i.e. northward or southward) and similar magnitude as NL jet-drift. Starting from the laminar solution, and assuming a mean-flow that varies slowly with reference to the scale of the eddies, we obtain an approximate equation for the vorticity correlation function that is then solved perturbatively. The Reynolds stress of the pertubative solution can then be expressed as a function of the mean-flow and its y-derivatives. In particular, it is shown that as long as the forcing breaks mirror-symmetry, the Reynolds stress has a wave-like term, as a result of which the mean-flow is governed by a dispersive wave equation.

In a separate study, Reynolds stress induced by an anisotropically forced unbounded Couette flow with uniform shear γ, on a β-plane, is calculated in conjunction with the eddy diffusivity of a co-evolving passive tracer. The flow is damped by linear drag on a time scale μ^{-1}. The stochastic forcing is controlled by a parameter α, that characterizes whether eddies are elongated along the zonal direction ($\alpha < 0$), the meridional direction ($\alpha > 0$) or are isotropic ($\alpha = 0$). The Reynolds stress varies linearly with α and non-linearly and non-monotonically with γ; but the Reynolds stress is independent of β. For positive values of α, the Reynolds stress displays an “anti-frictional” effect (energy is transferred from the eddies to the mean flow) and a frictional effect for negative values of α. With $\gamma = \beta = 0$, the meridional tracer eddy diffusivity is $\overline{v'^2}/(2\mu)$, where v' is the meridional eddy velocity. In general, β and γ suppress the diffusivity below $\overline{v'^2}/(2\mu)$.

1 Introduction

Zonal flows and eddies are a dominant component of the large-scale circulation of terrestrial and planetary atmospheres and the Southern Ocean. In many cases eddy fluxes of heat and momentum generate mean flows, while in other examples, they regulate the strength, structure and variability of mean flows. The central aim of this dissertation is to construct simplified theories of eddy-mean flow interactions, and characterize the eddy fluxes of momentum and a passive scalar, under the paradigm of forced-dissipative barotropic β-plane flow. In Chapter 2, we introduce the idea of zonal jets as being an instability of an underlying two-dimensional homogenous turbulent flow and present an idealized statistical model and analytical solutions that are tested against a wide swath of numerical results. Chapter 3 analyzes a specific aspect of the variability of eddy-driven zonal jets, namely their slow meridional drift. In Chapter 4, we calculate the Reynolds stress of anisotropic eddies in a β-plane shear flow and show that the diffusivity of a passive scalar is suppressed by both the shear and β.

1.1 Reynolds stresses and eddy-driven zonal jets

While zonal flows and jets are ubiquitous in geophysical systems, only some examples are driven solely by the fluxes of turbulent eddies and waves. For example, though eddy fluxes significantly modify the sub-tropical jet in the upper troposphere, the existence of the jet is a consequence of temperature contrasts at the terminus of the Hadley cell [*Held*, 2000]. The Southern Ocean is largely driven by the mechanical action of westerly wind-stress applied at the surface. However, baroclinic instability generates eddies that are responsible for the formation of multiple jets with a high degree of spatial and temporal variability [*Sokolov and Rintoul*, 2007; *Thompson and Richards*, 2011]. The zonal flows in the atmospheres of giant planets (in our solar system Jupiter, Saturn, Uranus and Neptune) are likely to be eddy-driven because these planets are too far from the sun to be driven by equator-to-pole temperature contrasts [*Aurnou et al.*, 2007]. Further, the giant planets have very strong zonal jets [*Vasavada and Showman*, 2005; *Beebe*, 2005] (the peak mean zonal wind in Neptune is around 200 m/s) with a majority of the surface energy in the mean zonal-flow.

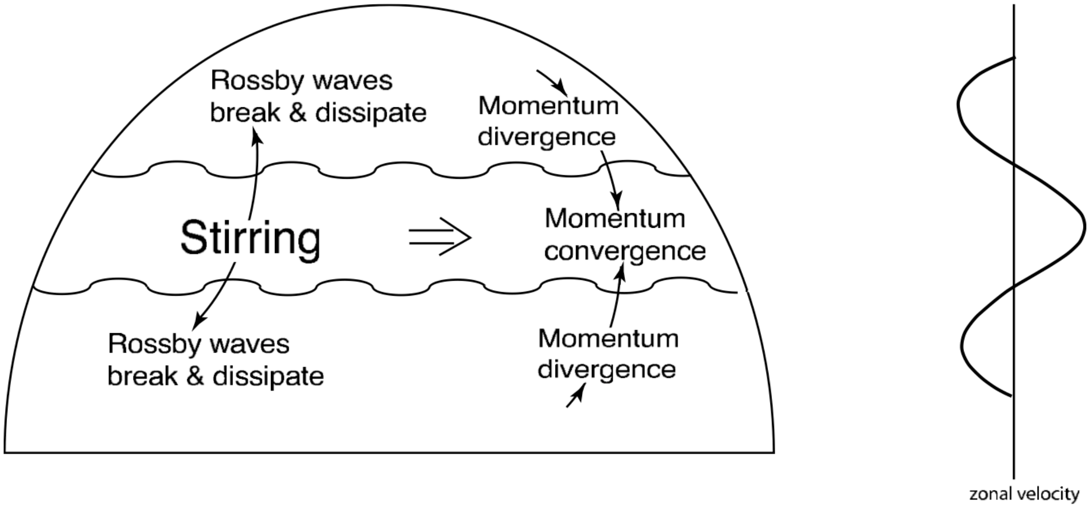

Figure 1.1: A schematic depicting the formation of the mid-latitude eddy driven jet from *Vallis* [2006]. Rossby waves (and eddies) generated due to baroclinic instability in the mid-latitude radiate outward, break and dissipate, and deposit momentum at the source region.

The surface westerly flow in the mid-latitude terrestrial atmosphere is perhaps one of the simplest examples of a zonal flow that is primarily generated by the action of eddy momentum fluxes (or Reynolds stresses) [*Hartmann*, 2007]. The schematic in Figure 1.1 (from *Vallis* [2006]) presents a simplified view of how the northern hemisphere westerlies are generated. The midlatitudes have a narrow baroclinic unstable zone that are also identifiable with the region of the storm tracks. Eddies formed due to baroclinic instability excite Rossby waves that propagate away from the source region, and undergo breaking and dissipation at the

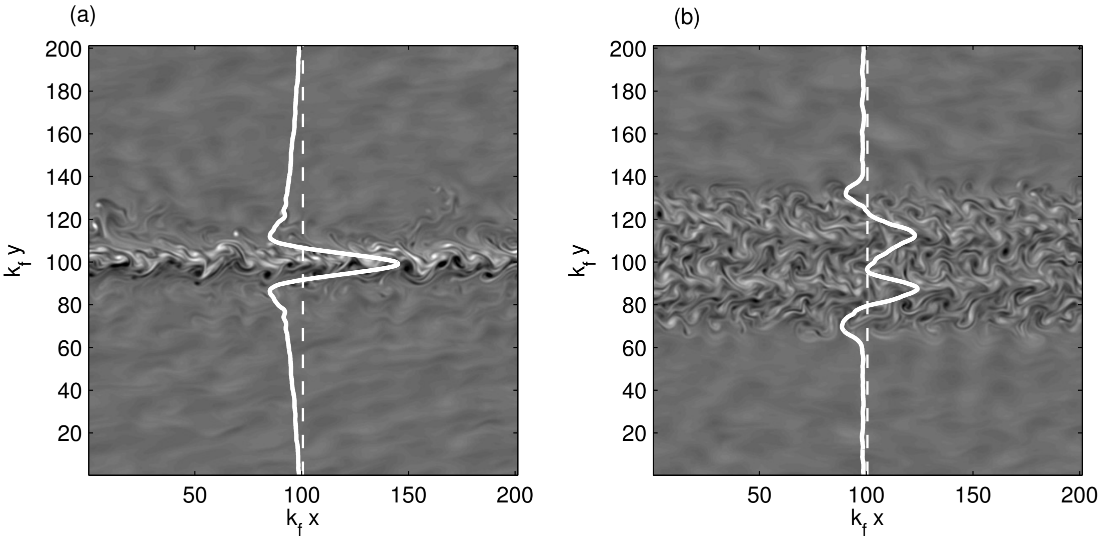

Figure 1.2: Snapshots of the vorticity field obtained from equilibriated runs of the forced barotropic vorticity equation, overlaid by the instantaneous zonal-mean velocity (thick white curves) relative to a zero level (dashed white lines) for the following two cases: (a) A numerical run on the barotropic β-plane that illustrates the basic jet generation mechanism shown in Figure 1.1. The narrow source region (between $k_f y = 96$ and $k_f y = 104$) is stirred by a random forcing, that models baroclinic eddies. (b) Emergence of an intrinsic length scale: As the source region expands in width (now between $k_f y = 80$ and $k_f y = 120$), multiple jets start to appear and the jet width no longer scales with the width of the stirred region.

so-called ‘critical’ latitudes. An easily derivable property of Rossby waves [*Held*, 2000; *Vallis*, 2006] is that the outward propagating Rossby waves converge momentum flux (or Reynolds stress), $\overline{u'v'}$, *into* the source region, thereby creating the eastward or westerly flow at the source region. This is a general result: convergence (or divergence) of Reynolds stresses are responsible for generation of zonal mean flows. This mechanism is illustrated clearly in Figure 1.2(a), which shows a numerical result obtained from solving the barotropic vorticity equation on the β-plane (the numerical approach is explained in detail in Chapter 2). The flow is stirred in a narrow source region by a random forcing, which also ends up being a region of high eddy-activity (like the atmospheric storm tracks). A strong eastward jet is seen in the source region with a width that corresponds to the width of the stirred zone. Outside the stirred region, westward flow exists to maintain momentum conservation, since the stirring does not add momentum to the fluid.

The picture gets considerably muddled when the width of the stirring region is increased and multiple jets start to emerge, as seen in Figure 1.2 (b). This is because an *intrinsic* length scale has now emerged in the system and the model and discussion surrounding Figure 1.1 no longer works. If the stirring region is expanded to cover the entire domain, a systematic pattern of eastward and slower westward jets emerges (see Figure 2.1 in Chapter 2). Similar results are seen in idealized general circulation models with planetary radius and rotation rate larger than that of the earth [*Schneider and Walker*, 2008; *Williams*, 2003; *O'Gorman and Schneider*, 2008]. These examples have wide zones of baroclinic instability and therefore display multiple zonal jets.

The atmospheres of giant planets are not driven by baroclinic instability but by a combination of moist shallow-convection in the cloud layer [*Gierasch et al.*, 2000; *Vasavada and Showman*, 2005; *Li et al.*, 2006] and possibly, deep convection from the metallic interior to the surface [*Heimpel et al.*, 2005; *Schneider and Liu*, 2009; *Showman et al.*, 2011]. Figure 1.3 is a plot of the zonal mean-flow constructed using observations from the *Cassini* mission [*Porco et al.*, 2003; *Vasavada and Showman*, 2005; *Heimpel et al.*, 2005] and a pattern of east-west jets flanking a strong equatorial super-rotating jet is clearly seen. Barotropic models have been used previously to understand Jovian jets [*Galperin et al.*, 2004, 2006], though their validity is contingent on deep convection in Jupiter [*Heimpel et al.*, 2005; *Showman et al.*, 2011; *Schneider and Liu*, 2009] being less important dynamically than shallow convection in the cloud layer. On the other hand, the atmospheres of Neptune and Uranus are shallow, as inferred from gravity measurements collected during the *Voyager* mission [*Kaspi et al.*, 2013] and barotropic models [*Galperin et al.*, 2004] are of value here.

For the barotropic model, starting from the pivotal work of *Rhines* [1975], numerous physical mechanisms have been proposed to explain the formation of multiple jets, their spacing and strucure, and we examine some of them in the

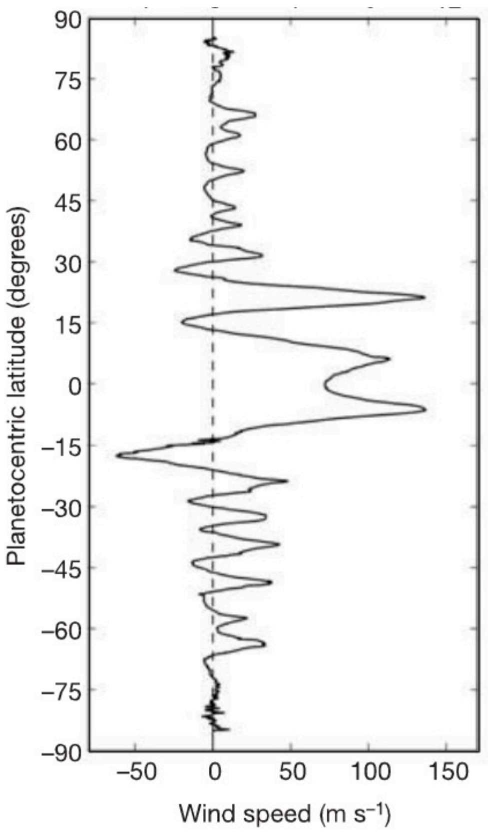

Figure 1.3: The zonal mean flow of the jupiter calculated from NASA's *Cassini* mission. From *Heimpel et al.* [2005].

next section.

1.2 Zonal jets, eddies and Rossby waves

The presence of differential rotation, due to the near-spherical shape of planets, or β-effect, is a basic requirement for the formation of large scale zonal jets. The interaction between Rossby waves (which only exist for non-zero β) and turbulent eddies is at the heart of most theories of jet formation. *Rhines* [1975] proposed a scaling for the jet width based on idea that jet formation occurred as consequence of a transition from turbulent eddies to waves. The small-scale driving agent generates eddies that grow larger as a consequence of the two-dimensional inverse cascade [*Kraichnan*, 1967]. When the eddies reach a particular scale, given by the Rhines wave number, k_{Rh}, the inverse cascade is halted and the eddies attain a wave-like character, which *Rhines* interprets as representing the jets. Based on this idea and a simple *ad hoc* balance between the advective ('eddies') and β ('waves') terms of the momentum equation, *Rhines* [1975] obtained an expression for the halting wavenumber,

$$k_{Rh} \sim \sqrt{\frac{\beta}{\mathcal{U}}}\,, \tag{1.1}$$

where $\mathcal{U}$ is a velocity scale that needs to be determined. For example, one possible choice of $\mathcal{U}$ suggested by *Danilov and Gurarie* [2004] and also used in Chapter 2 (upto a pre-factor of 2) is the root mean square velocity of the flow, V_{rms} (so that the flow kinetic energy is proportional to V_{rms}). If linear bottom friction is assumed to be the dominant dissipation mechanism, then the Rhines scale becomes

$$k_{Rh} \sim \beta^{1/2}\mu^{1/4}\varepsilon^{-1/4}\,, \tag{1.2}$$

where ε is the energy disspation rate of the system. *Vallis and Maltrud* [1993] proposed a mechanism for the anisotropization of two-dimensional turbulent flow on the β-plane and suggested that it also explained the origin of jets. Following along the lines of Rhines, they attempt to obtain the length scale (referred to as k_β) at which the *time-scales* of eddies and Rossby waves are the same: if the Rossby wave time scales are much faster, then eddies would be suppressed due to rapid de-correlation induced by the waves (also see *Salmon* [1998]). But since the Rossby wave frequency is highly anisotropic, the resulting halting scale has a dumbbell-like shape centered along the zonal wavenumber axis. *Vallis and Maltrud* found that eddy activity is indeed suppressed in the dumbbell and further speculated that the inverse cascade would make the spectrum increasingly concentrated along the meridional wavenumber axis (or equivalently, the zonal direction, in physical space) eventually leading to the formation of zonal jets.

For one set of barotropic numerical solutions from Chapter 2, this dumbbell shape is prominently seen along the zonal wavenumber axis in Figure 1.4 for all the figures marked 'turbulent' (1.4 (b) to (f)). The problem is that, while Figure 1.4(c) is turbulent and has the anisotropic dumbbell structure proposed by *Vallis and Maltrud* [1993], jets don't exist (the red high energy spots in (e) and (f) mark

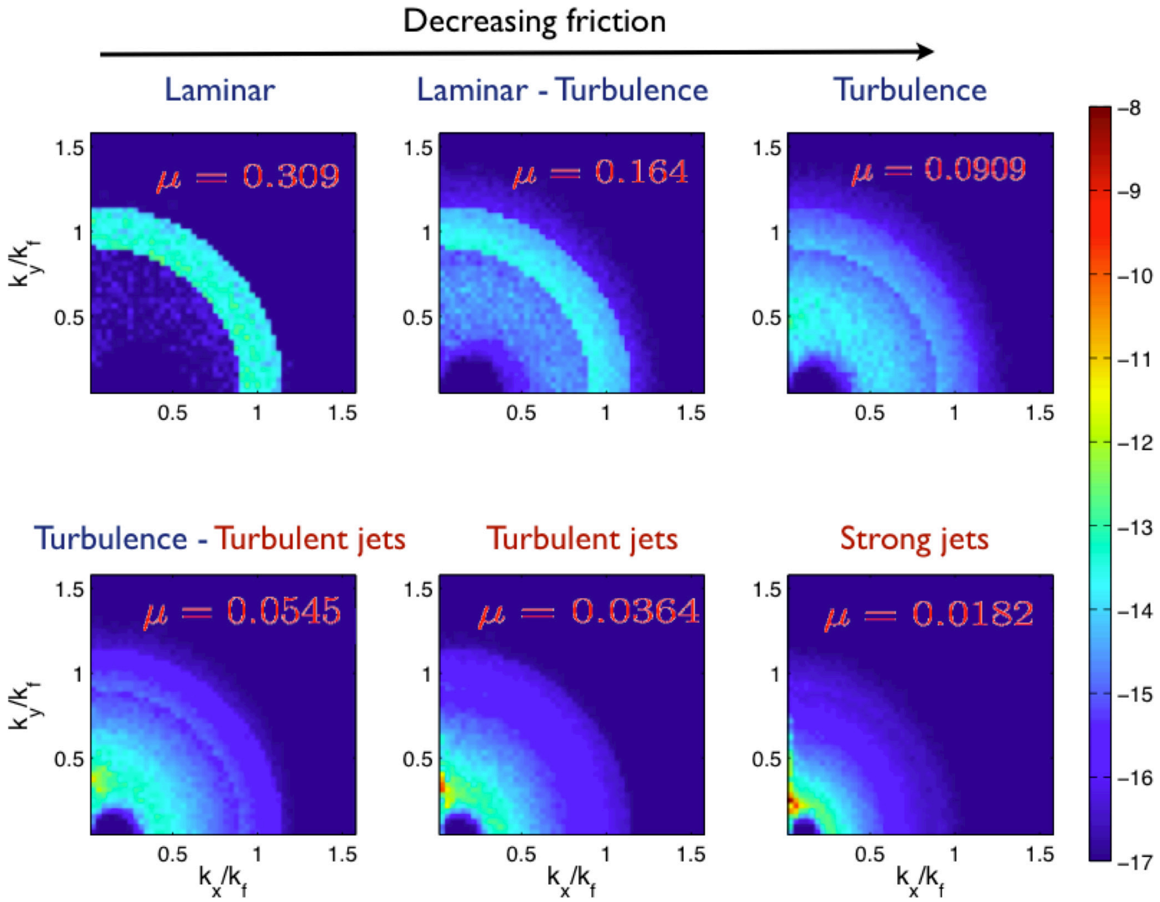

Figure 1.4: Two dimensional spectra of equilibriated runs of the barotropic vorticity equation from Chapter 2. The *Vallis and Maltrud* 'dumbell' is prominently seen on the abscissa of all the runs marked as 'turbulent'. The red spots in (d), (e) and (f) are the zonal jets and their meanders.

the jets). Thus the mechanism proposed by *Vallis and Maltrud* is an inadequate explanation for jet formation. In Chapter 2 we show that none of the mechanisms reviewed in this section can serve as a fundamental theory for jet formation, by *eliminating* turbulent eddies altogether: only wave-mean flow interactions are preserved, but zonal jets are still formed. In the mechanism explored in Chapter 2, jets are formed as a result of direct (or non-local in wave-number space) transfer of energy from the forced modes (the banded structure clearly visible in Figure 1.4 (a)) to the jets. In particular, the jets are viewed as a large scale ('zonostrophic') instability of the underlying turbulent state.

1.3 Structure of forcing in the barotropic model

Previous studies on barotropic zonal jets have used a variety of choices for the forcing that drives the jets. Steady monochromatic forcing was employed by *Manfroi and Young* [1999], *Tsang and Young* [2008] and *Boland et al.* [2012] with the aim of simulating baroclinic instability. In a quasigeostrophic model with a zonal background vertical shear, the most unstable baroclinic mode is a pure zonal mode (i.e. its phase lines are aligned with the longitude) and to model this, the steady forcing is typically chosen as a sinusoidal function (like $\cos(k_f x)$, k_f representing the deformation wavenumber) to force the barotropic vorticity equation. To motivate this construction, Figure 1.5 (a) shows the initial evolution of baroclinic instability of an unstable background flow with zonally oriented vertical shear. A two-layer quasi-geostrophic model was used for the run in Figure 1.5 (a) and the plotted upper layer potential vorticity shows the characteristic 'noodle'-modes with their phase lines aligned along the meridional direction (as expected from linear instability theory). An important property of the two-layer QG model and the barotropic QG model (in the absence of forcing) is that they are both Galilean invariant [*Pedlosky*, 1982], a property that is in fact broken by the $\cos(k_f x)$ forcing. A way to preserve Galilean invariance is to chose a stochastic rapidly de-correlating forcing (see the discussion surrounding Chapter 4 (4.22) for a proof of this).

Stochastic forcing is probably the most popular driving agent, with a majority of studies [*Vallis and Maltrud*, 1993; *Smith*, 2004; *Danilov and Gurarie*, 2004; *Danilov and Gryanik*, 2004; *Galperin et al.*, 2006] using a forcing that has a isotropic spatial structure (usually a narrow band of wavenumbers at small scales) with the aim of simulating moist convection in giant planets. In Chapter 2 of this dissertation, the same isotropic narrow band forcing is employed primarily to establish a connection with the large body of research that uses this forcing. Futher the forcing is also white-noise in time as this idealization allows the construction of analytically solvable models. In Chapters 4 and 3 anisotropic forcing is used. The model forcing in Chapter 4 considers a range of possible choices for the forcing that vary from the meridional noodle-mode structure seen in Figure

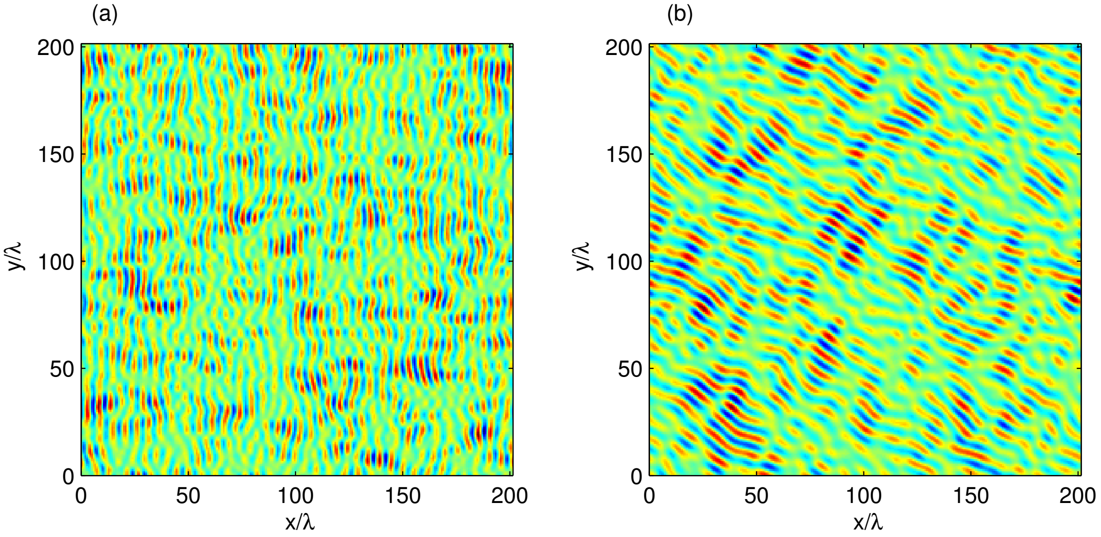

Figure 1.5: (a) Noodle modes: Snapshot of upper layer potential vorticity showing initial stages of evolution of baroclinic instability for a background with zonally oriented vertical shear (b) The same but for a flow whose vertical shear is aligned at an angle $\pi/4$ to the zonal direction. Here λ is the deformation radius.

1.5(a) to a zonal noodle-mode structure (not shown here). In Chapter 3 we also employ *tilted* noodle-like forcing, that models the baroclinically unstable modes that appear from instability of a background flow with a non-zonal mean flow, as seen in Figure 1.5(b). This titled eddy forcing causes the emergence of a new phenomenon, that has not previously been seen in forced barotropic flow on the β-plane, namely meridionally *drifting* zonal jets (as detailed in Chapter 3).

1.4 Tracer diffusion due to eddies in a background mean flow

Ocean sea surface maps obtained from satellite altimetry indicate that the extra-tropics are dominated by geostrophic eddies. These eddies are formed due to baroclinic instability of the background time-mean flow, which in case of the extratopical ocean happens almost *everywhere* since most of the ocean has been found to be baroclinically unstable[*Ferrari and Wunsch*, 2010; *Tulloch et al.*, 2011].

Eddies mix and transport momentum and heat across the ocean, while the corresponding eddy fluxes alter the background mean flow and stratification. Eddies also redistribute dissolved gases and minerals globally, and are important in both climatic and biogeochemical studies.

Global ocean models at this juncture do not possess sufficient spatial and temporal resolution to adequately resolve mesoscale eddies, and as a result, eddy fluxes continue to be a significant source of uncertainty for climate studies. In the absence of sufficient resolution, eddy fluxes are parametrized in terms of the resolved large scale flow using a diffusivity. For example in case of eddy heat fluxes, we write, $\overline{\mathbf{u}'T'} = -\kappa_e \nabla \bar{T}$ where κ_e is the eddy-duffusivity. Here the idea of 'diffusion' by eddies is invoked in analogy with the diffusion due to random motion of molecules. Continuing in this vein, the eddy diffusivity is typically written as $\kappa_e = v_e l_e$ where v_e is an estimate for the velocity scale associated with the eddies (often taken to be proportional to $\sqrt{EKE}$, where EKE is the eddy kinetic energy) and l_e is an average estimate of the eddy length scale, referred to as the 'mixing-length' [*Prandtl*, 1925]. At the ocean surface, v_e and l_e are obtained from the surface geostrophic velocity calculated from satellite altimetry [*Stammer*, 1998]. Excluding areas that have strong mean currents, like the western boundary currents and the ACC, the kinetic energy in the eddies is an order of magnitude greater than that in the time-mean flow. As a consequence, the effect of the mean flow on tracer diffusivity is not significant and can be neglected. However, in flow regions where the kinetic energy of the mean flow and the eddies are comparable, like the ACC, the mean flow can no longer be neglected in diffusivity calculations. To illustrate we start with one of the equilibrated zonal jet runs from Chapter 2 and co-evolve a passive scalar. The scalar equation and the vorticity equation are identical except the presence of the stochastic forcing (described in Chapter 2) in the vorticity equation. Figure 1.6 (c) plots the Eulerian eddy diffusivity $\overline{vc}/\beta_c$ where v is the meridional velocity, c the scalar field and β_c the background scalar field gradient. It is clear from the figure that the eddy-diffusivity is suppressed at the faster eastward jets by about a factor of 4. In the oceanographic context, *Marshall et al.* [2006] were the first to note the suppression of eddy-diffusivity by

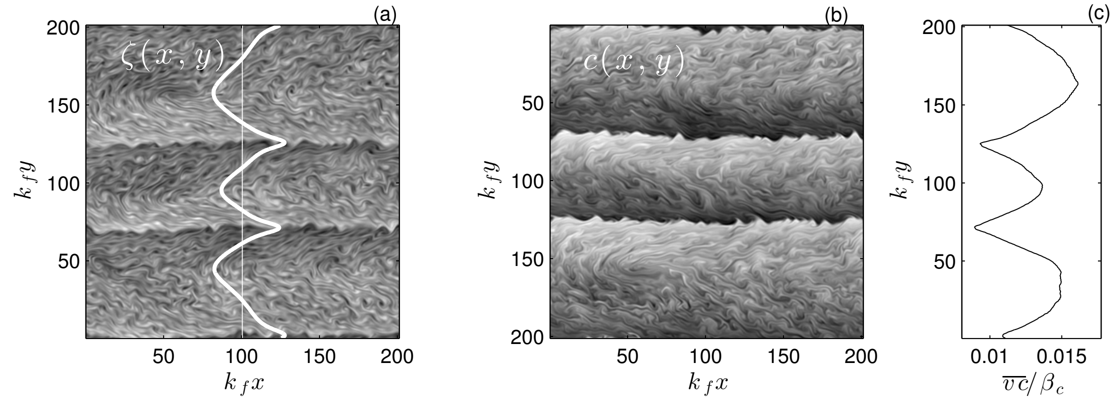

Figure 1.6: (a) Snapshot of equilibrated vorticity from a zonal jet run for $\mu_* = 0.00182$ and $\beta_* = 1$ from Chapter 2 with overlaid zonal-mean velocity (thick white line). (b) The corresponding snapshot of the passive scalar field. (c) The Eulerian eddy-diffusivity $\overline{v'c'}/\beta_c$, where β_c is the background scalar gradient.

strong mean flows in the ACC. *Ferrari and Nikurashin* [2010] provided a formal theoretical framework for identifying the effect of a mean flow, U on the Prandtl diffusivity, $\kappa_e = v_e l_e$ and provided the following modification

$$\kappa_e^U = \frac{\kappa_e}{1 + \chi(U - c)^2}\,, \tag{1.3}$$

where c is the zonal speed of the eddies, and χ is a factor which depends on the eddy structure. When there is no relative motion between the eddies and the mean flow, $U = c$ and the basic mixing length result is recovered. In other words, the greater the relative motion between the eddies and mean flow, the greater the eddy suppression.

One issue with the derivation of (1.3) by *Ferrari and Nikurashin* [2010] and *Klocker et al.* [2012] is that the meridional variation of the mean flow $U(y)$ is neglected without sufficient justification. One of the consequences of this assumption is that the mean-flow does not alter the spatial structure or scale of the eddies, i.e. there is no eddy-mean flow interaction at all. In other words, the studies of *Ferrari and Nikurashin* and *Klocker et al.* are *kinematic*. In Chapter 4, we allow the eddies to be modified by the local shear of the background mean flow through the Orr mechanism. This allows us to study the effect of shear on eddy diffusivity, which is not accounted for in (1.3) and find that strong shear can also suppress eddy diffusivity. Our mathematical approach in deriving the eddy diffusivity is based on the correlation dynamics approach used in Chapter 2.

2 Zonostrophic instability

Abstract. Zonostrophic instability leads to the spontaneous emergence of zonal jets on a β-plane from a jetless basic-state flow which is damped by bottom drag and driven by a random body force. Decomposing the barotropic vorticity equation into the zonal-mean and eddy equations, and neglecting the eddy-eddy interactions, defines the quasi-linear (QL) system. Numerical solution of the QL system shows zonal jets with length scales comparable to jets obtained by solving the nonlinear (NL) system.

Starting with the QL system, one can construct a deterministic equation for the evolution of the two-point single-time correlation function of the vorticity, from which one can obtain the Reynolds stress that drives the zonal mean flow. This deterministic system has an exact nonlinear solution, which is an isotropic and homogenous eddy field with no jets. We characterize the linear stability of this jetless solution by calculating the critical stability curve in the parameter space and successfully comparing this analytic result with numerical solutions of the QL system. But the critical drag required for the onset of NL zonostrophic instability is sometimes a factor of six smaller than that for QL zonostrophic instability.

Near the critical stability curve, the jet scale predicted by linear stability theory agrees with that obtained via QL numerics. But on reducing the drag, the emerging QL jets agree with the linear stability prediction at only short times. Subsequently jets merge with their neighbors till the flow matures into a state with jets which are significantly broader than the linear prediction, but have have similar spacing as NL jets.

2.1 Introduction

Zonal flows are banded, anisotropic, weakly fluctuating alternating jets that form spontaneously and persist indefinitely in an otherwise turbulent plasma or planetary fluid [*Diamond et al.*, 2005; *Vasavada and Showman*, 2005]. The subject started with Rhines' 1975 discovery that freely evolving barotropic β-plane turbulence transfers energy into zonal shear modes with zero frequency [*Rhines*, 1975]. Also in 1975, experiments by Whitehead showed that forcing, without the exertion of azimuthal torque, in a rapidly rotating basin produces prograde jets; in this context the curved upper surface provides an analog of the β-effect. We follow Galperin et al. (2006) in referring to the development and persistence of these anisotropic planetary flows as "zonation". *Williams* [1978] showed that zonation occurs in statistically steady forced-dissipative flows on the sphere, and proposed this as an explanation of the banded structure of the planetary circulations of Jupiter and Saturn.

Figure 2.1 shows a typical example of fully developed, forced and dissipative zonation obtained by numerical solution of (2.3) below. The main features of the statistically steady flow, such as the sharp eastward jets, the broader westward return flows, and the sawtooth relative vorticity, are familiar from many earlier studies of statistically steady, stochastically forced, dissipative β-plane turbulence in doubly periodic geometry [*Danilov and Gurarie*, 2004; *Danilov and Gryanik*, 2004; *Maltrud and Vallis*, 1991; *Smith*, 2004; *Vallis and Maltrud*, 1993], and on the sphere [*Williams*, 1978; *Nozawa and Yoden*, 1997; *Huang and Robinson*, 1998; *Scott and Polvani*, 2007].

To establish the notation used in this study, we start with the equations of motion for a forced and dissipative barotropic flow, $\boldsymbol{u} = (u, v)$:

$$\frac{D\boldsymbol{u}}{Dt} + f\hat{\boldsymbol{z}} \times \boldsymbol{u} = \hat{\boldsymbol{z}} \times \boldsymbol{\nabla} a - \boldsymbol{\nabla} p - \mu\boldsymbol{u} + \nu_n \nabla^{2n}\boldsymbol{u}\,, \tag{2.1}$$

$$\boldsymbol{\nabla}\boldsymbol{\cdot}\boldsymbol{u} = 0\,, \tag{2.2}$$

where $f = f_0 + \beta y$ is the β-plane Coriolis frequency. The flow is energized by a solenoidal (incompressible) force generated by the function $a(x, y, t)$. There is no loss of generality in taking the force to be solenoidal: any compressive component of the external force is balanced by the pressure gradient. Damping is provided by a combination of drag μ and hyper-viscosity ν_n (with $n = 4$ in numerical simulations, and $n = 1$ in development of theory).

The incompressible velocity field (2.2) admits a streamfunction, $\psi(x, y, t)$ with $(u, v) = (-\psi_y, \psi_x)$, and relative vorticity, $\zeta = \psi_{xx} + \psi_{yy}$. Eliminating the pressure from (2.1), one obtains the β-plane vorticity equation

$$\zeta_t + u\zeta_x + v\zeta_y + \beta v = \xi - \mu\zeta + \nu_n \nabla^{2n} \zeta \, . \tag{2.3}$$

The vorticity forcing ξ on the right of (2.11) is the curl of the solenoidal force in the momentum equation i.e.,

$$\xi = \nabla^2 a \, . \tag{2.4}$$

We assume that the forcing, a in (2.1) and ξ in (2.3), is a rapidly de-correlating, isotropic, spatially homogeneous, random processes. Thus energy and enstrophy are injected into a narrow band of wavenumbers centered on a "forced wavenumber" k_f (see Appendix A for details of the implementation). This model of exogenous stochastic forcing, first proposed by *Lilly* [1969], is now a standard protocol used in many barotropic and shallow-water studies of forced-dissipative zonation. The physical interpretation of the forcing, and the choice of its spatial structure, vary somewhat in literature. Considering ξ to be a representation of baroclinic eddies, *Williams* [1978] chose the forced wavenumbers to lie in a narrow rectangular band, with the zonal extent of the band equal to the baroclinic deformation radius. *Scott and Polvani* [2007] and *Smith* [2004] interpreted the rapidly de-correlating, narrow-band, isotropic forcing as a model of small-scale three-dimensional convection. Another possibility is that ξ is a representation of the bubble-cloud forcing used by *Whitehead* [1975] in the laboratory. Below, in the discussion surrounding (2.10) we give yet another interpretation of the forcing ξ.

We have found no studies that establish any particular forcing protocol as being a reasonable physical representation of three-dimensional small-scale eddies acting on a barotropic flow. However, despite the two strong modeling approximations, namely quasi-geostrophy and the choice of the forcing, some features

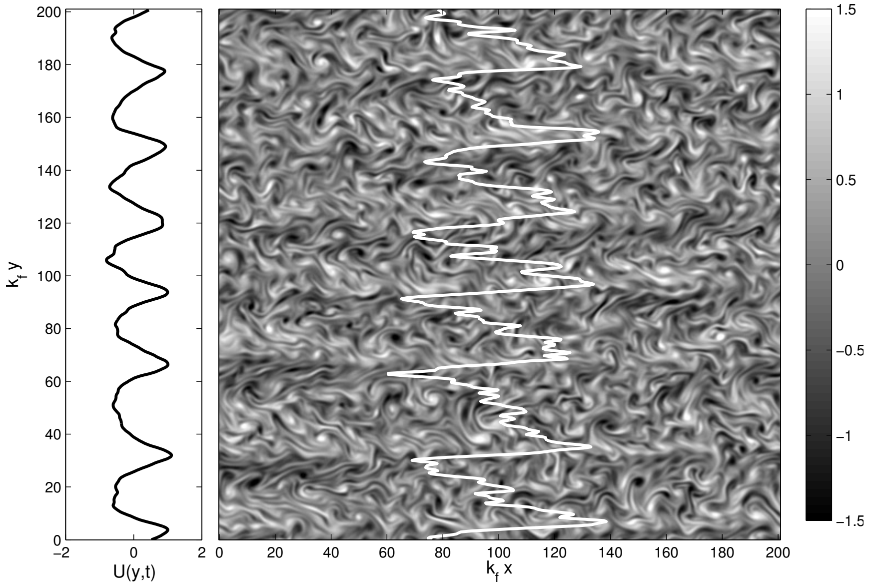

Figure 2.1: *Nonlinear (NL) zonal jets.* Left panel: a snapshot of the zonally averaged velocity $U(y,t)$ obtained from a solution of (2.3) in a doubly periodic domain $2\pi L \times 2\pi L$ with $k_f L = 32$, where k_f is the dominant wavenumber of the forcing ξ. Right panel: a snapshot of the vorticity ζ, with overlaid zonally averaged vorticity $-U_y(y,t)$ (solid white curve). The parameter values for this run are $\mu_* = 0.01824$ and $\beta_* = 1.0$. The snapshot is at $2\mu t = 25$ with spin-up from rest.

of Jovian jets, like the jet width, are approximately captured by simplified models [*Smith*, 2004; *Vasavada and Showman*, 2005]. A different model forcing due to *Showman* [2007] uses non-solenoidal physical-space mass-forcing to represent moist convection in a shallow water system. Despite the different choice of forcing, Showman's results on planetary zonal jets are broadly consistent with those obtained by *Smith* [2004]. In light of this fact, and since the barotropic QG system cannot represent mass-forcing, we do not address these issues further.

A common theme in all the studies mentioned above is a separation of scales between the forcing length scale, k_f^{-1}, and the width of the emergent jets. Indeed the spacing of the jets in Figure 2.1 is significantly greater than k_f^{-1}, which is an indication of either the inverse cascade, or of a spectrally nonlocal transfer of

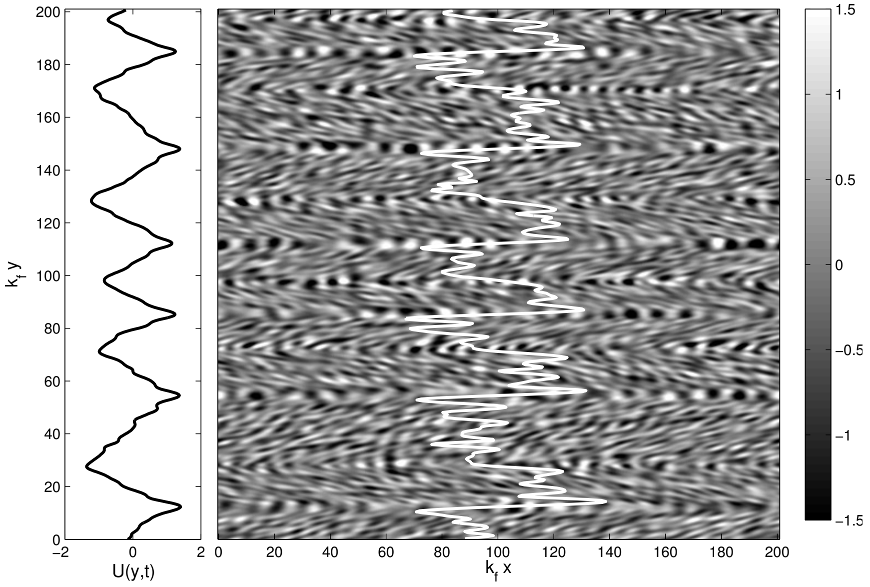

Figure 2.2: *Quasilinear (QL) zonal jets.* Left panel: a snapshot of the zonally averaged velocity $U(y,t)$ obtained by integrating the QL system (2.6), (2.7) and (2.9). Right panel: a snapshot of the QL vorticity ζ, with overlaid zonally averaged vorticity $-U_y$ (solid white curve). The parameters for this run are the same as the nonlinear solution in Figure 2.1 i.e., $\mu_* = 0.0182$, $\beta_* = 1$ and $k_f L = 32$. The snapshot is at $2\mu t = 40$ after spin-up from rest.

energy [*Huang and Robinson*, 1998].

A striking feature of β-plane zonation is that the translational symmetry, $y \to y + a$, of the equation of motion (2.3) is spontaneously broken: the locations of the eastward maxima in Figure 2.1 are an accident of the initial conditions and of the random number generator used to create ξ. If the bottom friction is weak enough, jets that form remain in the same position, apparently forever. In the limit $\beta \to 0$ however, the jets get weaker (with no jets for $\beta = 0$) and have a tendency to meander along the meridional direction, without a net migration. We do not discuss the phenomenon of meandering jets any further in this chapter. In the weak friction limit, once quasi-steady jets are in place, their dynamics can be discussed in mechanistic terms using concepts such as potential vorticity mixing, the resilience of transport barriers at the velocity maxima, radiation stress and shear-straining of turbulent eddies [*Rhines and Young*, 1982; *Dritschel and McIntyre*, 2010]. But the primary question addressed here is why the jets form in the first place, given that the forcing ξ does not select particular locations. Following earlier investigations of this phenomenon [*Farrell and Ioannou*, 2007; *Manfroi and Young*, 1999], we show that zonation can be understood as symmetry-breaking instability of an isotropic, spatially homogeneous and jetless β-plane flow .

In section 2.2 we introduce the eddy-mean decomposition and discuss a statistical method, previously used by *Farrell and Ioannou* [1993a, 2003, 2007], *Marston et al.* [2008], and *Tobias et al.* [2011], which is the basis of our linear stability analysis of zonostrophic instability. This method amounts to forming quadratic averages of the equations of motion and then discarding third-order cumulants. *Farrell and Ioannou* [2003, 2007] refer to this method as stochastic structural stability theory (SSST), while *Marston et al.* [2008] call it the second-order cumulant expansion, or CE2. SSST and CE2 are completely equivalent, and only one name is required. We have therefore adopted the more descriptive CE2 terminology of *Marston et al.* [2008].

In section 2.3 we present a physical space re-formulation of CE2 which has analytic advantages over earlier numerically oriented formulations. Within the context of CE2, section 2.4 provides a complete analytic description of zonostrophic instability obtained by linearizing around an exact isotropic and homogeneous solution with no jets. As in *Farrell and Ioannou* [2007], zonation is understood as a linear instability of CE2: part of the linearly unstable eigenmode is a zonal flow. This linear stability problem is characterized by two control parameters, a non-dimensional drag parameter μ_* and a non-dimensional planetary parameter β_*, and we determine the CE2 zonostrophic stability boundary in the (β_*, μ_*)-parameter plane. An important property of CE2 zonostrophic instability is that the most unstable wavenumber, which determines the meridional scale of the exponentially growing jets, is well away from zero. Because the instability unfolds around a nonzero wavenumber, CE2 zonostrophic instability is not properly a negative-viscosity instability. This point is reinforced in section 2.5 by showing that the CE2 eddy viscosity is identically zero. Section 2.6 is a comparison between the analytic results and direct numerical simulations of the nonlinear system. Section

2.7 is the discussion and conclusion. The more technical aspects of the paper are in five appendices.

2.2 The eddy-mean decomposition and quasilinear (QL) dynamics

We use an eddy-mean decomposition

$$\psi(x,y,t) = \bar{\psi}(y,t) + \psi'(x,y,t)\,, \tag{2.5}$$

where the overbar denotes a zonal average; we also denote the zonal mean velocity as $U(y,t) = \bar{u}(y,t)$. Applying this average to (2.3) results in the zonal mean momentum equation

$$\partial_t U + \partial_y \left(\overline{u'v'}\right) = -\mu U + \nu \partial_y^{2n} U\,, \tag{2.6}$$

and the eddy vorticity equation

$$\zeta'_t + U\zeta'_x + (\beta - U_{yy})\psi'_x + \mathrm{EENL} = \xi - \mu\zeta' + \nu\nabla^{2n}\zeta'\,. \tag{2.7}$$

In (2.7), the eddy-eddy nonlinearity is

$$\mathrm{EENL} \overset{\mathrm{def}}{=} \psi'_x\zeta'_y - \psi'_y\zeta'_x - \left(\overline{\psi'_x\zeta'}\right)_y\,. \tag{2.8}$$

In addition to the zonal average, the overbar includes a running time average over a short interval so that $\bar{\xi}(y,t)$ does not appear on the right of (2.6). In presenting equations subsequently used to obtain analytic results, we use $n = 1$ for the viscosity.

2.2.1 Quasilinear (QL) dynamics

The main results in this paper are obtained with a quasilinear (QL) system, which is defined by taking

$$\mathrm{EENL} \to 0 \tag{2.9}$$

in (2.7). Figure 2.2 shows a QL solution at the same parameter values as the fully nonlinear (NL) solution as Figure 2.1. Because of the coupling between the

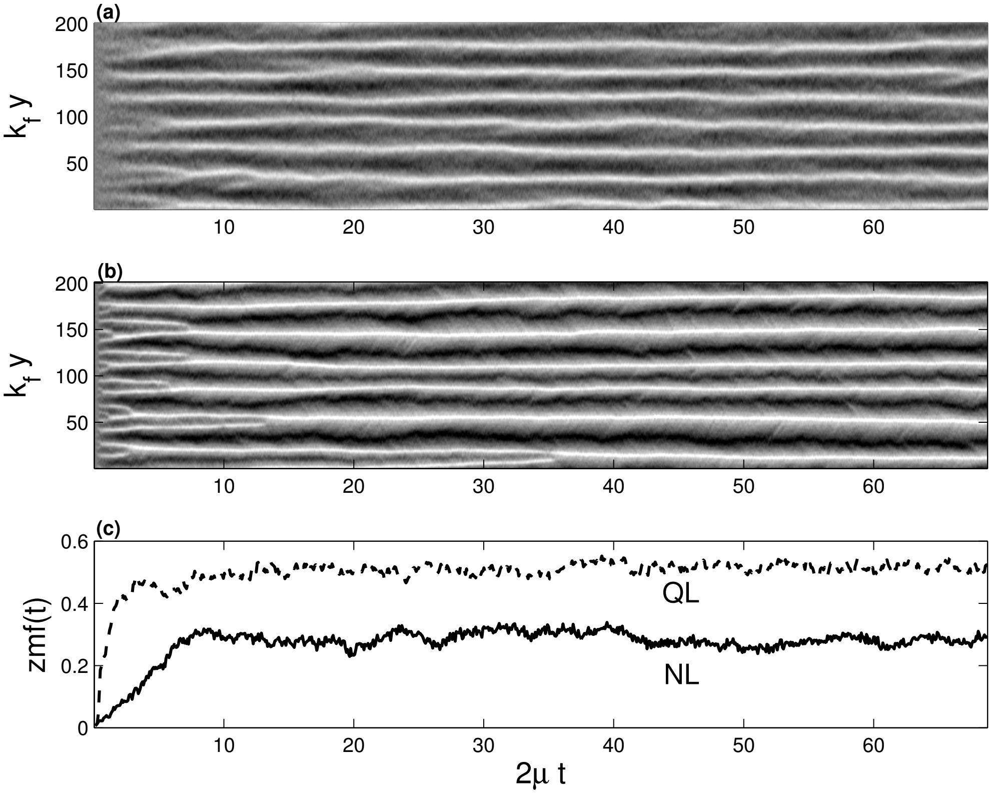

Figure 2.3: (a) Hovmöller diagram of the zonal mean velocity $U(y,t)$ obtained by solution of the full nonlinear (NL) system in (2.3). (b) Hovmöller diagram of the zonal mean velocity $U(y,t)$ obtained by solution of the quasilinear (QL) system. (c) A comparison of the zonal mean energy fraction, zmf(t) defined in (3.16), for QL and NL runs. The time-averaged fractions are $\langle \text{zmf} \rangle_{\text{NL}} = 0.3$ and $\langle \text{zmf} \rangle_{\text{QL}} = 0.51$. This figure shows the time evolution of the runs in Figures 2.1 and 2.2.

mean and the eddies, the QL system is nonlinear, and Figure 2.2 shows that QL dynamics still results in the spontaneous formation of quasisteady zonal jets.

Comparing the left panels in Figures 2.1 and 2.2, one sees that the QL jets are faster and wider than NL jets, and the jet profiles are different: QL jets are distinctly more east-west symmetric than NL jets. Nonetheless, we show in section 2.6 that the QL jets in Figure 2.2 do have a small east-west QL asymmetry, and at other points in the (β_*, μ_*)-parameter space, QL jets are strongly east-west asymmetric.

Because the QL jets are faster, the QL system is more zonostrophically unstable than the NL system. In Figures 2.1 and 2.2, quasi-steady jets evolve spontaneously from an initially jetless state, as shown in the Hovmöller diagram of the zonal mean flow $U(y,t)$ in Figure 2.3. Comparing the upper and middle panels in Figure 2.3, shows that the QL system has significantly longer adjustment times than the NL system.

O'Gorman and Schneider [2007] made the QL approximation (2.9) in an atmospheric general circulation model and showed by comparison with the full nonlinear version of the model that several important features of the flow are unaffected by complete removal of the eddy-eddy nonlinearity as in (2.9). Comparing Figures 2.1 and 2.2 we reach a similar conclusion for the more idealized model studied here. This preliminary conclusion is supported by a detailed comparison between NL and QL solutions in section 2.6.

There are several ways of motivating QL dynamics. The QL system conserves both energy and enstrophy, and has the same zonal-mean equation and symmetries as the NL system. Thus arguments based on quadratic integral invariants apply equally to the QL and the NL system [*Salmon*, 1998]. Nonetheless, because EENL is discarded, the QL system cannot exhibit a true Batchelor-Kraichnan inverse energy cascade: in the QL model all nonlinear interactions require participation of the zonal mean flow. Because $U(y,t)$ has a larger length scale than the eddy field, all these nonlinear QL interactions are spectrally nonlocal. Figure 2.2 shows that the spectrally local Batchelor-Kraichnan inverse cascade is not necessary for zonation.

Potential vorticity (PV) is not materially conserved by the QL system, and consequently non-quadratic functions of PV are not conserved by the nonlinear terms remaining in QL. Thus Figure 2.2 also shows that strict material conservation of PV is not necessary for zonation.

Thus, at the most basic level, the QL system is instructive as an indication of the physically essential processes necessary for zonation.

2.2.2 Stochastic closure versus cumulant expansion

A main motivation of the QL system is that using the statistical method pioneered in meteorology by *Farrell and Ioannou* [1993a, 2003, 2007] one can compute important average quadratic properties of the QL flow, such as Reynolds stress and the eddy enstrophy and energy. However rather than (2.9), *Farrell and Ioannou* [2007] adopt a stochastic closure, which amounts to replacing the eddy-eddy nonlinearity with a combination of random forcing and dissipation:

$$\mathrm{EENL} \to -\xi_{\mathrm{EENL}} + \mu_{\mathrm{EENL}}\zeta' \,; \tag{2.10}$$

see also *DelSole* [2001]. The intent of (2.10) is that the random forcing $\xi_{\mathrm{EENL}}(\boldsymbol{x}, t)$ and the dissipation $\mu_{\mathrm{EENL}}\zeta'$ should be chosen to match the evolution of the NL system. The terms in (2.10) then augment the exogeneous forcing and dissipation on the right of (2.7).

However there is probably no reliable a priori method of determining the right hand side of (2.10). Heeding the principle to first do no harm, we prefer the QL alternative (2.9). This has the advantage that one can then make a specific comparison between QL and NL solutions (e.g., as in Figures 2.1 and 2.2) and assess the role of EENL.

Our point of view, which follows *Marston et al.* [2008] and *Tobias et al.* [2011], is to regard the QL system as an approximation to the NL system. In fact, (2.9) in tandem with the method of Farrell & Ioannou, is precisely the second-order cumulant expansion CE2 of *Marston et al.* [2008]. It is from this perspective that in section 2.3 we develop a physical-space formulation of CE2, which is suitable for analytic solution.

2.3 Dynamics of correlations: CE2

In the QL approximation, the eddy vorticity equation can be written as

$$\partial_t\zeta' + \mathsf{L}\,\partial_x\psi' = \xi - \mu\zeta' + \nu\nabla^2\zeta' \,, \tag{2.11}$$

where L is the Rayleigh-Kuo operator

$$\mathsf{L} \stackrel{\text{def}}{=} U\,\nabla^2 + (\beta - U_{yy}) \;. \tag{2.12}$$

In this section we obtain a closed deterministic evolution equation for the two-point correlations function of vorticity ζ' and streamfunction ψ'. This correlation equation, (2.23) below, is coupled to the evolution of the zonal mean flow via the Reynolds stresses, and the Reynolds stresses can be obtained by evaluating derivatives of the correlation function at zero separation. Thus one obtains the zonal-mean evolution equation in (2.34) below.

2.3.1 Correlation functions: kinematics

We assume that the external forcing, $a(\boldsymbol{x},t)$ in (2.1) and $\xi(\boldsymbol{x},t)$ in (2.11), has a two-point, two-time correlation functions of the form

$$\overline{a(\boldsymbol{x}_1,t_1)a(\boldsymbol{x}_2,t_2)} = \delta(t_2-t_1)\,A(x_1-x_2,y_1,y_2)\,, \tag{2.13}$$

$$\overline{\xi(\boldsymbol{x}_1,t_1)\xi(\boldsymbol{x}_2,t_2)} = \delta(t_2-t_1)\,\Xi(x_1-x_2,y_1,y_2)\,, \tag{2.14}$$

where the overbar above denotes an ensemble average. The dependence of the spatial correlation functions A and Ξ only on the difference

$$x \stackrel{\text{def}}{=} x_1 - x_2 \tag{2.15}$$

indicates that the forcing is zonally homogeneous. We do not assume (yet) that the forcing is isotropic and meridionally homogenous.

Because derivatives commute with the ensemble average, the relation (2.4) implies that A and Ξ are related by

$$\Xi = \nabla_1^2\nabla_2^2 A\,, \tag{2.16}$$

where the Laplacian acting on the coordinates of point n is

$$\nabla_n^2 \overset{\text{def}}{=} \partial_x^2 + \partial_{y_n}^2 \,. \tag{2.17}$$

Notice that that we have changed notation: undecorated x in (2.15) is the zonal difference coordinate. We also use the shorthand $u_1' = u'(\boldsymbol{x}_1, t)$, $U_2 = U(y_2, t)$, $\zeta_2' = \zeta'(\boldsymbol{x}_2, t)$ etc. Strictly speaking, we should decorate all the variables in (2.11) with the subscript $n = 1$ or 2 to explicitly indicate whether we refer to the eddy-vorticity equation at the point $\boldsymbol{x}_1 = (x_1, y_1)$, or at the point $\boldsymbol{x}_2 = (x_2, y_2)$. We forbear.

We assume "ergodicity", so that the overbar is also equivalent to the zonal average of a single realization. We desire the single-time two-point correlation functions

$$\mathcal{Z}(x, y_1, y_2, t) \overset{\text{def}}{=} \overline{\zeta_1'\zeta_2'} \,, \tag{2.18}$$

and

$$\Psi(x, y_1, y_2, t) \overset{\text{def}}{=} \overline{\psi_1'\psi_2'} \,. \tag{2.19}$$

The analog of (2.16) is

$$\mathcal{Z} = \nabla_1^2 \nabla_2^2 \Psi \,. \tag{2.20}$$

Given the streamfunction correlation $\Psi(x, y_1, y_2, t)$, one can obtain the velocity correlation tensor as

$$V_{ij}(x, y_1, y_2, t) \overset{\text{def}}{=} \begin{pmatrix} \overline{u_1'u_2'} & \overline{u_1'v_2'} \\ \overline{u_2'v_1'} & \overline{v_1'v_2'} \end{pmatrix} = \begin{pmatrix} \partial_{y_1}\partial_{y_2} & \partial_x\partial_{y_1} \\ -\partial_x\partial_{y_2} & -\partial_x^2 \end{pmatrix} \Psi \,. \tag{2.21}$$

Because the choice of denoting one point as $\boldsymbol{x}_1$ and the other as $\boldsymbol{x}_2$ is arbitrary, all correlation function have an important "exchange" symmetry

$$\Psi(x, y_1, y_2) = \Psi(-x, y_2, y_1) \,, \tag{2.22}$$

and likewise for A, $\mathcal{Z}$, Ξ etc.

2.3.2 Correlation functions: dynamics

It follows from (2.11) and (2.14) that the correlation functions evolve as

$$\partial_t \mathcal{Z} + \left(\nabla_2^2 \mathsf{L}_1 - \nabla_1^2 \mathsf{L}_2\right) \partial_x \Psi = \Xi - 2\mu \mathcal{Z} + \nu \left(\nabla_1^2 + \nabla_2^2\right) \mathcal{Z} \,, \tag{2.23}$$

where the Rayleigh-Kuo operator at point n is $\mathsf{L}_n \equiv U_n \nabla_n^2 + (\beta - U_n'')$.

To derive (2.23), multiply the equation for $\partial_t \zeta_1'$ by ζ_2' and add this to the $\partial_t \zeta_2'$-equation multiplied by ζ_2'. The sum is then ensemble averaged, and after the average all fields depend on x_1 and x_2 only through the combination $x = x_1 - x_2$. Because of this zonal homogeneity $\partial_{x_1} = -\partial_{x_2} = \partial_x$. Thus, for example,

$$\overline{\zeta_2' \mathsf{L}_1 \partial_{x_1} \psi_1'} + \overline{\zeta_1' \mathsf{L}_2 \partial_{x_2} \psi_2'} = \left(\nabla_2^2 \mathsf{L}_1 - \nabla_1^2 \mathsf{L}_2\right) \partial_x \, \overline{\psi_1' \psi_2'} \,. \tag{2.24}$$

A crucial simplification is that the forcing is rapidly decorrelating in time, as expressed by the $\delta(t_1 - t_2)$ in (2.14). Considerations summarized in Appendix B (amounting to a simple proof of Ito's formula) show that

$$\overline{\zeta_1' \xi_2} + \overline{\zeta_2' \xi_1} = \Xi \,. \tag{2.25}$$

The result above is the origin of the first term on the right hand side of (2.23).

2.3.3 Collective coordinates

As alternatives to y_1 and y_2, there are advantages in using the "collective coordinates"

$$y \overset{\text{def}}{=} y_1 - y_2 \qquad \text{and} \qquad \bar{y} \overset{\text{def}}{=} \tfrac{1}{2}(y_1 + y_2) \,. \tag{2.26}$$

Eventually we will restrict attention to homogenous and isotropic forcing, and at that point we take Ξ in (2.14) to be a function only of the two-point separation

$$r \overset{\text{def}}{=} |\boldsymbol{x}_1 - \boldsymbol{x}_2| = \sqrt{x^2 + y^2} \,. \tag{2.27}$$

Collective coordinates are then essential for analytic progress.

In terms of y and $\bar{y}$, the Laplacians are

$$\nabla_n^2 = \nabla^2 - (-1)^n \partial_y \partial_{\bar{y}} + \tfrac{1}{4} \partial_{\bar{y}}^2 \,, \tag{2.28}$$

where $\nabla^2 \overset{\text{def}}{=} \partial_x^2 + \partial_y^2$ is the "separation" Laplacian. Thus, for instance,

$$\mathscr{Z} = \left(\nabla^2 + \partial_y \partial_{\bar{y}} + \tfrac{1}{4}\partial_{\bar{y}}^2\right)\left(\nabla^2 - \partial_y \partial_{\bar{y}} + \tfrac{1}{4}\partial_{\bar{y}}^2\right) \Psi \,, \tag{2.29}$$

$$= \nabla^4 \Psi + \tfrac{1}{2}\left(\partial_x^2 - \partial_y^2\right) \partial_{\bar{y}}^2 \Psi + \tfrac{1}{16} \partial_{\bar{y}}^4 \Psi \,. \tag{2.30}$$

Using the coordinates in (2.26), the correlation equation (2.23) becomes

$$\begin{aligned}\partial_t \mathcal{Z} + (U_1 - U_2)\partial_x \mathcal{Z} - (U_1'' - U_2'')\left(\nabla^2 + \tfrac{1}{4}\partial_{\bar{y}}^2\right)\partial_x \Psi \\ - \left(2\beta - U_1'' - U_2''\right)\partial_{\bar{y}}\partial_y\partial_x \Psi \\ = \Xi - 2\mu\mathcal{Z} + 2\nu\nabla^2\mathcal{Z} + \tfrac{1}{2}\nu\partial_{\bar{y}}^2\mathcal{Z}\,, \end{aligned} \tag{2.31}$$

where now $U_1 = U\left(\bar{y} + \frac{1}{2}y\right)$ and $U_2 = U\left(\bar{y} - \frac{1}{2}y\right)$

2.3.4 The zonal mean flow equation

One advantage of collective coordinates is that mean square quantities, such as the enstrophy, are obtained by evaluating correlation functions at zero separation i.e., by setting $(x, y) = 0$. For example if one possesses $\mathcal{Z} = \mathcal{Z}(x, y, \bar{y}, t)$ then the eddy enstrophy is $\overline{\zeta'^2} = \mathcal{Z}(0, 0, \bar{y}, t)$.

A key result, obtained by evaluating

$$\overline{u_1'v_2'} + \overline{u_2'v_1'} = 2\partial_x\partial_y\Psi \tag{2.32}$$

at $(x, y) = 0$, is that the Reynolds stress is

$$\overline{u'v'}(\bar{y}, t) = \partial_y\partial_x\Psi(0, 0, \bar{y}, t)\,. \tag{2.33}$$

Thus the mean flow equation (2.6) can be written as

$$\partial_t U + \partial_{\bar{y}}\partial_y\partial_x\Psi(0, 0, \bar{y}, t) = -\mu U + \nu\partial_{\bar{y}}^2 U\,. \tag{2.34}$$

The mean flow equation (2.34), coupled with the correlation equation (2.31), is a closed system for the ensemble-averaged properties of QL dynamics.

2.4 Zonostrophic instability of a spatially homogeneous and isotropic base-state flow

2.4.1 The spatially homogeneous basic state

We now suppose that the forcing is statistically homogenous and isotropic, *i.e.* that the correlation function of the forcing has the particular form

$$\overline{\xi(\boldsymbol{x}_1, t_1)\xi(\boldsymbol{x}_2, t_2)} = \delta(t_2 - t_1)\,\Xi(r)\,, \tag{2.35}$$

where r is the two-point separation defined in (2.27). Because Ξ does not depend on $\bar{y}$, there is a simple exact solution to (2.31) and (2.34). This solution is spatially homogeneous and isotropic and has no mean flow, $U = 0$. With these simplifications the correlation equation (2.31) collapses to:

$$\left(2\mu - 2\nu\nabla^2\right)\mathcal{Z}_{\mathsf{H}} = \Xi\,. \tag{2.36}$$

The subscript H emphasizes that $\mathcal{Z}_{\mathsf{H}}(r)$ is spatially homogeneous i.e., independent of $\bar{y}$. The streamfunction correlation function, $\Psi_{\mathsf{H}}(x, y)$, can be obtained from $\mathcal{Z}_{\mathsf{H}}$ by solving $\nabla^4\Psi_{\mathsf{H}} = \mathcal{Z}_{\mathsf{H}}$. It is remarkable that $\mathcal{Z}_{\mathsf{H}}$ in (2.36) is independent of β: an isotropic and spatially homogenous forcing drives an isotropic and spatially homogeneous flow, despite the anisotropy of Rossby wave propagation.

We now apply the Fourier integral theorem,

$$\tilde{f}(p, q) \overset{\text{def}}{=} \iint f(x, y)\mathrm{e}^{-i(px+qy)}\,\mathrm{d}x\,\mathrm{d}y\,, \tag{2.37}$$

$$f(x, y) = \iint \tilde{f}(p, q)\mathrm{e}^{i(px+qy)}\,\frac{\mathrm{d}p\,\mathrm{d}q}{(2\pi)^2}\,, \tag{2.38}$$

to (2.36). We use the notation

$$h \overset{\text{def}}{=} \sqrt{p^2 + q^2}\,, \tag{2.39}$$

so that after the Fourier transform $h^4\tilde{\Psi}_{\mathsf{H}} = \tilde{\mathcal{Z}}_{\mathsf{H}}$, and the streamfunction spectrum is related to the forcing spectrum by

$$\tilde{\Psi}_{\mathsf{H}}(h) = \frac{\tilde{\Xi}(h)}{2\mu h^4 + 2\nu h^6}\,. \tag{2.40}$$

We emphasize that $\tilde{\Psi}_{\mathsf{H}}(h)$ in (2.40) is not singular as $h \to 0$. To see this, we recall (2.16), which in this homogeneous and isotropic case implies that $\Xi = \nabla^4 A$, and therefore $\tilde{\Xi} = h^4\tilde{A}$. In terms of $\tilde{A}$ then, the streamfunction spectrum in (2.40) becomes

$$\tilde{\Psi}_{\mathsf{H}}(h) = \frac{\tilde{A}(h)}{2\mu + 2\nu h^2}\,. \tag{2.41}$$

Since $a(\boldsymbol{x}, t)$ is stationary, the spectra $\tilde{A}(h)$ and $\tilde{\Psi}_{\mathsf{H}}(h)$ are finite as $h \to 0$ (provided that $\mu \neq 0$).

Later we will need two integral constraints on the vorticity forcing correlation function Ξ:

$$\iint \Xi(x,y)\,\mathrm{d}x\mathrm{d}y = \tilde{\tilde{\Xi}}(0,0) = 0\,, \tag{2.42}$$

and also

$$\iint \Xi(x,y) r^2\,\mathrm{d}x\mathrm{d}y = \lim_{h\to 0} h^{-2}\tilde{\tilde{\Xi}}(p,q) = 0\,. \tag{2.43}$$

These follow from $\Xi = \nabla^4 A$, and the assumption that the correlation function $A(r)$ decays faster than r^{-1} as $r \to \infty$. The constraints above are satisfied by the standard forcing protocol described in Appendix A, which has zero spectral density around $h = 0$.

2.4.2 The dispersion relation of inviscid and isotropic flow

The linear stability of the spatially homogeneous solution in (2.41) is determined by imposing small initial disturbances and examining evolution in time. The perturbation variables are added to the base state variables, $(0, \Psi_\mathsf{H}, \mathcal{Z}_\mathsf{H})$ and substituted into equations (2.31) and (2.34). The total 'flow', with mean and imposed small perturbations, is

$$\begin{bmatrix} U(\bar{y},t) \\ \mathcal{Z}(x,y,\bar{y},t) \\ \Psi(x,y,\bar{y},t) \end{bmatrix} = \begin{bmatrix} 0 \\ \mathcal{Z}_\mathsf{H}(x,y) \\ \Psi_\mathsf{H}(x,y) \end{bmatrix} + \mathrm{e}^{im\bar{y}+st} \begin{bmatrix} \hat{U}(m,s) \\ \hat{\mathcal{Z}}(x,y;m,s) \\ \hat{\Psi}(x,y;m,s) \end{bmatrix} + \text{c.c.}\,, \tag{2.44}$$

where m is the meridional wavenumber of the disturbances and s is the growth rate, with growing perturbations corresponding to $\Re(s) > 0$. Retaining terms linear in the perturbation variables $(\hat{U}, \hat{\Psi}, \hat{\mathcal{Z}})$, one has the equations governing the evolution of small perturbations to the homogeneous solution. The details of the subsequent solution are in Appendix C, and a main result of that analysis is the dispersion relation

$$\begin{aligned} 2\mu\beta^2 \frac{s+\mu}{s+2\mu} &= \\ &\int_0^\infty h^5 \left(h^2 - m^2\right) \tilde{A}(h)\, Q\left[\frac{h^2(s+2\mu)}{m\beta}, \frac{m}{h}\right] \frac{\mathrm{d}h}{2\pi}\,, \end{aligned} \tag{2.45}$$

where $\tilde{A}(h)$ is the forcing spectrum in (2.41), and the function $Q(\chi, n)$ is defined by the angular integral

$$Q(\chi, n) \overset{\text{def}}{=} \oint \frac{\cos^2\theta\,\left(1 + n^2 - 4\sin^2\theta\right)}{\left(\chi + \mathrm{i}\sin 2\theta\right)^2 + n^2\left[\chi^2(n^2 + 2 - 4\sin^2\theta) + \cos^2\theta\right]}\,\frac{\mathrm{d}\theta}{2\pi}\,. \tag{2.46}$$

The dispersion relation (2.45) applies to the special case of isotropic forcing, $A = A(r)$ and $\nu = 0$; a more general expression of the dispersion relation is in Appendix C.

Dr. George Carnevale has shown that the dispersion relation in (2.45) and (2.46) is also obtained from equation (5.13) in *Carnevale and Martin* [1982]. The field-theoretic approach of *Carnevale and Martin* [1982] is different from the approximation used to obtain the CE2 system in (2.31) and (2.34) e.g., CE2 contains terms such as $(U_1 - U_2)\mathcal{Z}_x$, which *Carnevale and Martin* [1982] consider to be fourth order in wave amplitude, and therefore negligible. However, after linearization of CE2 around a basic state with $U = 0$, these terms are neglected. Therefore the linearized version of CE2 in this section is equivalent to the weak-turbulence limit (5.13) in *Carnevale and Martin* [1982]. This consistency provides confidence in (2.45) and (2.46).

2.4.3 Ring forcing

In most previous investigations of zonation, the forcing is limited to an annulus of wave numbers in Fourier-space. Typically the annulus of forced modes has a mean radius $h = k_f$ and has thickness $2\delta k \ll k_f$. This is the "narrow-band forcing" described in Appendix A. We idealize this choice further by considering 'ring' forcing corresponding to the limit $\delta k \to 0$. In other words, we consider a random flow, driven isotropically by injecting energy on the circle $h = k_f$ in wavenumber space. This corresponds to

$$A(r) = \frac{2\varepsilon}{k_f^2} J_0(k_f r)\,, \qquad \tilde{A}(h) = \frac{4\pi\varepsilon}{k_f^3}\delta(h - k_f)\,, \tag{2.47}$$

where J_0 is the Bessel function of order zero. Notice that $\Xi = \nabla^4 A = k_f^4 A$. With $\nu = 0$ — as we assume in (2.45) — the spatially homogeneous base state solution in (2.41) is

$$\Psi_{\mathsf{H}}(r) = \varepsilon\,\frac{J_0(k_f r)}{k_f^2\mu}\,, \qquad \tilde{\Psi}_{\mathsf{H}}(h) = 2\pi\varepsilon\,\frac{\delta(h-k_f)}{k_f^3\mu}\,. \tag{2.48}$$

The parameter ε above, with dimensions Watts per kilogram, is the rate of working of the force that sustains the base state (2.48) flow against dissipation.

With $\delta(h-k_f)$ in (2.47), the h-integral in (2.45) is trivial. Before proceeding however, it is convenient to write the various parameters in the non-dimensional form using the length scale k_f^{-1} and time scale $(\varepsilon k_f^2)^{-1/3}$. These scales lead to the control parameters

$$\mu_* \stackrel{\text{def}}{=} \frac{\mu}{k_f^{2/3}\varepsilon^{1/3}}\,, \qquad \beta_* \stackrel{\text{def}}{=} \frac{\beta}{k_f^{5/3}\varepsilon^{1/3}}\,. \tag{2.49}$$

The nondimensional wavenumber and growth rate are

$$m_* \stackrel{\text{def}}{=} \frac{m}{k_f}\,, \quad \text{and} \quad s_* \stackrel{\text{def}}{=} \frac{s}{(\varepsilon k_f^2)^{1/3}}\,. \tag{2.50}$$

The zonostrophic dispersion relation in non-dimensional variables is then

$$\mu_*\beta_*^2\,\frac{s_*+\mu_*}{s_*+2\mu_*} = (1-m_*^2)\,Q\left(\frac{s_*+2\mu_*}{m_*\beta_*}, m_*\right)\,, \tag{2.51}$$

with the function Q defined in (2.46). We now lighten the notation by dropping the $*$ on non-dimensional variables m and s. We have obtained the growth rate by solving (2.51) numerically for $s = s_r + is_i$. This numerical solution indicates that modes with $s_r > 0$ are found only if $0 < m^2 < 1$, and these unstable modes have $s_i = 0$. We have been unable to obtain a satisfactory non-numerical proof of these two important properties of zonostrophic instability.

Figure 2.4 shows some examples of the growth rate $s(m)$ plotted as a function of m for various values of β_*, with $\mu_* = 0.15$ in all cases. If $s > 0$ for some values of m (e.g., $\beta_* = 0.15$ and 1 in Figure 2.4) then the homogeneous flow is unstable and zonal jets will grow from very small initial amplitude. Also shown in Figure 2.4 are two marginally stable situations $\beta_* = 0.0634$ and $\beta_* = 2.571$. These are defined by the condition that the most unstable disturbance has $s = 0$:

$$\max_{\forall m} s(m;\beta_*,\mu_*) = 0\,. \tag{2.52}$$

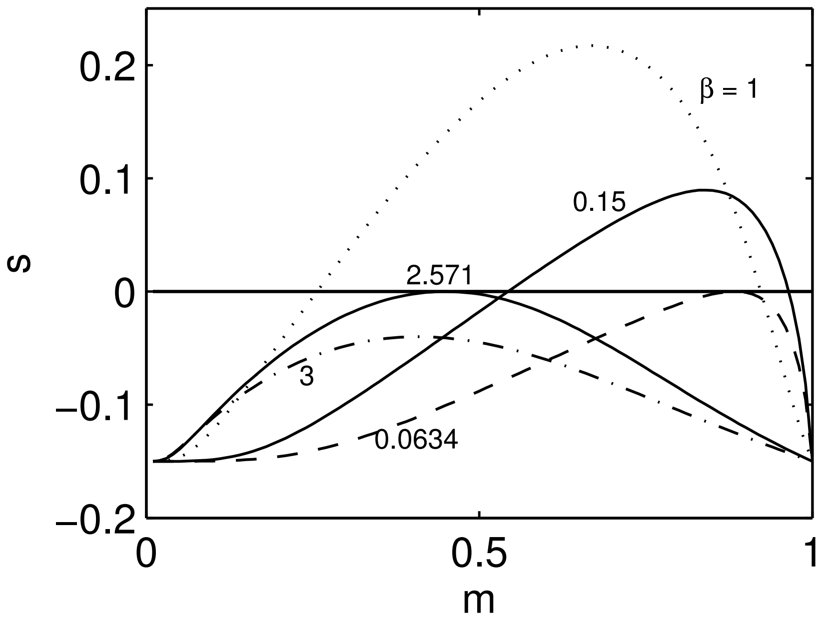

Figure 2.4: The growth rate s as a function of m for $\mu_* = 0.15$ and five values of β_* indicated on the curves. The variables in this figure are non-dimensionalized according to (3.15) and (2.50). These modes have $s_i = 0$ i.e., s is real. The curves $\beta_* = 2.571$ and 0.0634 correspond to the marginally stable situation defined by (2.52).

A main conclusion resulting from our analysis is that zonostrophic instability is suppressed if β_* is either too large or too small e.g., in Figure 2.4 the flow is stable if $\beta_* > 2.571$ or if $\beta_* < 0.0634$.

The marginal stability condition in (2.52), which is equivalent to the requirements

$$s(m;\beta_*,\mu_*) = 0\,, \quad \text{and} \quad \partial_m s(m;\beta_*,\mu_*) = 0\,, \tag{2.53}$$

defines a "critical curve" in the (β_*,μ_*)-parameter plane. This curve, $\mu_* = \mu_*^{\mathrm{c}}(\beta_*)$ is shown in the upper panel of Figure 2.5. The solution $(\mathcal{Z},U) = (\mathcal{Z}_{\mathsf{H}},0)$ is linearly unstable in the region below the critical curve. The peak of the critical curve is $0.2464 = \mu_*^{\mathrm{c}}(0.65)$. This peak defines the "most unstable" point in the (β_*,μ_*)-parameter space i.e., the largest value of drag μ_* at which the homogeneous solution loses stability. The lower panel of Figure 2.5 shows the wavenumber $m^{\mathrm{c}}(\beta_*)$ of the incipient instability i.e., the wavenumber determined by simultaneously satisfying

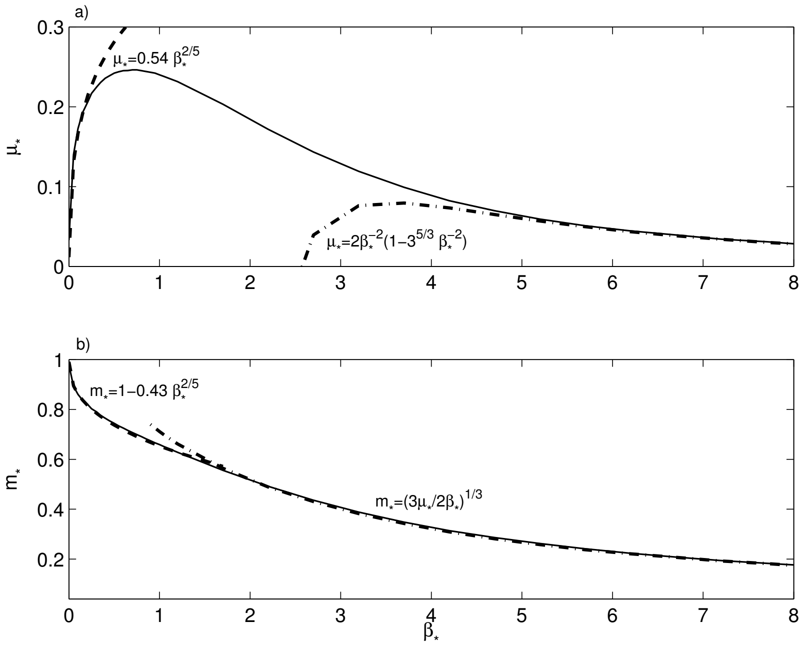

Figure 2.5: (a) The critical curve, $\mu_*^{\mathrm{c}}(\beta_*)$ (solid line); linear zonostrophic instability occurs in the region below the critical curve. (b) The wavenumber on the critical curve, $m^{\mathrm{c}}(\beta_*)$ (solid line) i.e., the most linearly unstable wavenumber. Asymptotic approximations for the critical curve and the most unstable wavenumber based on $\beta_* \gg 1$ (dash-dot) and $\beta_* \ll 1$ (dash) are shown in both panels.

the two equations in (2.53).

2.4.4 Approximations to the neutral curve with large and small β_*

Also shown in Figure 2.5 are analytic approximations in the complementary limits $\beta_* \ll 1$ and $\beta_* \gg 1$. These results are obtained via asymptotic analysis of the integral $Q(\chi, n)$ in (2.46), and simplification of the dispersion relation (2.51) (see Appendix E). If $\beta_* \ll 1$ then the critical curve is

$$\mu_*^{\mathrm{c}}(\beta_*) = \left(\frac{3}{64}\right)^{1/5} \beta_*^{2/5} + O\left(\beta_*^{4/5}\right) , \tag{2.54}$$

with wavenumber

$$m_*^{\mathrm{c}}(\beta_*) = 1 - 0.43\beta_*^{2/5} + O\left(\beta_*^{4/5}\right) . \tag{2.55}$$

In the complementary limit $\beta_* \gg 1$, the approximation to the critical curve is

$$\mu_*^{\mathrm{c}}(\beta_*) = \frac{2}{\beta_*^2}\left(1 - \frac{3^{5/3}}{\beta_*^2}\right) + O\left(\beta_*^{-6}\right) , \tag{2.56}$$

with wavenumber

$$m_*^{\mathrm{c}}(\beta_*) = \frac{3^{1/3}}{\beta_*} + O\left(\beta_*^{-3}\right) . \tag{2.57}$$

The lower panel of Figure 2.5 shows that linear zonostrophic instability is spectrally nonlocal only in the limit $\beta_* \to \infty$: in that case the most unstable wavenumber is much less than the forced wavenumber k_f, implying a scale separation between the scales at which energy is injected and the scale at which jets initially form. In the other limit $\beta_* \to 0$ the linearly unstable wavenumber is close to k_f.

2.4.5 The small wavenumber structure of the growth rate

The structure of the dispersion relation at small m provides insight into the nature of zonostrophic instability. Looking at Figure 2.4, we anticipate that

$$s = -\mu_* + \eta_2 m^2 + \eta_4 m^4 + O\left(m^6\right) , \tag{2.58}$$

where $\eta_2 > 0$ might explain the increase in s that results in the instability with $s > 0$. This would be a "negative-viscosity instability", which is the interpretation offered by *Farrell and Ioannou* [2007] and *Bakas and Ioannou* [2013, 2011].

However there is a small surprise: from (2.138) we find that the expansion of the dispersion relation (2.51) around $m = 0$ is:

$$s = -\mu_* + \frac{3\beta_*^2}{8\mu_*^4}\, m^4 + O\left(m^6\right) . \tag{2.59}$$

i.e., the term η_2 in (2.58), corresponding to viscosity, is identically zero. Instead, the instability is associated with a destabilizing *hyperviscous* term i.e., the Reynolds stresses are related to the zonal mean flow by

$$\overline{u'v'} = -\frac{3\beta_*^2}{8\mu_*^4}\,\frac{\partial^3 U}{\partial y^3} , \tag{2.60}$$

leading to the small-m growth rate in (2.59). We analyze this curious situation further in Section 2.5 and show that $\eta_2 = 0$ follows from the assumed isotropy of the forcing i.e., $\eta_2 = 0$ is not a special property of the particular model in (2.48). The conclusion is that zonostrophic instability requires anti-frictional momentum fluxes, and in the small-m limit this anti-friction is hyperviscous.

In recent work *Bakas and Ioannou* [2013, 2011] reach a different conclusion viz., that the anti-frictional effect resulting in nonzero Reynolds stress is equivalent to non-zero and positive η_2, and that the hyper-viscous coefficient η_4 is negative and therefore stabilizing. We believe that these differences may result from a different choice of forcing Ξ. *Bakas and Ioannou* [2013, 2011] use an anisotropic forcing, while our conclusion above is specifically for isotropic forcing. The importance of isotropy to our conclusion is underscored in the section 2.5.

2.5 Isotropy and zero eddy viscosity

In the discussion surrounding (2.59) we observed that the term in the zonostrophic dispersion relation corresponding to the eddy viscosity is zero. This result emerges from the analysis of a complicated dispersion relation and surely deserves a more fundamental explanation, or at least another explanation. Thus in this section we more directly obtain the eddy viscosity of an isotropically forced QL β-plane shear flow, and show that the result is identically zero.

The eddy viscosity is obtained by calculating the Reynolds stresses in a situation where there is good scale separation between a shear flow and eddies. The best possible scale separation is achieved by considering a Couette flow, $U_n = \gamma y_n$, and in this case the CE2 correlation equation (2.31) collapses to

$$\gamma y \partial_x \mathcal{Z} - 2\beta \partial_{\bar{y}} \partial_x \partial_y \Psi = \Xi(x, y) - 2\mu \mathcal{Z} \, . \tag{2.61}$$

For the moment we assume general forcing i.e., there is no restriction to isotropic forcing (yet).

The eddy viscosity ν_e is defined by the relation

$$\nu_\mathrm{e} \stackrel{\mathrm{def}}{=} -\gamma^{-1} \, \overline{u'v'} \, . \tag{2.62}$$

The goal is to solve (2.61) and obtain the Reynolds stress $\overline{u'v'}$ by evaluating Ψ_{xy} at zero separation e.g., as in (2.33). The eddy viscosity then follows from the definition (2.62).

We expect that ν_{e} defined above is equal to the coefficient η_2 in (2.58). In the $m \to 0$ limit, the modal solution in (2.44) varies on the length scale m^{-1}, which is much greater than the length scale of the forcing, viz., k_f^{-1}. Thus on the scale of the forcing, the growing zonal disturbance resembles the Couette flow [1] (except at the "shearless" points, where $U_y = 0$). By calculating the Reynolds stress in this situation one can anticipate the low-wavenumber structure of the dispersion relation. This reasoning is identical to methods in kinetic theory by which the molecular shear viscosity is calculated.

2.5.1 A solution of the correlation equation

We can simplify (2.61) with $\mathcal{Z} = \mathcal{Z}(x, y)$ i.e., by looking for a solution independent of $\bar{y}$:

$$\gamma y \partial_x \mathcal{Z} = \Xi(x, y) - 2\mu \mathcal{Z} \,. \tag{2.63}$$

This exact reduction is surprising because the β-effect is removed from the problem. Equation (2.63) can be solved straightforwardly as an ordinary differential equation in x. However to make contact with a large literature on sheared disturbances, it is instructive to consider the initial value problem

$$F_t + \gamma y \partial_x F = -2\mu F \,, \tag{2.64}$$

with the initial condition

$$F(x, y, 0) = \Xi(x, y) \,. \tag{2.65}$$

The solution of the steady problem (2.63) is then obtained as

$$\mathcal{Z}(x, y) = \int_0^\infty F(x, y, t) \, \mathrm{d}t \,. \tag{2.66}$$

---

[1] There is also uniform advection by the zonal flow. But that sweeping is eliminated by the difference $U_1 - U_2$ in the correlation equation (2.31), and is therefore inconsequential to Reynolds stresses.

Thus, solving the initial value problem for F, the vorticity correlation function is written as the time integral of a sheared disturbance:

$$\mathcal{Z}(x,y) = \int_0^\infty \mathrm{e}^{-2\mu t}\, \Xi\,(x - \gamma t y, y)\, \mathrm{d}t\,. \tag{2.67}$$

2.5.2 The Reynolds stresses

To obtain the correlation function Ψ from $\mathcal{Z}$ we must solve the two-dimensional biharmonic equation $\nabla^4\Psi = \mathcal{Z}$, which is accomplished with the Green's function defined by $\nabla^4 G = \delta(x)\delta(y)$, or $\tilde{G}(h) = h^{-4}$, or

$$G(x,y) = \frac{r^2}{8\pi}\left(\ln r - 1\right)\,. \tag{2.68}$$

With $G(x,y)$ in hand, we have

$$\Psi(x,y) = \iint G(x-x', y-y')\mathcal{Z}(x',y')\, \mathrm{d}x'\mathrm{d}y'\,. \tag{2.69}$$

The Reynolds stress now follows by evaluating Ψ_{xy} at zero separation, or

$$\overline{u'v'} = \frac{1}{4\pi}\iint \frac{xy}{x^2+y^2}\,\mathcal{Z}(x,y)\,\mathrm{d}x\,\mathrm{d}y\,. \tag{2.70}$$

This is a very convenient and general expression for the Reynolds stresses $\overline{u'v'}$ in terms of the vorticity correlation function $\mathcal{Z}(x,y)$.

Substituting (2.67) into (2.70) results in a triple integral. To disentangle this, exchange the order so that t-integral is last, and in the inner x and y integrals "unshear" the correlation function with the coordinate change

$$x_1 = x - \gamma y t\,, \qquad y_1 = y\,. \tag{2.71}$$

After these maneuvers the Reynolds stress is

$$\overline{uv} = \frac{1}{4\pi}\int_0^\infty \mathrm{e}^{-2\mu t}\Sigma(t)\,\mathrm{d}t\,, \tag{2.72}$$

where

$$\Sigma(t) \overset{\text{def}}{=} \iint \frac{(x_1+\gamma t y_1)y_1}{(x_1+\gamma t y_1)^2 + y_1^2}\,\Xi\,(x_1,y_1)\,\mathrm{d}x_1\mathrm{d}y_1\,. \tag{2.73}$$

Now we restrict attention to isotropic forcing i.e.,

$$\Xi(x_1,y_1) = \Xi\left(\sqrt{x_1^2+y_1^2}\right)\,. \tag{2.74}$$

Then in polar coordinates, the double integral in (2.73) factors:

$$\begin{aligned}\Sigma(t) &= \oint \frac{(\cos\theta + \gamma t \sin\theta)\sin\theta}{(\cos\theta+\gamma t\sin\theta)^2 + \sin^2\theta}\,\mathrm{d}\theta \times \int_0^\infty \Xi(r) r \mathrm{d}r\,,\\ &= \frac{2\pi\,\gamma t}{4+(\gamma t)^2} \times \int_0^\infty \Xi(r)\, r\mathrm{d}r\,,\\ &= 0\,. \end{aligned} \tag{2.75}$$

The final line follows from the constraint (2.42), and implies that $\overline{u'v'} = 0$. That is, the eddy viscosity ν_e is zero.

We remark that the constraints in (2.42) and (2.43) are required so that correlation function Ψ on the left of (2.69) decays as $r \to \infty$, despite the $r \to \infty$ divergence of the Green's function $G(r)$ in (2.68). In the convolution integral on the right of (2.69), the large-r divergence of G is shielded by zero integrals of the vorticity correlation function $\mathscr{Z}$, which follows from the integral constraints on Ξ in (2.42) and (2.43).

There are two important caveats associated with the conclusion that $\nu_\mathrm{e} = 0$: the stochastic forcing is isotropic and dissipation is provided only by Ekman drag. Relaxing either or both of these assumptions might result in non-zero ν_e.

2.5.3 The kinetic energy density

The energy power integral for the β-plane Couette flow problem considered here is obtained by first rewriting (2.63) as

$$\gamma\nabla^2\left(y\nabla^2\partial_x\Psi - 2\partial_x\partial_y\Psi\right) = \nabla^4 A - 2\mu\nabla^4\Psi\,. \tag{2.76}$$

Canceling a Laplacian, and evaluating the result at zero separation, one obtains[2]

$$\gamma\overline{u'v'} = \varepsilon - \mu\left(\overline{u'^2} + \overline{v'^2}\right)\,. \tag{2.77}$$

The left hand side is the transfer of energy between the eddies and the Couette flow, which is zero because $\overline{u'v'} = 0$. Therefore the statistically energy balance is between dissipation due to drag and the rate of working of the random force that

---

[2] The rate of energy injection is $\varepsilon = -\frac{1}{2}\nabla^2 A|_0$; see, for example, the model forcing in (2.47).

drives the eddies. Remarkably, because the Reynolds stresses are zero, the eddy kinetic energy of the statistically steady flow is $\varepsilon/(2\mu)$, independent of both β and γ.

2.5.4 Discussion

To a certain extent the result $\nu_{\mathrm{e}} = 0$ is anticipated in the literature on sheared disturbances. *Shepherd* [1985] showed that an isotropic initial distribution of Rossby waves maintains a constant energy density, despite shearing by a Couette flow; see also *Farrell and Ioannou* [1993b] and *Holloway* [2010]. The solution in (2.67), with the isotropic initial condition in (2.65), is essentially a time integral of Shepherd's solution of the sheared-disturbance problem with an isotropic initial condition.

Via direct numerical simulation (but with $\beta = 0$), *Cummins and Holloway* [2010] have recently shown that the eddy-eddy nonlinearity, EENL, is essential in producing nonzero Reynolds stresses from Couette-sheared eddies. *Cummins and Holloway* [2010] identify the essential role of EENL as restoration of isotropy at high wavenumbers. Moreover, as a result of nonlinearly restored isotropy, the eddy viscosity ν_{e} is robustly *positive*, and thus cannot serve as an explanation of zonostrophic instability. Whatever the sign of ν_{e}, an unfortunate consequence of (2.9) is that restoration of isotropy at small scales is absent in QL dynamics, and not represented in the ensemble-averaged dynamics CE2.

2.6 Zonation in QL and NL solutions

We now turn to numerical solutions for a comparison between the full nonlinear system, the quasilinear system and the predictions of CE2. In these calculations the resolution is 512×512, and we use the ETDRK4 time-stepping scheme [*Cox and Matthews*, 2005]. In addition to the control parameters β_* and μ_* defined in (3.15), there is a third control parameter which is the size of the domain relative to the forced wavenumber k_f: in our computations the domain is a doubly periodic square $2\pi L \times 2\pi L$, with $k_f L = 32$. Thus there is scale separation between

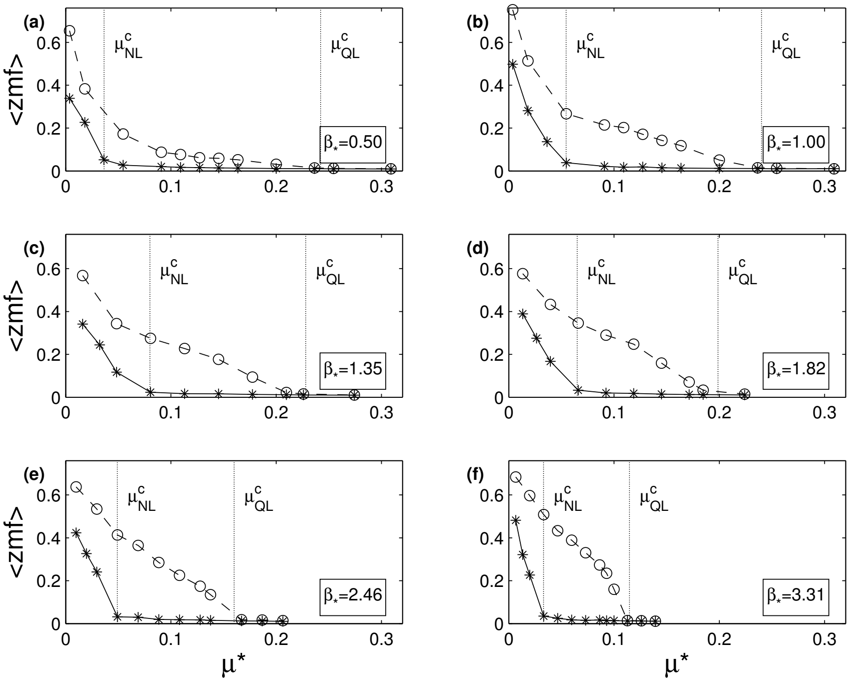

Figure 2.6: The time-averaged zonal mean energy fraction $\langle \mathrm{zmf} \rangle$ as a function of μ_*, with β_* fixed as indicated in the bottom right corner of each panel. QL simulations are indicated by $\circ$ and NL solutions by $*$.

the forcing and the domain.

We have obtained about 150 QL and NL numerical solutions, with the planetary vorticity gradient in the range

$$0.1 \leq \beta_* \leq 3.3\,,$$

and the drag parameter in the range

$$0.0051 \leq \mu_* \leq 0.309\,.$$

In this section we use these solutions to compare QL and NL solutions, and assess the validity of the CE2 linear stability analysis.

2.6.1 The onset of zonation in NL and QL solutions

Shown in the bottom panel of Figure 2.3 is the evolution of the fraction of kinetic energy in the zonal mean flow,

$$\mathrm{zmf}(t) \overset{\mathrm{def}}{=} \frac{\int U^2 \,\mathrm{d}a}{\int U^2 + u'^2 + v'^2 \,\mathrm{d}a}\,. \tag{2.78}$$

$\int \cdots \mathrm{d}a$ above denotes the area integral over the entire domain. The index $\mathrm{zmf}(t)$ is a gross measure of the strength of the zonal mean flow. The time average, denoted by $\langle \mathrm{zmf} \rangle$, is computed by averaging over an interval $t_1 < t < t_1 + 10/\mu$, where typically $2\mu t_1 > 40$. This long spin-up ensures that statistical equilibrium has been achieved and is consistent with the equilibration time suggested by *Galperin et al.* [2006].

The index $\langle \mathrm{zmf} \rangle$ is used to classify the flow. Figure 2.6 summarizes a suite of QL and NL calculations in which the drag parameter μ_* is varied at fixed β_*. The onset of zonation is indicated by the increase in $\langle \mathrm{zmf} \rangle$. The dotted lines marked μ^c_{QL} correspond to the critical curve in the upper panel of figure 2.5; these analytic predictions compare well with the increase in $\langle \mathrm{zmf} \rangle$ in the QL numerical solutions. The dotted lines marked μ^c_{NL} in Figure 2.6 are eyeball estimates of the onset of NL zonation.

The onset of zonostrophic instability requires significantly smaller values of μ_* in the NL case than in the QL case: in Figure 2.6 the ratio $\mu^c_{\mathrm{QL}}/\mu^c_{\mathrm{NL}}$ is as large as five. Thus the QL system is much more unstable than the NL system. Regarding this quantitative difference between NL and QL, we recall that QL (and CE2) is an approximation based on dropping the eddy-eddy nonlinearity. This approximation is most defensible when the mean flow is very strong i.e., in cases where the zonal mean flow contains almost all of the energy. Therefore CE2 is not likely to be quantitatively accurate near the linear stability boundary, where the zonal mean flow is weak or nonexistent. The comparison in Figure 2.6 is thus a worst case test of CE2. How, or if, CE2 might be improved to account for the missing eddy-eddy nonlinearity in this weak mean-flow regime is an open issue.

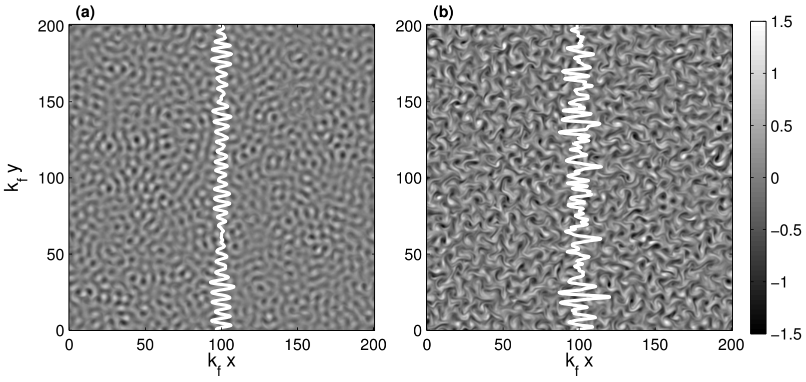

Figure 2.7: Snapshots of the vorticity $\zeta(x, y, t)$ with overlaid zonally averaged vorticity $-U_y(y, t)$ (solid white curve) with (a) $\mu_* = 0.309$ and, (b) $\mu_* = 0.0545$. Both snapshots are at non-dimensional time $2\mu t = 25$, after spin-up from rest, and $\beta_* = 1$.

2.6.2 Zonostrophically stable NL solutions

Figure 2.7 shows two NL solutions which are zonostrophically stable i.e., these solutions have

$$\mu^c_{\mathrm{NL}} < \mu_* , \tag{2.79}$$

and $\langle \mathrm{zmf} \rangle \approx 0$. In the left panel of Figure 2.7 the drag is so heavy that the approximate dominant balance in (2.1) is $\mu\zeta \approx \xi$ and the vorticity field closely resembles a snapshot of the forcing ξ.

Figure 2.8 compares energy spectra of statistically steady QL and NL solutions. With strong drag (i.e., $\mu_* = 0.309$) only the directly forced wavenumbers are significantly excited. As μ_* is reduced there is transfer of energy to small wavenumbers. In the NL case the transfer of energy to wavenumbers smaller than k_f is the due to the inverse energy cascade. In the QL case the excitation of small wavenumbers is due only to shearing by the zonal mean flow. Comparing QL and NL solutions at the same value of μ_*, one sees from Figures 2.8(b) and 2.8(d), that there is significantly more low-wavenumber eddy energy in the NL cases. Yet the zonal mean energy is always stronger in the QL case. There is no clear association between the inverse energy cascade and zonation.

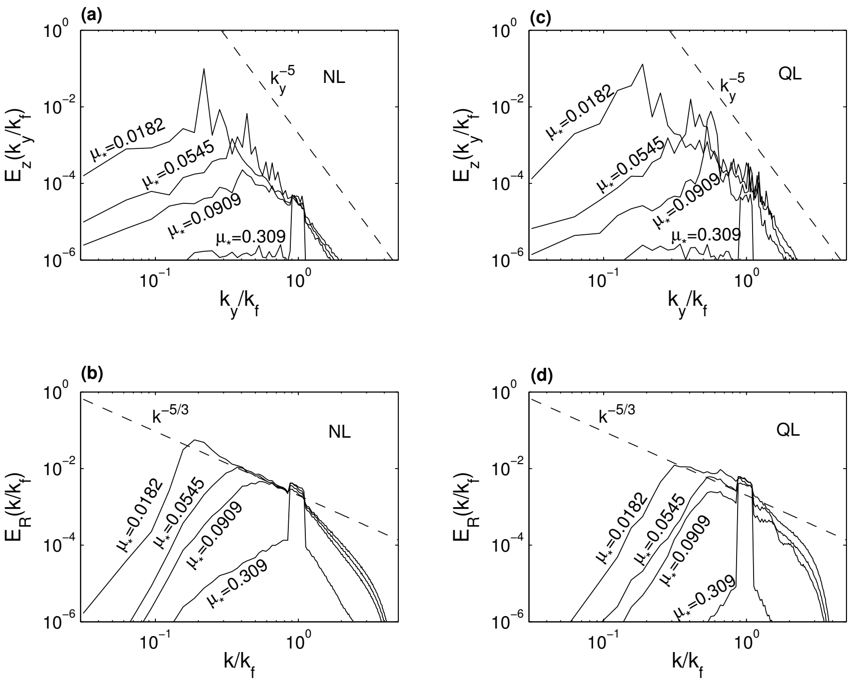

Figure 2.8: The upper panels show the zonal spectrum, $E_{\mathrm{Z}}(k_y/k_f)$, for QL and NL solutions with $\beta_* = 1$. The lower panels show the residual spectrum $E_{\mathrm{R}}(k/k_f)$, defined as the angularly averaged spectrum after removal of the "zonal modes" with $k_x = 0$. The largest peak in $E_{\mathrm{Z}}(k_y/k_f)$ defines the wavenumber m_{Z}, even if there are no quasi-steady steady zonal jets e.g., as in the NL simulation with $\mu_* = 0.0545$ in panel (a).

The NL solution shown in right panel of Figure 2.7 with $\mu_* = 0.0545$ has an eddy energy spectrum in Figure 2.8 (b) exhibiting the beginning of $-5/3$ range. However this solution has $\langle \mathrm{zmf} \rangle \approx 0$ and thus serves as example of an isotropic, spatially homogeneous, weakly turbulent, β-plane flow, without jets. To activate zonostrophic instability the drag μ_* must be reduced e.g., to $\mu_* = 0.0182$ in Figures 2.1 and 2.8.

2.6.3 The jet scale

If zonation occurs, as evinced by significantly nonzero values of $\langle \text{zmf} \rangle$, then by counting the number of distinct jets one can reliably estimate[3] a jet wavenumber m_{J}. For example, in Figure 2.1 there are seven jets and therefore $m_{\text{J}}/k_f = 7/32$.

However we noticed that there are cases without jets in which the zonal energy spectrum $E_{\text{Z}}(k_y/k_f)$ has a strong peak: an example is the $\mu_* = 0.0545$ solution in Figure 2.7(b): the corresponding zonal energy spectrum in Figure 2.8(a) has a distinct peak even though there are no zonal jets. In cases like this, we report a wavenumber m_{Z} which is the peak of the zonal spectrum $E_{\text{Z}}(k_y/k_f)$. In cases where there are strong jets we invariably find that $m_{\text{Z}} \approx m_{\text{J}}$. It is interesting to compare m_{J} and m_{Z} with a Rhines wavenumber defined as

$$m_{\text{Rh}} = \sqrt{\frac{\beta}{2V_{\text{RMS}}}}\,, \tag{2.80}$$

where the root mean square velocity is

$$V_{\text{RMS}}^2 \overset{\text{def}}{=} \left\langle \frac{1}{(2\pi L)^2} \int U^2 + u'^2 + v'^2 \,\mathrm{d}a \right\rangle . \tag{2.81}$$

We investigated other choices for the velocity in the Rhines wavenumber e.g., *Rhines* [1975] advocated the RMS of v'. We found however that V_{RMS} gave the best estimate of the NL jet spacing at small values of μ_*. An advantage of V_{RMS} is that the energy power integral[4] can be used to express V_{RMS} in terms of external parameters as

$$\varepsilon \approx \mu V_{\text{RMS}}^2 \,. \tag{2.82}$$

The relation above applies with an error (due to hyperviscous dissipation) of less than 5% in our simulations. Substituting (2.82) into (2.80) one has

$$m_{\text{Rh}} \approx k_f \left(\frac{\beta_* \mu_*^{1/2}}{2} \right)^{1/2} . \tag{2.83}$$

---

[3] In certain cases the system may be transitioning between a state with n and $n+1$ jets. Following *Panetta* [1993], we then count $n + \frac{1}{2}$ jets; no other fractional values are permitted.

[4] From (2.3), the exact energy power integral is $\langle \psi\xi + \mu|\boldsymbol{\nabla}\psi|^2 + (-1)^{n-1}\nu_n|\boldsymbol{\nabla}^{n-1}\zeta|^2\rangle = 0$, where $\langle\rangle$ is both a domain integral and a time average.

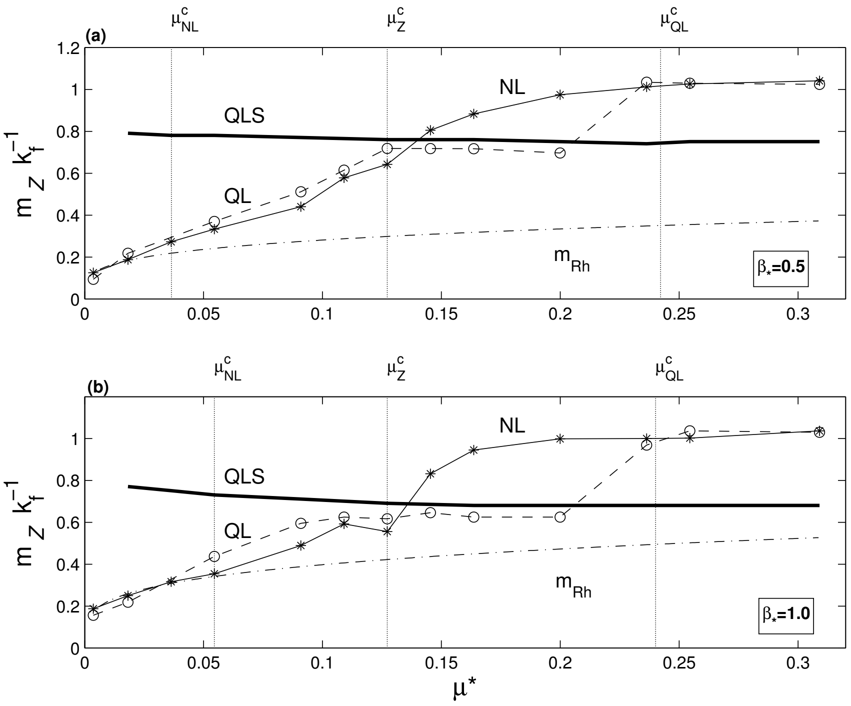

Figure 2.9: A summary of zonal wavenumbers (jet scales) for solutions with (a) $\beta_* = 0.5$ and (b) $\beta_* = 1$. The dot-dashed curve is the Rhines wavenumber defined in (2.83). The solid curve labelled QLS is most unstable wavenumber calculated from the dispersion relation (2.51). The NL solutions are indicated by $*$ and the QL solutions by $\circ$.

Figure 2.9 compares the zonal wavenumber m_{Z} obtained from QL and NL solutions with the Rhines wavenumber on the right of (2.83), and with the most-unstable wavenumber obtained from the linear stability analysis of section 2.4. In Figure 2.9 we show only the $\beta_* = 1$ and $\beta_* = 0.5$ solutions: solutions with other values of β_* exhibit a broadly similar dependence of m_{Z} on μ_*.

At large values μ_* only the directly forced modes are excited, and consequently $m_{\mathrm{Z}} \approx k_f$ in both the QL and NL cases. At the critical value $\mu_* = \mu^c_{\mathrm{QL}}$ in Figure 2.9, the QL solutions undergo zonostrophic instability, and close to this transition, e.g., at $\mu_* = 0.2$ and 0.165 in Figure 2.9(a), the QL m_{Z} agrees with the analytic result from Figure 2.5. In this regime the NL solutions start to develop an

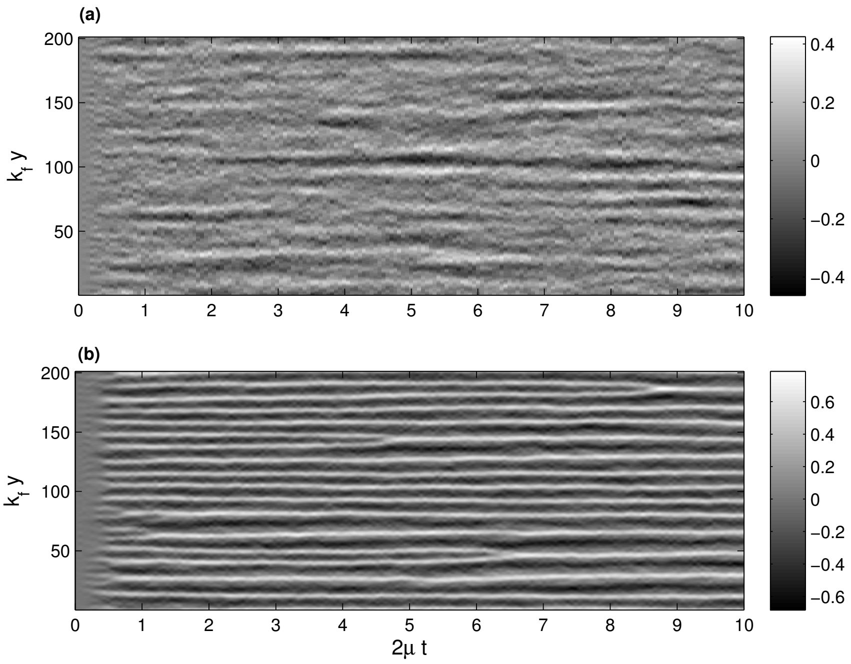

Figure 2.10: Hovmöller diagrams for the (a) NL and (b) QL runs with β_*=1.0 and $\mu_* = 0.0545$. The NL run corresponds to the vorticity snapshot shown in Fig. 2.7(b) and shows zonal "streaks". In panel (b) the QL jets initially appear at a wavenumber predicted by linearization of CE2. Then successive mergers result in an increase in jet spacing.

inverse cascade (but without exciting zonal jets) and the NL m_{Z} begins to decrease.

There is an interesting transition at $\mu_* = \mu_Z^c$ in Figure 2.9. At this point the QL and NL zonal wavenumbers are equal, and as μ_* is reduced the QL and NL wavenumbers are locked together. At $\mu_* = \mu_{\mathrm{NL}}^c$ in Figure 2.9 the NL solutions finally become zonostrophically unstable, resulting in NL jets and significantly non-zero values of NL $\langle \mathrm{zmf} \rangle$. At the smallest value of μ_* in Figure 2.9, which corresponds to the runs in Figures 2.1 and 2.2, the QL and NL wavenumbers are almost equal, and are estimated roughly by m_{Rh}.

In Figure 2.9 the analytic result QLS agrees with the observed QL jet scale only when μ_* is not too far from the linear stability boundary μ_{QL}^c. In the strongly unstable regime, with μ_* significantly less than μ_{QL}^c, the observed wavenumber m_{Z}

is much smaller than the most unstable wavenumber predicted by linear theory. This increase in the QL jet scale is a result of merging jets which initially appear with a spacing which is well predicted by the linear theory. This phenomenology begins at about $\mu_* = \mu_Z^c$ and is illustrated in Figure 2.10.

Figure 2.10(a) shows the Hovmöller diagram of the jetless NL solution from Figure 2.7(b). There is no zonation and $U(y,t)$ shows "streaks" rather than jets. These streaks are not strong relative to the turbulent eddy field i.e., $\langle \text{zmf} \rangle \approx 0$. The corresponding zonal energy spectrum in Figure 2.8(a) exhibits a strong peak, which is a signature of these transient zonal steaks.

Figure 2.10(b) shows the QL case in which jets initially appear with a relatively small meridional spacing predicted by linear theory, followed by a sequence of mergers so that the mature flow has m_{Z} much less than the most linearly unstable wavenumber. The QL jet-merging phenomenology, which is effectively a one-dimensional inverse cascade, is very similar to the "Cahn-Hilliard" solutions obtained by *Manfroi and Young* [1999] from a model of deterministically forced zonation.

2.6.4 The small drag regime

The flows in Figure 2.1 and 2.2 have relatively light damping and both flows have organized jets containing a substantial fraction of the total kinetic energy. Figure 2.11 shows the time-averaged zonal mean-flow, $\langle U \rangle$ and the corresponding potential vorticity (PV) gradient, $\beta_* - \langle U_{yy} \rangle$. In Figure 2.2 the QL jets are almost symmetrical in the zonal direction, in contrast to the NL jets[5]. But the QL jets are not perfectly symmetric: the PV gradient in Figure 2.11(b) reveals the QL east-west asymmetry. The NL PV gradient is positive for all y and thus the NL jets are stable according to the Rayleigh-Kuo criterion. The QL PV gradient in Figure 2.11(b) reverses sign on the flanks of the eastward jet, and also at the centers of the westward jets. Nonetheless the QL zonal mean flow shows no indication

---

[5] If $\beta = 0$ then the equations of motion are invariant under $y \to -y$ and $\psi \to -\psi$. This symmetry, which induces $u \to u$, is broken in both QL and NL by non-zero β. This explains the characteristic east-west asymmetry of $U(y,t)$ on the β-plane

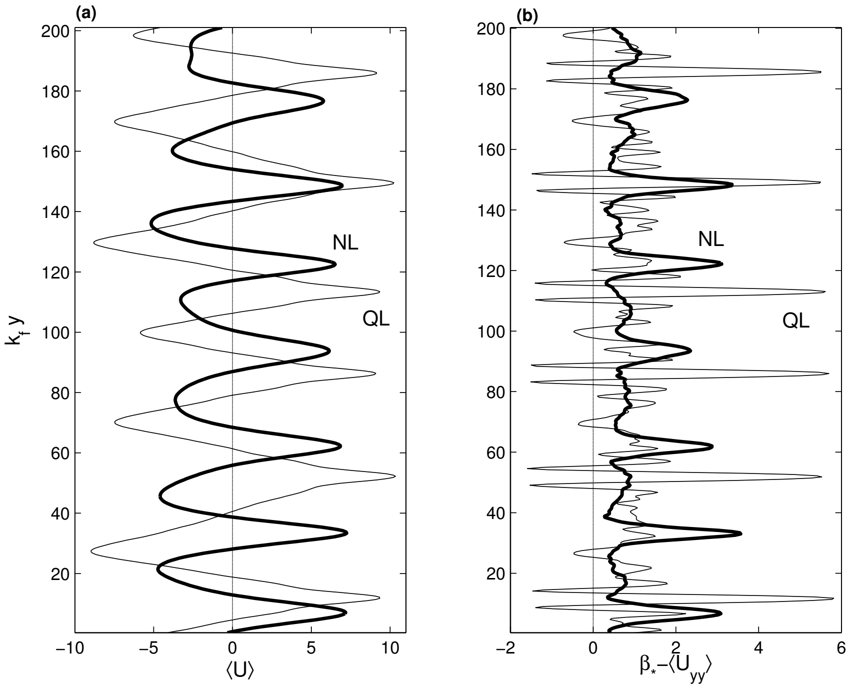

Figure 2.11: Comparison of zonal mean velocity profiles of the $\beta_* = 1$ NL and QL runs in Figures 2.1 and 2.2.

of barotropic instability i.e., the deep spikes with $\beta_* - \langle U_{yy} \rangle < 0$ are permanent features of the QL zonal mean flow even after time averaging.

Via integration of their SSST system, *Farrell and Ioannou* [2007] report equilibrated zonal mean flows with much stronger east-west asymmetry than the QL flow in Figure 2.11 e.g., see their figures 8 and 9. There are at least[6] two non-dimensional parameters, β_* and μ_*, and the jet profile depends on both of these. We will not attempt to characterize this variation systematically. However to make some contact with the strong-forcing limit considered by *Farrell and Ioannou* [2007] we consider the QL solution in Figure 2.10(b) and in Figure 2.12(a), and increase the energy injection rate ε by a factor of one thousand, while holding β, μ and k_f approximately fixed. Then from (3.15), the control parameters β_* and μ_* are each reduced by a factor of ten. The time averaged zonal-mean profile of this

---

[6] *Farrell and Ioannou* [2007] also employ a forcing with a different correlation functon than our isotropic choice.

strongly forced solution is shown in Figure 2.12(b), and exhibits the parabolic velocity profile seen in the NL run in Figure 2.1: there are fast eastward jets with sharp gradients and broad westward jets with smaller PV gradients. Also, the time averaged QL jet-profile in Figure 2.12(b) is more asymmetric than the weaker forced QL jet shown in Figure 2.12(a), that has a forcing that is a factor of 10 smaller. In order to quantify the jet asymmetry, we use the ratio

$$\alpha(\beta_*, \mu_*) = \frac{U_{\max}}{|U_{\min}|}\,, \tag{2.84}$$

where $U_{\max}$ and $U_{\min}$ are the maximum and mimimum values attained in the zonal-mean velocity profile. By increasing the forcing strength by a factor of 1000, the jet asymmetry increases from $\alpha = 1.25$ in Figure 2.12(a) to $\alpha = 1.56$ for the profile in Figure 2.12(b). This is smaller than the "ideal", marginally stable (i.e. $\beta - U_{yy} = 0$ everywhere except at the eastward jet where the PV jumps) profile considered in *Danilov and Gurarie* [2004], which has $\alpha = 2$.

Thus, although a detailed study of QL jet asymmetry is not a focus of the present work, our QL numerical solutions are thus generally consistent with the equilibrated SSST jets presented in *Farrell and Ioannou* [2007].

2.6.5 Discussion of the eddy-eddy nonlinearity

An important effect of eddy-eddy nonlinearity is the stirring of PV, producing an exponential-in-time reduction in the length scale of vorticity fluctuations. Eddy-driven stirring is removed from the QL system by (2.9): shearing by $U(y,t)$ is the only scale-reduction mechanism acting on the QL eddy vorticity. The small-scale structure evident in the QL PV gradient in the right panel of Figure 2.11 may reflect the relative inefficiency of shearing by $U(y,t)$ at removing vorticity fluctuations.

Further differences in the jet structure evident in Figure 2.11 can be explained by meandering of the NL jets, so that the zonal average reduces the sharpness of the NL PV gradient. The spectral signature of the NL jet meanders is a high energy mode at $(k_x, k_y) = (1/32, 6/32)k_f$ in the two-dimensional NL spectrum; this same mode is only weakly excited in the QL spectrum. The excitation

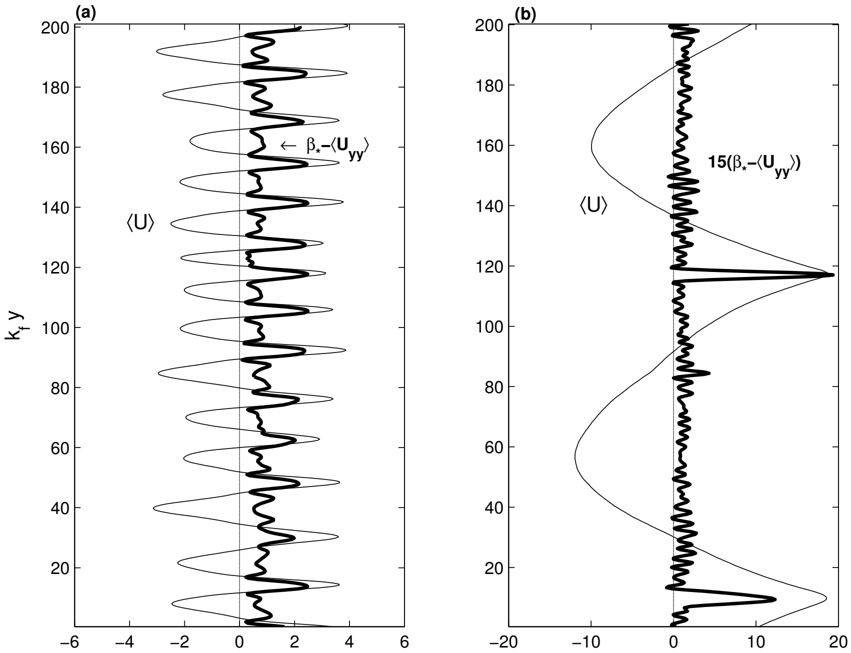

Figure 2.12: Comparison of time-averaged zonal-mean velocity profiles (thin lines) of QL runs. Panel (a) is the solution from Figure 2.10(b) with $\beta_* = 1.0$ and μ_*=0.054 and panel (b) is the strongly forced solution with $\beta_* = 0.1$ and μ_*=0.005. Also plotted are the corresponding PV gradients (thick curves).

of almost-zonal modes, with a small but non-zero of value of k_x, is a well known aspect of zonation. These are called a "satellite modes" by *Danilov and Gurarie* [2004], and they correspond to a domain-scale meander of the NL jets, which is not present in the QL case.

2.7 Discussion and conclusion

A contribution of this work is the analytic development of the linearized theory of zonostrophic instability within the context of the second-order cumulant expansion (CE2) of *Marston et al.* [2008], and the stochastic structural stability theory (SSST) of *Farrell and Ioannou* [2003, 2007]. These statistical formulations are equivalent to the correlation dynamics derived in section 2.3, and that physical-space formulation, in terms of partial differential equations for the correlation functions Ψ and $\mathcal{Z}$, provides some insight into the mathematical structure of CE2/SSST.

In the upper panel of Figure 2.5 we display the curve of neutral zonostrophic stability in the (β_*, μ_*)-parameter plane obtained by solution of linearized CE2 dynamics. We have shown that with isotropic forcing zonostrophic instability is not a negative-viscosity instability: the hallmark of a negative-viscosity instability is that at the stability boundary the most unstable wavenumber is zero. The deterministic model of anisotropically forced β-plane zonation analyzed by *Manfroi and Young* [1999] provides a bona fide example of the negative-viscosity case. Instead, for the isotropically and stochastically forced model analyzed here, the onset of zonostrophic instability is at the non-zero meridional wavenumber shown in the bottom panel of Figure 2.5; only at large β_* does this wavenumber approach zero. Moreover, in Section 2.5 we showed that with isotropic forcing the CE2 eddy viscosity ν_e is identically zero.

Comparison of QL and NL numerical solutions indicates that the CE2 linear stability boundary does not provide an accurate estimate of the onset of zonostrophic instability for NL flows. This quantitative failure of CE2 is not surprising: neglect of the eddy-eddy nonlinearity is most plausible in cases where most of the energy is in the zonal mean flow: close to the stability boundary the zonal-mean flow is only incipient. An outstanding open problem is improving CE2 to account for the missing physics in the eddy-eddy nonlinearity. Another important problem is obtaining analytic insight into the solution of the CE2 system in the regime where CE2 is likely to be valid i.e., in the strongly unstable regime where the drag μ_* is much less than the critical drag μ^c and the fraction of energy in the zonal-mean flow is substantial.

2.A Implementation of the random forcing $\xi(\boldsymbol{x}, t)$

For numerical purposes we model the δ-correlated forcing $\xi(x, y, t)$ in (2.3) using a discrete approximation. The goal is to construct a statistically isotropic and narrow band forcing localized close to a radial wavenumber k_f. Thus the forcing is confined to an annulus $\mathcal{A}$ in wavenumber space, where wavenumbers $\boldsymbol{k}$ in $\mathcal{A}$ satisfy the inequality

$$k_f + \delta k < |\boldsymbol{k}| < k_f - \delta k \,. \tag{2.85}$$

We take $\delta k = k_f/8$, so that $\mathcal{A}$ is tightly around the average radius k_f. We use a fourth-order Runge Kutta scheme, with time step δt. Implementing the Runge-Kutta scheme requires the value of the forcing not just at points in time separated by the time step δt but also at the mid-points. Some care must be exercised here though, since the Runge-Kutta scheme assumes a certain degree of smoothness of the solution. To ensure this, we use a forcing that during the n'th time step, when $(n-1)\delta t < t < n\delta t$, has the form

$$\xi(\boldsymbol{x}, t) = \sum_{\boldsymbol{k}_i \in \mathcal{A}} \{\xi_i(n-1) + [\xi_i(n) - \xi_i(n-1)]\chi_n(t)\}\, e^{i\boldsymbol{k}_i \cdot \boldsymbol{x}} \,, \tag{2.86}$$

where $\chi_n(t) \overset{\text{def}}{=} (t/\delta t) - (n-1)$ varies linearly from zero to one during the n'th time step. The coefficient $\xi_i(n)$ above is

$$\xi_i(n) = \sqrt{\frac{2\varepsilon k_f^2}{N_{\mathcal{A}} \delta t}}\; \mathrm{e}^{\mathrm{i}\phi_i(n)} \,, \tag{2.87}$$

where $N_{\mathcal{A}}$ is the number of wavevectors in $\mathcal{A}$, and $\varepsilon = -\langle \psi \xi \rangle$ is the rate of energy injection. The dependence $\xi_i(n) \propto 1/\sqrt{\delta t}$ ensures that the forcing is $\delta-$correlated in the limit $\delta t \to 0$. The phase, $\phi_i(n)$, is a random variable, chosen from a uniform distribution in $[0, 2\pi]$; the phase is set independently for each wavevector $\boldsymbol{k}_i$, and resets at the start of each time step.

The narrow-band forcing is described by the correlation function,

$$\tilde{\Xi}^b(k) = \frac{2\pi\varepsilon k_f}{\delta k} \begin{cases} 1\,, & \text{if } k_f - \delta k < k < k_f + \delta k; \\ 0\,, & \text{otherwise,} \end{cases} \tag{2.88}$$

which has the physical-space form

$$\begin{aligned} \Xi^b(r) &= \frac{\varepsilon k_f}{\delta k} \int_{k_f - \delta k}^{k_f + \delta k} J_0(kr)\, k \mathrm{d}k \,, \\ &= \frac{2\varepsilon k_f}{r^2 \delta k} \left[z J_1(z) \right]_{(k_f - \delta k) r}^{(k_f + \delta k) r} \,. \end{aligned} \tag{2.89}$$

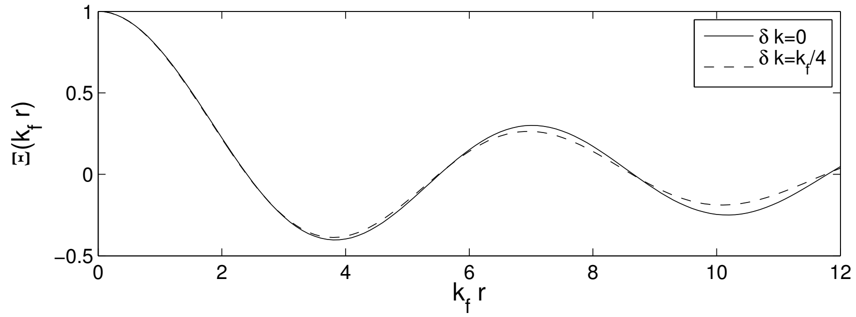

Figure 2.13: Comparison of the ring forcing, $\delta k \to 0$ (solid line) and the narrow-band forcing with $\delta k = k_f/4$ (dashed line).

A comparison of $\Xi^b(r)$ and its idealized form, $\Xi(r) \propto J_0(k_f r)$ is shown in Figure 2.13

2.B Rapid temporal decorrelation: derivation of (2.25)

The crucial assumption leading to (2.25) is that the temporal de-correlation of the forcing is rapid, as indicated by the $\delta(t_1 - t_2)$ on the right of (2.14). Operationally, this means that we might integrate (2.11) during the first time step from $t = 0$ to $t = \delta t$ as

$$\zeta'(\boldsymbol{x}, \tau) = \zeta'(\boldsymbol{x}, 0) + \sqrt{\delta t} \times \hat{\xi}(\boldsymbol{x}) + \delta t \times \mathrm{AOT}(\boldsymbol{x}, 0)\,, \tag{2.90}$$

where $\mathrm{AOT}(\boldsymbol{x}, 0)$ indicates "all other terms" in (2.11), evaluated at $t = 0$. Also in (2.90), $\hat{\xi}(\boldsymbol{x})$ is a spatial random field with correlation function

$$\Xi(x, y_1, y_2,) = \overline{\hat{\xi}(\boldsymbol{x}_1)\hat{\xi}(\boldsymbol{x}_2)}\,. \tag{2.91}$$

The forcing $\hat{\xi}$ "renovates" during each time step i.e., in the n'th time step one creates a new independent realization of $\hat{\xi}$, but always with the same spatial correlation function Ξ. According to this recipe the magnitude of $\hat{\xi}$ is independent of δt as $\delta t \to 0$, and therefore $\xi = \hat{\xi}/\sqrt{\delta t} \to \infty$ as $\delta t \to 0$. As demanded by this argument, notice that $\xi_i(n)$ in (2.87) is proportional to $1/\sqrt{\delta t}$.

Before ensemble averaging, we can multiply (2.90) evaluated at $\boldsymbol{x}_1$ with (2.90) evaluated at $\boldsymbol{x}_2$ to obtain

$$\begin{aligned}\zeta_1'(\delta t)\zeta_2'(\delta t) = \zeta_1'(0)\zeta_2'(0) + \sqrt{\delta t}\left[\zeta_1'(0)\hat{\xi}_2 + \zeta_2'(0)\hat{\xi}_1\right] \\ + \delta t\left[\hat{\xi}_1\hat{\xi}_2 + \zeta_1'(0)\mathrm{AOT}_2(0) + \zeta_2'(0)\mathrm{AOT}_1(0)\right] \\ + O\left(\delta t^{3/2}\right) ,\end{aligned} \tag{2.92}$$

where the subscript n indicates evaluation at $\boldsymbol{x}_n$ e.g.,

$$\zeta'(\boldsymbol{x}_1, \delta t) = \zeta_1'(\delta t) . \tag{2.93}$$

Upon ensemble averaging, the terms of order $\sqrt{\delta t}$ on the right of (2.92) vanish because $\hat{\xi}(\boldsymbol{x})$ is independent of $\zeta'(\boldsymbol{x}, 0)$. Thus

$$\begin{aligned}\frac{\mathcal{Z}(\delta t) - \mathcal{Z}(0)}{\delta t} =& \Xi + \overline{\zeta_1'(0)\mathrm{AOT}_2(0)} + \overline{\zeta_2'(0)\mathrm{AOT}_1(0)} \\ &+ O\left(\delta t^1\right) .\end{aligned} \tag{2.94}$$

As $\delta t \to 0$ the left hand side is the time derivative of the vorticity correlation function. The $\sqrt{\delta t}$-terms in (2.92), which prohibit a differentiable limit, are nulled in (2.94) by the ensemble average. Thus, taking the limit $\delta t \to 0$ in (2.94), we obtain the deterministic differential equation (2.23) for the evolution of the correlation function $\mathcal{Z} \equiv \overline{\zeta_1\zeta_2}$.

2.C Derivation of the dispersion relation (2.45)

The linearized equations resulting from substitution of (2.44) into (2.34) and (2.31) are

$$\begin{aligned}\left(s + 2\mu + \tfrac{1}{2}\nu m^2 - 2\nu\nabla^2\right)\hat{\mathcal{Z}} + 2i\sin\left(\frac{my}{2}\right)\Phi_{\mathsf{H}x}\,\hat{U}(m) \\ - 2im\beta\hat{\Psi}_{xy} = 0 ,\end{aligned} \tag{2.95}$$

$$\left(s + \mu + \nu m^2\right)\hat{U}(m) + im\hat{\Psi}_{xy}\big|_{x=y=0} = 0 , \tag{2.96}$$

$$\left(\nabla^2 + im\partial_y - \tfrac{1}{4}m^2\right)\left(\nabla^2 - im\partial_y - \tfrac{1}{4}m^2\right)\hat{\Psi} = \hat{\mathcal{Z}} , \tag{2.97}$$

where in (2.95)

$$\Phi_{\mathsf{H}} \overset{\text{def}}{=} \mathcal{Z}_{\mathsf{H}} + m^2\nabla^2\Psi_{\mathsf{H}} = \left(\nabla^4 + m^2\nabla^2\right)\Psi_{\mathsf{H}}\,. \tag{2.98}$$

A key intermediate step on the path to (2.95) is noting $U_1 = U\left(\bar{y} + \frac{1}{2}y\right)$ and $U_2 = U\left(\bar{y} - \frac{1}{2}y\right)$, so that with $U(y,t)$ in (2.44) one has

$$U_1 - U_2 = \; 2i\sin\left(\frac{my}{2}\right)\mathrm{e}^{im\bar{y}+st}\,\hat{U}(m) + c.c.\,. \tag{2.99}$$

Applying the Fourier transform in (2.38) to (2.95) and (2.97), one has

$$\left[2im\beta pq + h_+^2 h_-^2 s'\right]\tilde{\Psi} + ip\,\hat{U}\left(\tilde{\Phi}_{\mathsf{H}}^- - \tilde{\Phi}_{\mathsf{H}}^+\right) = 0\,, \tag{2.100}$$

$$\frac{im}{\bar{s}}\iint pq\,\tilde{\Psi}\,\frac{\mathrm{d}p\,\mathrm{d}q}{(2\pi)^2} = \hat{U}\,, \tag{2.101}$$

$$h_+^2 h_-^2\tilde{\Psi} = \tilde{\mathcal{Z}}\,. \tag{2.102}$$

In (2.100) through (2.102) we use the notation

$$h_\pm \overset{\text{def}}{=} \sqrt{p^2 + (q \pm m/2)^2}\,, \tag{2.103}$$

$$\tilde{\Phi}_{\mathsf{H}}^\pm \overset{\text{def}}{=} h_\pm^2\left(h_\pm^2 - m^2\right)\tilde{\Psi}_{\mathsf{H}}(p, q \pm m/2)\,, \tag{2.104}$$

$$\bar{s} \overset{\text{def}}{=} s + \mu + \nu m^2\,, \tag{2.105}$$

$$s' \overset{\text{def}}{=} s + 2\mu + \tfrac{1}{2}\nu m^2 + 2\nu h^2\,. \tag{2.106}$$

Eliminating $\hat{U}(m)$ between (2.100) and (2.101), we obtain the dispersion relation

$$\bar{s} = m\Lambda_-\left(s', m\right) - m\Lambda_+\left(s', m\right)\,, \tag{2.107}$$

where the functions $\Lambda_+(s',m)$ and $\Lambda_-(s',m)$ are defined by the integral

$$\Lambda_\pm(s',m) \overset{\text{def}}{=} \iint p^2 q\,\frac{h_\pm^2\left(h_\pm^2 - m^2\right)\tilde{\Psi}_{\mathsf{H}}(p, q \pm m/2)}{s'\,h_+^2 h_-^2 + 2im\beta pq}\,\frac{\mathrm{d}p\,\mathrm{d}q}{(2\pi)^2}\,. \tag{2.108}$$

Changing variables with $p \to -p$ and $q \to -q$, and using the exchange symmetry in (2.22), one finds that

$$\Lambda_-(s',m) = -\Lambda_+(s',m)\,, \tag{2.109}$$

so that the right of (2.107) is equal to $2m\Lambda_-$. Then with the change of variables $q' = q - m/2$ in the Λ_- integral, and using (2.41), one can write the dispersion relation (2.107) as

$$\bar{s} = \iint \frac{p^2\,(h_{++}^2 - h^2)\,h^2\,(h^2 - m^2)}{s'\,h^2 h_{++}^2 + i\beta p\,(h_{++}^2 - h^2)}\,\frac{\tilde{A}(p,q)}{2\mu + 2\nu h^2}\,\frac{\mathrm{d}p\,\mathrm{d}q}{(2\pi)^2}\,, \tag{2.110}$$

where $h_{++} \overset{\text{def}}{=} \sqrt{p^2 + (q+m)^2}$.

If the forcing is isotropic then $\tilde{A}(p,q) = \tilde{A}\,(h)$, and the integral on the right of (2.110) can be simplified using polar coordinates $(p,q) = h(\cos\theta, \sin\theta)$:

$$\beta^2 \bar{s} = \int_0^\infty h^4\left(h^2 - m^2\right)\frac{\tilde{A}(h)}{2\mu + 2\nu h^2}\,S\!\left(\frac{s'h^2}{\beta m}, \frac{m}{h}\right)\frac{\mathrm{d}h}{2\pi}\,, \tag{2.111}$$

where S is the function

$$S(\chi, n) \overset{\text{def}}{=} \oint \frac{\cos^2\theta\,(2\sin\theta + n)}{\chi\,(1 + 2n\sin\theta + n^2) + \mathrm{i}\cos\theta\,(2\sin\theta + n)}\,\frac{\mathrm{d}\theta}{2\pi}\,. \tag{2.112}$$

One can show that $S(\chi,n) = -S(-\chi,n) = -S(\chi,-n)$, and therefore $S(0,n) = S(\chi,0) = 0$. These symmetries are important for further work, and they are not manifest from the definition of S in (2.112). Thus we seek an alternative form with more obvious properties. The change of variables $\theta \to \theta + \pi$ results in

$$S(\chi, n) = \oint \frac{\cos^2\theta\,(-2\sin\theta + n)}{\chi\,(1 - 2n\sin\theta + n^2) - \mathrm{i}\cos\theta\,(-2\sin\theta + n)}\,\frac{\mathrm{d}\theta}{2\pi}\,. \tag{2.113}$$

The average of (2.112) and (2.113) is then

$$\begin{aligned} S(\chi,n) &= \chi n \\ &\quad\times \underbrace{\oint \frac{\cos^2\theta\,(1 + n^2 - 4\sin^2\theta)}{\left[\chi + \mathrm{i}\sin 2\theta\right]^2 + n^2\left[\chi^2(n^2 + 2 - 4\sin^2\theta) + \cos^2\theta\right]}\,\frac{\mathrm{d}\theta}{2\pi}}_{\overset{\text{def}}{=} Q(\chi,n)}\,. \end{aligned} \tag{2.114}$$

The function $Q(\chi,n)$ is manifestly an even function of n, and $\theta \to -\theta$ shows that Q is also an even function of χ.

Substituting (2.114) into (2.111) gives the dispersion relation in the form

$$\beta^2 \bar{s} = \int_0^\infty h^5\left(h^2 - m^2\right)\frac{\tilde{A}(h)\,s'}{2\mu + 2\nu h^2}\,Q\!\left(\frac{s'h^2}{\beta m}, \frac{m}{h}\right)\frac{\mathrm{d}h}{2\pi}\,. \tag{2.115}$$

If $\nu = 0$ then $s' = s + 2\mu$, and we obtain the dispersion relation in (2.45).

2.D The function $Q(\chi, n)$

In this appendix we summarize some properties of the function $Q(\chi, n)$ defined in (2.114). We first note that

$$\begin{aligned} Q(\chi, 0) &= \int_0^{2\pi} \frac{\cos^2\theta\,(1 - 4\sin^2\theta)}{(\chi + i\sin 2\theta)^2}\,\frac{\mathrm{d}\theta}{2\pi}\,, \\ &= 1 - \frac{|\chi|(2\chi^2 + 3)}{2\left(\chi^2 + 1\right)^{3/2}}\,. \end{aligned} \tag{2.116}$$

If $0 \le n^2 \le 1$ then

$$\begin{aligned} Q(0, n) &= 1 + \mathrm{Pr}\int_0^{2\pi} \frac{1}{n^2 - 4\sin^2\theta}\,\frac{\mathrm{d}\theta}{2\pi}\,, \\ &= 1\,, \end{aligned} \tag{2.117}$$

where ‘Pr’ refers to the Cauchy-principal value.

The case $\beta_* \ll 1$ requires the approximation of $Q(\chi, n)$ in the limit $\chi \to \infty$. One can expand the integrand in inverse powers of χ and integrate term by term. The first two non-zero terms are

$$\begin{aligned} Q(\chi, n) = &\frac{3}{2^3\chi^4(1 - n^2)} \\ &+ \frac{5}{2^5\chi^6}\frac{(n^4 + 2n^2 - 4)}{(1 - n^2)^3} + O\left(\chi^{-8}\right)\,. \end{aligned} \tag{2.118}$$

The case $\beta_* \gg 1$ requires the approximation of $Q(\chi, n)$ in the limit $\chi \to 0$. A somewhat laborious ‘range-splitting’ calculation shows that

$$Q(\chi, n) = 1 - \frac{3}{2}\frac{24 - 7n^2}{24 - 6n^2}|\chi| + O\left(\chi^2\right)\,. \tag{2.119}$$

Finally, if $\chi \to \infty$, with $n = 0$ then from either (2.116) or (2.118) we obtain

$$Q(\chi, 0) = \frac{3}{8\chi^4} + O\left(\chi^{-6}\right)\,. \tag{2.120}$$

2.E The neutral curve

The neutral curve in the (β_*, μ_*)-parameter plane is defined by the conditions in (2.53). For the dispersion relation in (2.51), these take the form,

$$\mu\beta^2 = 2(1-m^2)Q\left(\chi_0, m\right) \, , \tag{2.121}$$

$$m = \frac{(1-m^2)^2}{\mu\beta^2}\frac{\partial Q\left(\chi_0, m\right)}{\partial m} \, , \tag{2.122}$$

with $\chi_0 = 2\mu/m\beta$ above. (For brevity, in this Appendix, we drop the $*$'s indicating non-dimensional variables.) An examination of the numerical values of χ_0 on the neutral curve motivates the possibility that $\chi_0 \to \infty$ as $\beta \to 0$ and $\chi_0 \to 0$ as $\beta \to \infty$. We now use this numerical observation to derive analytical approximations for the neutral curve in the complementary limiting cases $\beta \to 0$ and $\beta \to \infty$. To this end, we use the approximations to $Q(\chi, m)$ summarized in Appendix D.

2.E.1 Approximation of the marginal curve, $\beta \gg 1$ and $\chi_0 \ll 1$

First in the case of $\beta \to \infty$, we have from (2.119)

$$Q(\chi_0, m) = 1 - \frac{\mu}{\beta}\left(\frac{3}{m} + \frac{5m}{8}\right) + O(m^2\chi_0) \, . \tag{2.123}$$

Clearly, neglecting the $O(m\chi_0)$ term must be justified *post-facto* once a consistent dominant balance is found. Substituting (2.123) in the neutral curve equations, (2.121) and (2.122) and keeping in mind that that $\beta^{-1} \ll 1$, we get

$$\frac{\mu\beta^2}{2} = (1-m^2) - \frac{3\mu}{m\beta} + \frac{29\mu m}{8\beta} + O\left(\mu m^2\beta^{-1}\right) \, , \tag{2.124}$$

$$m^3 = 3\beta^{-3} + O\left(m^2\beta^{-3}\right) \, . \tag{2.125}$$

The only consistent balance in the m-equation corresponds to $m^3 \sim 3\beta^{-3}$ and consequently,

$$m = \frac{3^{1/3}}{\beta} + O(\beta^{-3}) \, . \tag{2.126}$$

Since $m \sim O(\beta^{-1})$ the only consistent balance in (2.121) is $\mu \sim 2\beta^{-2}$. A higher order estimate for μ can be derived by substituting for m to get

$$\mu = \frac{2}{\beta^2}\left(1 - \frac{3^{5/3}}{\beta^2}\right) + O(\beta^{-6})\,. \tag{2.127}$$

These approximate expressions are superimposed on the numerically obtained neutral curve in the Fig. 2.5 with agreement once $\beta > 2$.

2.E.2 Approximation of the marginal curve, $\beta \ll 1$ and $\chi_0 \gg 1$

A similar analysis is used when $\beta \to 0$ for which, we can write from (2.118),

$$\begin{aligned} Q(\chi_0, m) = {} & \frac{3}{2^7}\left(\frac{\beta}{\mu}\right)^4 \left(\frac{m^4}{1-m^2}\right) \\ & + \frac{5}{2^{11}}\left(\frac{\beta}{\mu}\right)^6 \left[\frac{m^6(m^4+2m^2-4)}{(1-m^2)^3}\right] + O(\chi_0^{-8})\,, \end{aligned} \tag{2.128}$$

$$\tag{2.129}$$

and therefore

$$\begin{aligned} \partial_m Q(\chi_0, m) = {} & \frac{3}{2^6}\left(\frac{\beta}{\mu}\right)^4 \left[\frac{m^3(2-m^2)}{(1-m^2)^2}\right] - \\ & \frac{5}{2^{11}}\left(\frac{\beta}{\mu}\right)^6 \left[\frac{m^5(4m^6-6m^4-16m^2+24)}{(1-m^2)^4}\right] + O(\chi_0^{-9})\,. \end{aligned} \tag{2.130}$$

Substituting into equations (2.121) and (2.122) one has

$$\begin{aligned} \mu\beta^2 = {} & \frac{3}{2^6}\left(\frac{\beta}{\mu}\right)^4 m^4 + \\ & \frac{5}{2^{10}}\left(\frac{\beta}{\mu}\right)^6 \left[\frac{m^7(m^4+2m^2-4)}{(1-m^2)^2}\right] + h.o.t.\,, \end{aligned} \tag{2.131}$$

$$\begin{aligned} m = {} & \frac{3}{2^6}\frac{\beta^2}{\mu^5} m^2(2-m^2) - \\ & \frac{5}{2^{11}}\frac{\beta^4}{\mu^7}\left[\frac{m^5(4m^6-6m^4-16m^2+24)}{(1-m^2)^2}\right] + h.o.t. \end{aligned} \tag{2.132}$$

Above, *h.o.t.* refers to the higher order terms that have been neglected from the above equation and can be justified to be small *post-facto*. In (2.131), assuming a dominant balance between the term on the left and the first term on the right, we have

$$\mu \sim \left(\frac{3}{64}\right)^{1/5} \beta^{2/5} m^{4/5} \,. \tag{2.133}$$

Similarly from (2.132)

$$m \sim \frac{3}{2^6}\frac{\beta^2}{\mu^5} m^3 (2 - m^2) \,, \tag{2.134}$$

which on substituting for μ from (2.133), gives us $m \sim 1$ and

$$\mu \sim \left(\frac{3}{64}\right)^{1/5} \beta^{2/5} \,. \tag{2.135}$$

Proceeding to the next order, we obtain after some algebra

$$m \approx 1 - \underbrace{\frac{5^{1/3}}{3^{7/15} 2^{19/15}}}_{\approx 0.43} \beta^{2/5} \,. \tag{2.136}$$

As in the case before, we plot this estimate for m against the numerical estimate in Figure 2.5 and the agreement is excellent. In fact the approximations to $m^{\mathrm{c}}(\beta)$ practically span the entire range of the neutral curve.

2.E.3 The small-m expansion

When $m \to 0$ with all other parameters fixed, we observe in Figure 2.4 that $s \to -\mu$ and therefore in (2.51) the first argument of Q is

$$\frac{s + 2\mu}{m\beta} \approx \frac{\mu}{m\beta} \gg 1 \,. \tag{2.137}$$

To compute the small-m expansion of the dispersion relation we write $s = -\mu + s_1$ and use (2.120) to approximate Q. Thus the dispersion relation (2.51) becomes

$$\beta^2 s_1 \approx \frac{3}{8}\frac{m^4 \beta^4}{\mu^4} \,. \tag{2.138}$$

This produces the small-m version of the dispersion relation in (2.59).

Chapter 2, in full, is a reproduction of the material as it appears in *Srinivasan and Young* [2012], *J. Atmos. Sci,*, **69**, 1633. The dissertation author was the primary investigator and author of this work. W.R Young supervised and directed this research.

3 Meridionally drifting zonal jets on the β-plane

3.1 Introduction

Coherent eddy-driven jets are a prominent feature of the large-scale circulation of terrestrial [*Hartmann*, 2007] and planetary atmospheres [*Porco et al.*, 2003; *Vasavada and Showman*, 2005], and the Southern Ocean [*Sokolov and Rintoul*, 2007; *Thompson and Richards*, 2011]. While the jets in Jupiter have been observed to be remarkably stable over the past three decades [*Porco et al.*, 2003], southern ocean jets display a high degree of spatial and temporal variability [*Sokolov and Rintoul*, 2007], characterized by eddy variability, drift and steering attributed to the presence of background topography [*Thompson*, 2010; *Thompson and Richards*, 2011]. In this paper we study one aspect of the variability of eddy-driven zonal jets, namely the possibility that they slowly drift (or migrate) on a forced-dissipative barotropic β-plane.

Drifting jets have been found previously, in idealized primitive-equation models of the ocean and atmosphere. *Williams* [2003] characterized multiple drifting zonal jets in a weather-layer general circulation model of a Jupiter-like planet. *Chan et al.* [2007] observed migrating jets in a primitive variables, semi-hemispheric zonally reentrant channel model of the ocean. *Chan et al.* showed that the jet drift was a consequence of the meridional residual flow that caused an asymmetry in the baroclinicity on the flanks of each jet. *Thompson and Richards* [2011] describe topographically mediated jet drift in the southern ocean using a high-resolution ocean model and find that the jets migrate from regions of high background potential gradient towards regions of lower PV gradient. In a bid to further isolate the interactions between the jets and topography, *Boland et al.* [2012] used a two-layer quasigeostrophic system on the β-plane in a background topography that has a constant gradient in both the zonal and meridional directions. The jets in the model of *Boland et al.* [2012] were found to be aligned with the background barotropic PV gradient (which was non-zonal due to topography), and also exhibited a prominent drift in the meridional direction.

We simplify the problem further by studying turbulent jets on a barotropic β-plane, driven by a model for exogenous stochastic forcing and dissipated by bottom drag. The equation governing the evolution of the two-dimensional vorticity field, $\zeta(x, y, t)$, is

$$\zeta_t + u\zeta_x + v\zeta_y + \beta v = \xi - \mu\zeta + \nu_8 \nabla^8 \zeta\,, \tag{3.1}$$

where the random forcing, $\xi(x, y, t)$ is spatially homogenous and rapidly decorrelating, β is the background potential vorticity gradient, μ the coefficient of bottom friction while the hyperviscosity ν_8 is required for numerical stability. Previous studies of stochastically driven turbulent jets have often used a spatially isotropic forcing [*Rhines*, 1975; *Vallis and Maltrud*, 1993; *Huang and Robinson*, 1998; *Danilov and Gurarie*, 2004; *Smith*, 2004; *Galperin et al.*, 2006; *Scott and Polvani*, 2007; *Srinivasan and Young*, 2012; *Parker and Krommes*, 2013]. The few studies that have chosen an anisotropic driving force, [*Farrell and Ioannou*, 2003, 2007; *Bakas and Ioannou*, 2013; *Tobias and Marston*, 2013; *Constantinou et al.*, 2012], inadvertently impose an additional symmetry on the statistics of the forcing, that we identify as *mirror* (or reflexional) symmetry. Specifically, mirror symmetry refers to the invariance of the unforced barotropic equation ((3.1), but with $\xi \equiv 0$) under the transformation,

$$y \to -y\,, \quad \psi \to -\psi\,, \tag{3.2}$$

$$x \to x\,, \quad t \to t\,. \tag{3.3}$$

Thus, the only mechanism for breaking mirror symmetry in (3.1) is through the forcing, ξ. In this Chapter, we show that a forcing that preserves mirror symmetry does *not* lead to drifting jets and that breaking mirror symmetry is required for meridional jet drift to occur in the barotropic model, (3.1). It is also precisely why this phenomenon has not been observed in any of the aforementioned studies involving the barotropic model.

In section 3.2, we detail the idea of mirror symmetry and specify our choice of model forcing used for numerical runs in this chapter. In section 3.3, we present numerical solutions of the barotropic vorticity equation and characterize the variation of jet drift as a function of the forcing structure, β and μ. Further, we introduce the quasilinear model, obtained from the barotropic vorticity equation through a eddy-zonal-mean decomposition and subsequent neglect of eddy-eddy interactions in the eddy vorticity equation. Detailed comparisons between jets obtained from the quasilinear and nonlinear barotropic equations have been performed by *Srinivasan and Young* [2012] for isotropic forcing and more recently by *Constantinou et al.* [2012] using anisotropic mirror-symmetric forcing. Here we show that similar comparisons hold for the case of drifting zonal jets that are formed when mirror-symmetry of the forcing is broken.

The second order cumulant equation, the statistical equivalent of the stochastically forced quasilinear equations [*Farrell and Ioannou*, 2003, 2007] is used in section 3.4 but in the continuous-space formalism of *Srinivasan and Young* [2012] that has also been used in *Marston et al.* [2008], *Bakas and Ioannou* [2013] and *Parker and Krommes* [2013]. Employing the perturbative approach of *Bakas and Ioannou* [2013], a theory for jet drift is constructed by assuming a scale-separation between the mean flow and eddies. The details of the theory are relegated to the appendices.

3.2 Statistical properties of the forcing

The forcing function is completely described by its two-point two-time correlation function and we assume that it is homogenous in space and white noise in time,

$$\overline{\xi(\boldsymbol{x}_1, t_1)\xi(\boldsymbol{x}_2, t_2)} = \delta(t_2 - t_1)\,\Xi(x_1 - x_2, y_1 - y_2)\,. \tag{3.4}$$

3.2.1 Exchange symmetry

The forcing statistics in (3.4) must remain unchanged if the points $\boldsymbol{x}_1$ and $\boldsymbol{x}_2$ are interchanged. Using $x = x_1 - x_2$ and $y = y_1 - y_2$, this 'exchange' symmetry is expressed as

$$\Xi(x, y) = \Xi(-x, -y)\,. \tag{3.5}$$

As a consequence of exchange symmetry, a rotation of the (x, y) axis by π leaves $\Xi(x, y)$ unchanged. This ensures that the spectrum

$$\tilde{\Xi}(p, q) \overset{\text{def}}{=} \iint \mathrm{e}^{-\mathrm{i}px-\mathrm{i}qy}\, \Xi(x, y)\, \mathrm{d}x\mathrm{d}y\,, \tag{3.6}$$

is real and non-negative.

3.2.2 Mirror symmetry

The transformations in (3.3) take an even simpler form for the random forcing specified in (3.4). We are concerned with two point correlations of the streamfunction, $\overline{\psi(\boldsymbol{x}_1, t_1)\psi(\boldsymbol{x}_2, t_2)}$, on which a sign change in ψ (i.e. the transformation $\psi \to -\psi$) has no effect and all that remains is the transformation $y \to -y$. Thus the forcing specified by (3.7) is mirror symmetric if its statistics are invariant under reflection about the x-axis,

$$\Xi(x, y) = \Xi(x, -y)\,. \tag{3.7}$$

In conjunction with the exchange symmetry, (3.5), (3.7) also implies an invariance of $\Xi(x, y)$ to a reflection about the y-axis. In terms of the spectrum, $\tilde{\Xi}(p, q)$, mirror symmetry takes a similar form as (3.7),

$$\tilde{\Xi}(p, q) = \tilde{\Xi}(p, -q)\,. \tag{3.8}$$

In polar coordinates, $(p, q) = k(\cos\phi, \sin\phi)$, the 2π-periodicity of the angle, ϕ allows a general spectrum $\tilde{\Xi}(k, \phi)$ (that does not necessarily satisfy (3.8)) to be expressed as a Fourier series,

$$\tilde{\Xi}(k, \phi) = \underbrace{\sum_{m=0}^{\infty} A_m(k) \cos 2m\phi}_{\tilde{\Xi}_c} + \underbrace{\sum_{m=1}^{\infty} B_m(k) \sin 2m\phi}_{\tilde{\Xi}_s}\,, \tag{3.9}$$

where the functions, $\tilde{\Xi}_c$ and $\tilde{\Xi}_s$ satisfy

$$\tilde{\Xi}_c(k,\phi) = \tilde{\Xi}_c(k,-\phi)\,, \tag{3.10}$$

$$\tilde{\Xi}_s(k,\phi) = -\tilde{\Xi}_s(k,-\phi)\,. \tag{3.11}$$

Because (3.10) is just another way of expressing the mirror-symmetry relation, (3.8), it follows that any arbitrary forcing spectrum can be written as the linear sum of a mirror symmetric component ($\tilde{\Xi}_c$) and one that explicitly breaks this symmetry ($\tilde{\Xi}_s$).

3.2.3 The anisotropic ring forcing

For this paper, we choose a simplified forcing that is concentrated on a circle with radius k_f in wavenumber space. The anisotropy is characterized by the lowest modes ($m = 0, 1$) of the Fourier series in (3.9) and contains both mirror-symmetric and anti-symmetric components. The spectrum of this model forcing is written as

$$\tilde{\Xi}(p,q) = 4\pi k_f \varepsilon \left(1 + \alpha_c \cos 2\phi + \alpha_s \sin 2\phi\right) \delta(k - k_f)\,, \tag{3.12}$$

where ε is a measure of the strength of the forcing, while α_c and α_s are parameters that must satisfy the condition,

$$\alpha_c^2 + \alpha_s^2 \leq 1 \tag{3.13}$$

to ensure that the spectrum is non-negative. The corresponding correlation function in polar coordinates, $(x,y) = r(\cos\theta, \sin\theta)$ is,

$$\Xi(x,y) = 2\varepsilon k_f^2 \left[J_0(k_f r) - J_2(k_f r)\left(\alpha_c \cos 2\theta + \alpha_s \sin 2\theta\right)\right]\,, \tag{3.14}$$

where $J_m(z)$ is the Bessel function of order m.

Figure 3.1 shows model correlation functions and forcing obtained by varying α_c and α_s in (3.14). When $\alpha_s = 0$ and $\alpha_c = 1$ (Figure 3.1(a), (b)), the forcing has a spatial structure that closely resembles the 'noodle'-modes obtained from baroclinic instability of flow with zonally oriented vertical shear [*Berloff et al.*, 2009]. The tilted-noodle structures seen in Figure 3.1(f) can be obtained through baroclinic instability of a background flow with a non-zonal vertical shear [*Smith*,

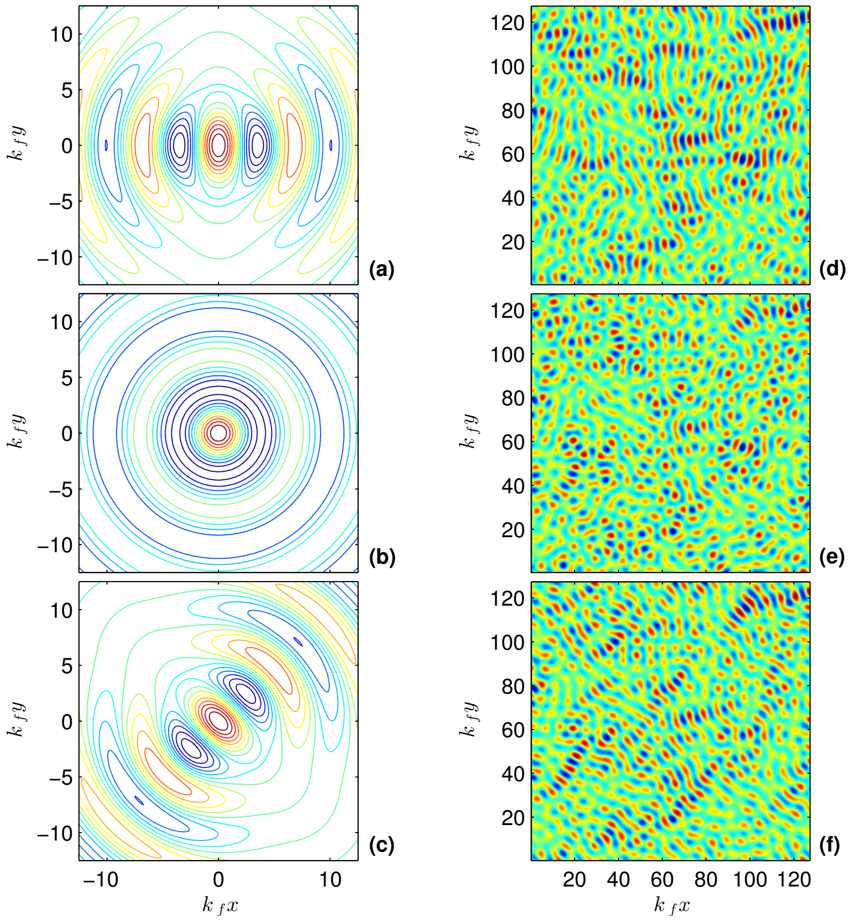

Figure 3.1: The left panels show the anisotropic ring correlation function Ξ in (3.14) and the right panels show corresponding snapshots of the forcing ξ. Panels (a) and (d) show $\alpha_c = 1$, $\alpha_s = 0$; (b) and (e) show the isotropic case $\alpha_c = \alpha_s = 0$; panels (c) and (f) show $\alpha_c = 0$ and $\alpha_s = 1$.

2007] or if the background topography has a zonally varying component [*Chen and Kamenkovich*, 2013]. The isotropic forcing corresponding to $\alpha_c = \alpha_s = 0$ is also shown for reference in Figure 3.1(b) and (d).

3.3 Numerical solutions of the barotropic vorticity equation

In this section we present numerical solutions of (3.1) by varying the forcing parameters (α_c, α_s) and the flow parameters μ and β. Following *Srinivasan and Young* [2012], we solve (3.1) on a doubly-periodic domain of size, $2\pi L \times 2\pi L$ and we pick $k_f L = 32$ to ensure scale separation. The ETDRK4 scheme [*Cox and Matthews*, 2005] is used for time-stepping at a spatial resolution of 512×512 for all the results in this section. The flow parameters (μ, β) are non-dimensionalized using a time-scale $(\varepsilon k_f^2)^{-1/3}$ and length-scale k_f^{-1},

$$\mu_* \overset{\text{def}}{=} \frac{\mu}{k_f^{2/3}\varepsilon^{1/3}}\,, \qquad\qquad \beta_* \overset{\text{def}}{=} \frac{\beta}{k_f^{5/3}\varepsilon^{1/3}}\,. \tag{3.15}$$

The forcing spectrum is modified from the theoretical ‘ring’-forcing form in (3.12) to a ‘band’-forcing form where the radial δ-function is replaced by a narrow band of wavenumbers centered around k_f and having a thickness $\delta k = k_f/8$. The details of the numerical implementation of the forcing have been discussed at length in *Srinivasan and Young* [2012] and are not repeated here.

3.3.1 Forcing with broken mirror-symmetry: Drifting jets

As a starting point, we pick the flow parameters, $\beta_* = 1$ and $\mu_* = 0.0364$ and study the effect of varying α_c and α_s on the time evolution of the zonal-averaged velocity, $U(y,t) = \bar{u}(x,y,t)$, where the overbar denotes a zonal-average. We first consider a forcing that breaks mirror-symmetry by setting $\alpha_c = 0$ and for three values of α_s: -1, 0 and 1 (if $\alpha_c = 0$, then $|\alpha_s| \le 1$ from (3.13)). Note that α_c does not need to be zero but is chosen so for simplicity. Figure 3.2 shows the Hovmöller plots of the zonal-mean velocity and we observe that the jets drift southward or northward depending on whether α_s takes the value 1 or -1. Isotropically forced jets are plotted in Figure 3.2 (b) as a reference. The drift is characterized as being ‘slow’ because it happens over many decades of the drag time scale $\tau = (2\mu)^{-1}$. Other than the presence of jet drift, the three cases shown in Figure 3.2 are remarkably similar in terms of the number of jets (which varies between 9 and 10 jets) and also the strength of the jets. The jet strength can be quantified using the zonal mean fraction (zmf), defined as the ratio of the kinetic energy of the zonal-mean flow to the total flow kinetic energy,

$$\text{zmf} \overset{\text{def}}{=} \left\langle \frac{\int U^2 \, \mathrm{d}a}{\int U^2 + u'^2 + v'^2 \, \mathrm{d}a} \right\rangle_t , \tag{3.16}$$

where $\int \cdots \mathrm{d}a$ is the area integral over the domain of the flow while the operator $\langle \ \rangle_t$ denotes a time average that is performed after the flow attains equilibrium. The zmf values for the the three cases in Figure 3.2 are 0.15 ($\alpha_s = 1$), 0.12 ($\alpha_s = 0$) and 0.145 ($\alpha_s = -1$). Owing to the symmetry in the jet strength, structure and spacing in the $\alpha_s = 1$ and $\alpha_s = -1$ cases, for the remainder of this section we only present results for the $\alpha_s = 1$ forcing.

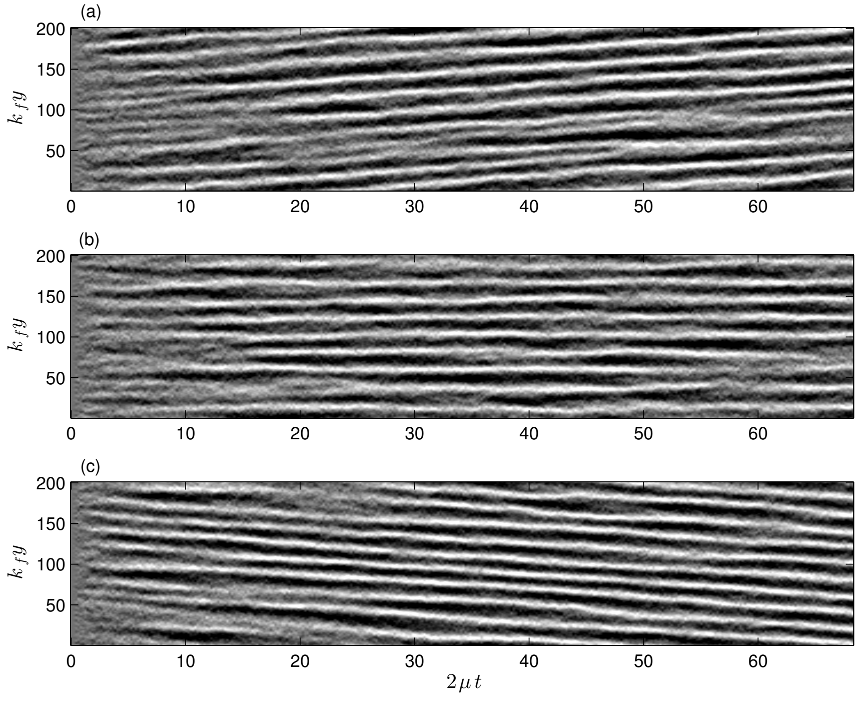

Figure 3.2: Turbulent drifting jets: Hovmöller diagrams of the zonal-mean velocity when the forcing breaks mirror symmetry. Here $\alpha_c = 0$ and (a) $\alpha_s = -1$, (b) $\alpha_s = 0$ (isotropic forcing) and (c) $\alpha_s = 1$. The flow parameters are $\mu_* = 0.036$ and $\beta_* = 1$.

3.3.2 The effect of varying μ_* and β_*

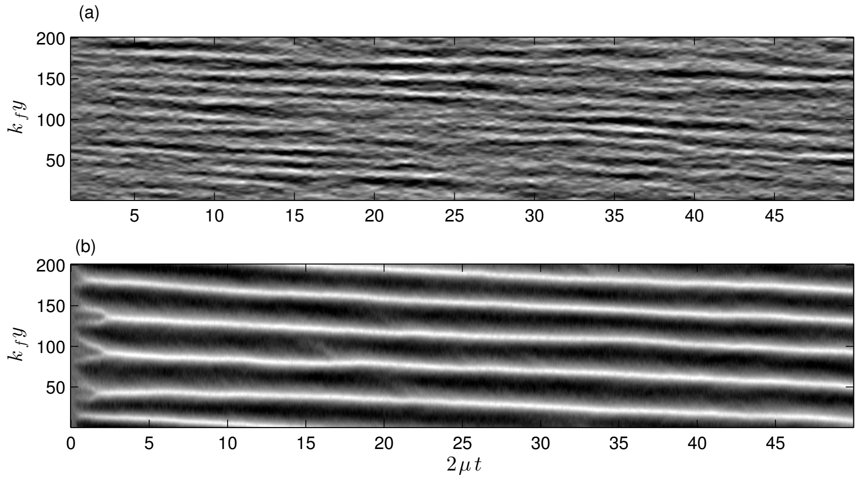

Figure 3.3: Hovmöller diagrams of the zonal-mean velocity when the forcing breaks mirror symmetry as the drag parameter is varied. Here $\alpha_c = 0$ and $\alpha_s = 1$. $\beta_* = 1$ is fixed while the drag values are (a) $\mu_* = 0.055$ and (b) $\mu_* = 0.0046$.

We now attempt to characterize the variation of the jet drift for the $\alpha_s = 1$, $\alpha_c = 0$ forcing as a function of the flow parameters μ_* and β_*. All the numerical results involving jet drift lie in the range $0.3 \leq \beta_* \leq 5$ and $0.0046 \leq \mu_* \leq 0.055$, about a decade of variation in each parameter. Figure 3.3 compares the Hovmöller plots for $\beta_* = 1$ and the two extreme values of μ_* for which numerical results are available: the strong drag flow consisting of weak 'streaky' jets encountered in Chapter 2 (zmf=0.04) while the weak drag flow has strong persistent jets (zmf=0.45). Through visual inspection of Figure 3.3, we notice that the drift in the two cases is almost the same. However since the axis in each case is written in terms of the inverse drag time-scale $(2\mu)^{-1}$, this admits the inference, $v_d \propto \mu_*$. For $\beta_* = 1$, and using drift values from runs over the entire range of available μ_*, we get a best-fit numerical estimate :

$$v_d(\mu_*, \beta_* = 1) \approx 1.6 \mu_* \varepsilon^{2/3} k_f^{-2/3} \, . \tag{3.17}$$

To see how well this estimate works, we compute drift from the Hovmöller diagrams using a Radon transform [*Maximenko et al.*, 2008] and as can be seen from Figure

3.5 (b), (3.17) provides a reasonable estimate for the drift speed when $\alpha_c = 0$, $\alpha_s = 1$ and $\beta_* = 1$. The proportional decrease of the drift speed with drag is not unexpected: as the μ_* decreases the jets get stronger and wider (as seen in Figure 3.3) while the forcing strength (characterized by ε) is constant. Thus stronger and more scale separated jets would be expected to interact with the forcing to a lesser degree, thereby reducing drift.

The dependence of drift on β_* can be seen in Figure 3.4 which contains results for $\mu_* = 0.0182$ and β_* about a factor of 16 apart. A surprising result that is noted here is that the drift increases for decreasing β_*. In fact, based on the results shown in Figure 3.5 the numerics indicate a $v_d \propto \beta_*^{-7/10}$ scaling for the parameter range for which results are available. In conjunction with the empirical scaling suggested in (3.17), we get

$$v_d(\mu_*, \beta_*) \approx 1.6\mu_* \beta_*^{-7/10} \varepsilon^{2/3} k_f^{-2/3} \,. \tag{3.18}$$

A wider range of numerical results are needed in the $\beta_* \to 0$ limit to have any degree of confidence in the scaling, (3.18), though the important point here that the jet speed increases with decreasing β_* faster than $\beta^{-1/2}$ but slower than β^{-1} . While this apparent divergence in the jet drift with β_* is surprising, it should be noted that for fixed μ_* and as $\beta_* \to 0$, the jets become wider (as $\beta_*^{-1/2}$ based on the Rhines scale form in Chapter 2 (2.83)) and also weaker, there being no jets when $\beta_* = 0$. As the jets get weaker they have a greater tendency to meander even for isotropic or mirror-symmetric forcing.

An important point regarding the drifting jets is that they are all *zonal*, as seen from a snapshot of vorticity field plotted in Figure 3.6 (a). In the study by *Boland et al.* [2012] however, the drifting jets are always non-zonal, i.e. non-zonality of the jets (also referred to as topographic steering) is intrinsically coupled to jet drift. In the two-layer quasigeostrophic model used by Boland et al, the layer-wise potential vorticity is slanted at an angle to the barotropic PV gradient, along which the jets propagate (which is again, non-zonal due to topopgraphy). *Boland et al.* conjecture that this cross-gradient advection of layerwise PV by the jets causes jet drift.

There is some similarity of *Boland et al.* [2012] with the present study

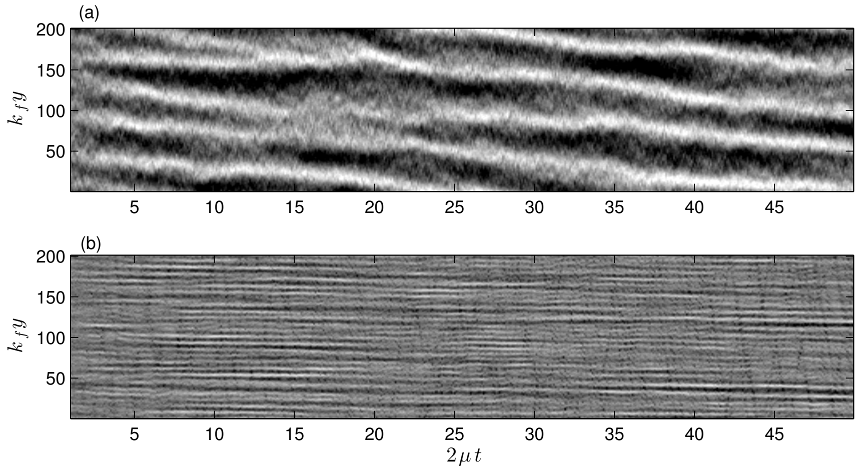

Figure 3.4: Hovmöller diagrams of the zonal-mean velocity when the forcing breaks mirror symmetry as the drag parameter is varied. Here $\alpha_c = 0$ and $\alpha_s = 1$. $\mu_* = 0.0182$ is fixed while the β_* values are (a) $\beta_* = 0.3$ and (b) $\beta_* = 5$.

because jet drift is only found when the phase lines of the forcing are inclined at an angle to that of the barotropic potential vorticity gradient, which in this case is just β.

3.3.3 Mirror-symmetric forcing

We take a brief look at anisotropic mirror-symmetric forcing ($\alpha_s = 0$) for three choices of α_c: -1, 0 and 1 (for $\alpha_s = 0$, $|\alpha_c| \leq 1$ from (3.13)). Figure 3.7 shows the Hovmöller plots of the zonal-mean velocity and we notice that even though the jets get stronger and more pronounced as α_c increases from -1 to 1, no drift of jets is observed. For the results shown in Figure 3.7 the jet strength increases from zmf=0.06 when $\alpha_c = -1$ to zmf=0.22 when $\alpha_c = 1$, a factor of about 4. Keeping β_* fixed at $\beta_* = 1$, when the drag is reduced by a factor of 20 to $\mu_* = 0.00182$ (jets not shown), the zmf values for the $\alpha_c = -1$ case and $\alpha_c = -1$ case are 0.49 and 0.51 respectively. Thus at large values of μ_*, the $\alpha_c = 1$ forced jets are much stronger than the $\alpha_c = -1$ jets, but this effect disappears as μ_* becomes sufficiently small. This phenomenon remains true for other values of β_*. A possible explanation for the effect of the cosine-forcing is provided based

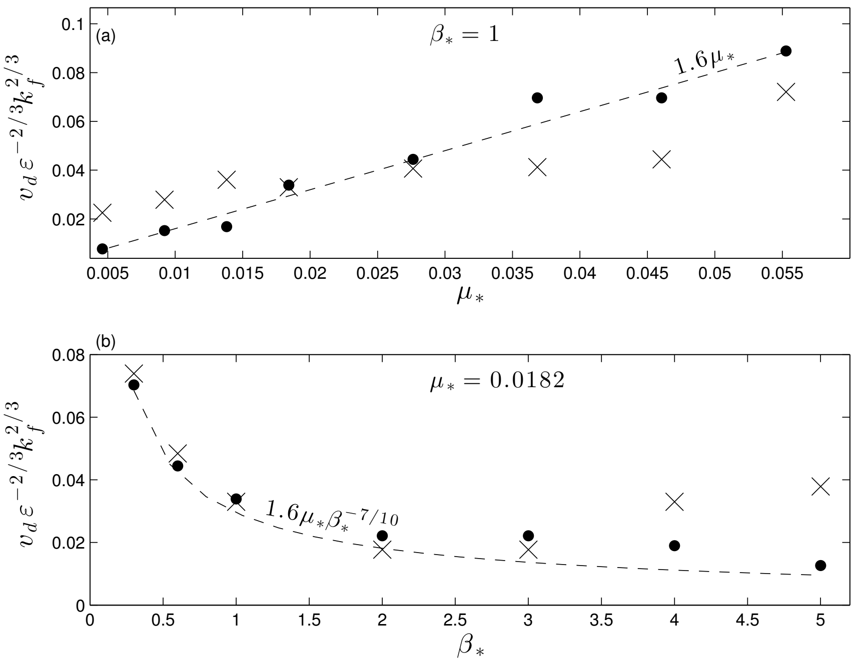

Figure 3.5: (a) Non-dimensional jet-drift at fixed $\beta_* = 1$, as a function of μ_* for the non-linear (filled-circles) and quasi-linear runs (crosses). The dashed line represents the $1.6\mu_*$ curve and is a best-fit estimate of the non-linear drift variation. (b) Jet drift at fixed $\mu_* = 0.0182$ as a function of β_* for the non-linear (filled-circles) and quasi-linear runs (crosses). The dashed line is the $1.6\mu_*\beta_*^{-7/10}$ curve (with $\mu_* = 0.0182$).

on the theoretical results derived in section 3.4.1. The effect of anisotropic mirror symmetric forcing is not a particular focus of this study, except to establish that no drift of the jets is observed, a finding that is consistent with previous studies [*Constantinou et al.*, 2012; *Bakas and Ioannou*, 2013].

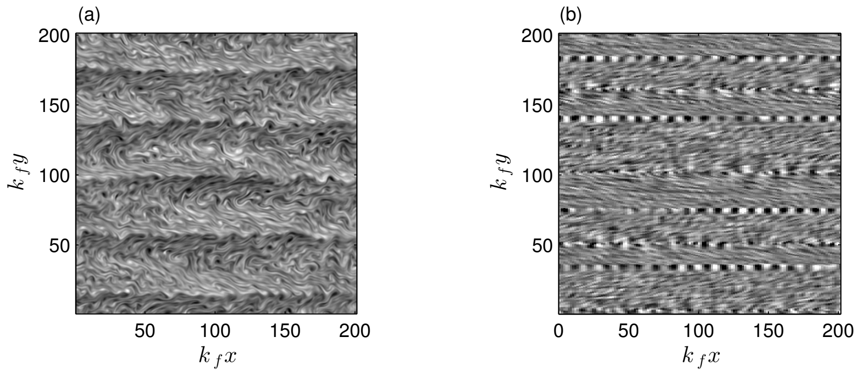

Figure 3.6: (a) Snapshot of the vorticity $\zeta(x, y)$, obtained from the nonlinear barotropic model at $2\mu t = 50$ for $\alpha_c = 0$, $\alpha_s = 1$, $\beta_* = 1$, $\mu_* = 0.0046$ corresponding to the run shown in Figure 3.3 (b). (b) The same but obtained from the quasi-linear model.

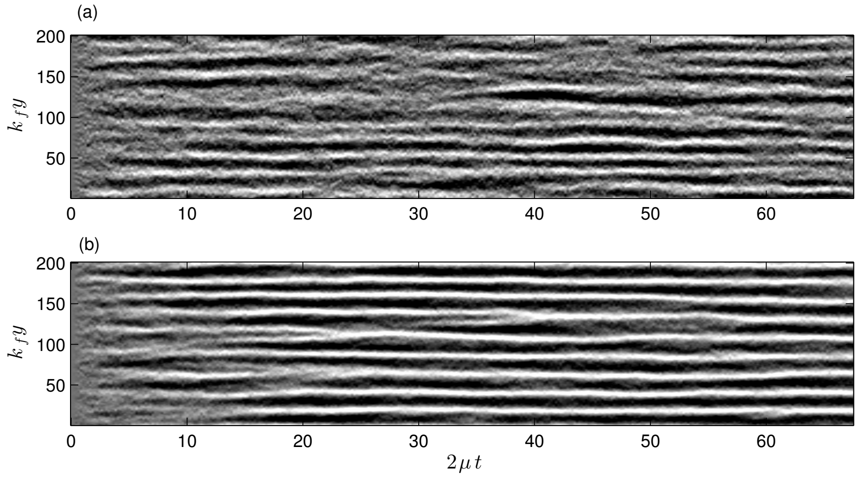

Figure 3.7: Hovmöller diagrams of the zonal-mean velocity subject to a mirror symmetric forcing ($\alpha_s = 0$) and two extremal values of α_c, (a) $\alpha_c = -1$, (b) $\alpha_c = 1$. The flow parameters are $\mu_* = 0.036$ and $\beta_* = 1$.

3.4 Quasi-linear dynamics and a CE2-based theory

Following the methodology of Chapter 2, we solve the quasi-linear equations for the zonal-mean flow, $U(y, t)$ and eddy vorticity field $\zeta'(x, y, t)$:

$$\partial_t U + \partial_y \left(\overline{u'v'}\right) = -\mu U + \nu \partial_y^{2n} U\,, \tag{3.19}$$

$$\zeta'_t + U\zeta'_x + (\beta - U_{yy})\psi'_x = \xi - \mu\zeta' + \nu\nabla^{2n}\zeta'\,. \tag{3.20}$$

where the spectrum of $\xi(x, y, t)$ is given by the sine-forcing ($\alpha_c = 0, \alpha_s = 1$) discussed in the previous section. We first show that jet drift is indeed found to occur in the QL system and the magnitude of jet drift is similar to that observed in the non-linear system. Then we construct a theory based on the second-order cumulant expansion equations (CE2) derived in Chapter 2, (2.31) to explain some of the features of jet drift observed in this chapter.

Figure 3.8 shows the Hovmöller plots of the mean-flow obtained from quasi-linear runs with forcing and (μ_*, β_*) values identical to the results shown in Figure 3.2. Consistent with the results found in Chapter 2, the QL jets are stronger than their NL counterparts. However comparing Figures 3.2 and 3.8, we see that the jet spacing (or number of jets), jet drift and asymmetry in the drift between $\alpha_s = 1$ and $\alpha_s = -1$ are almost identical. A more detailed comparison can be seen from the drift speed variation with the parameters, μ_* and β_* in Figure 3.5 (a) and (b). First, we note that, like the nonlinear jets, v_d in the QL jets decreases with μ_* but the nearly linear decrease with μ_* is no longer observed. Further, the decrease of jet drift in the $\mu_* \to 0$ limit is actually slower for the QL jets when compared to v_d of the NL jets. One possible reason for this is that, as μ_* decreases, the turbulent inverse cascade mechanism transfers energy to the mirror symmetric components thereby reducing the effectiveness of the drift generating components (that break mirror symmetry). For fixed μ_* and varying β_*, (Figure 3.5 (b)), the QL and NL drift values track each other surprisingly well, especially in the limit $\beta_* \to 0$. However for larger values of β_*, the NL drift values decrease almost monotonically whereas the QL drift values *increase*. The reasons for the variation of v_d with β_* remain unclear at this juncture, an issue that is not addressed by the theory presented in the next section.

3.4.1 CE2 theory for a slowly varying mean flow

In this section we attempt to construct a theory for the observed jet drift when a mirror symmetry breaking forcing is used. Our starting point is the second-order cumulant equation, the statistical equivalent of the quasi-linear eddy equation, (3.20), under some ergoticity assumptions. This correlation equation has

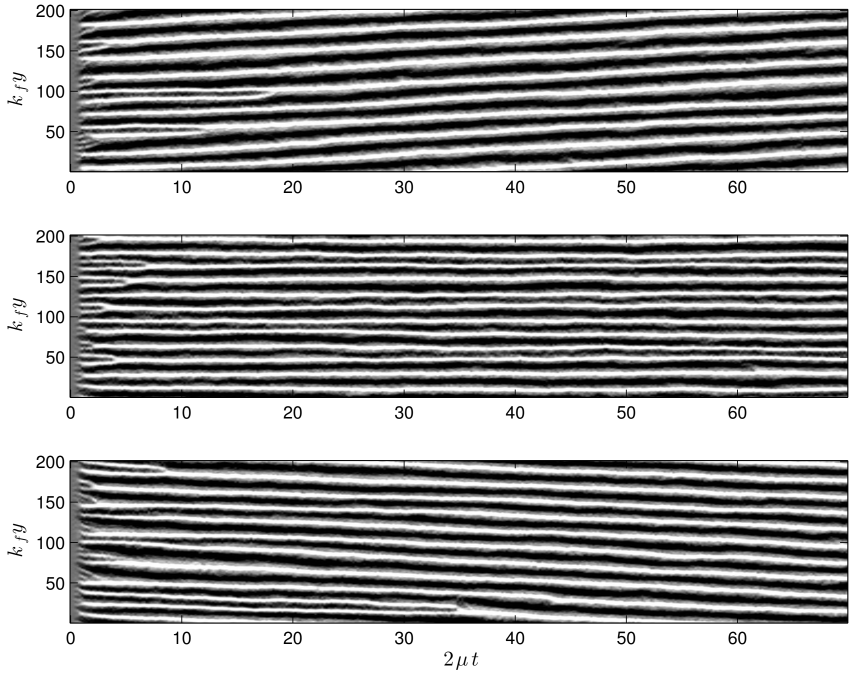

Figure 3.8: Quasi-linear drifting jets: Hovmöller diagrams of the quasi-linear zonal-mean velocity when the forcing breaks mirror symmetry. Here $\alpha_c = 0$ and (a) $\alpha_s = -1$, (b) $\alpha_s = 0$ (isotropic forcing) and (c) $\alpha_s = 1$. The flow parameters are $\mu_* = 0.036$ and $\beta_* = 1$.

been derived in considerable detail in Chapter 2 (2.31) and is,

$$\begin{aligned}\partial_t \mathcal{Z} + (U_1 - U_2)\partial_x \mathcal{Z} - (U_1'' - U_2'')\left(\nabla^2 + \tfrac{1}{4}\partial_{\bar{y}}^2\right)\partial_x \Psi \\ - (2\beta - U_1'' - U_2'')\,\partial_{\bar{y}}\partial_y\partial_x\,\Psi \\ = \Xi - 2\mu\mathcal{Z} + 2\nu\nabla^2\mathcal{Z} + \tfrac{1}{2}\nu\partial_{\bar{y}}^2\mathcal{Z}\,. \qquad (3.21)\end{aligned}$$

Here $\mathcal{Z}(x, y, \bar{y}) = \overline{\zeta'(x_1, y_1, t)\zeta'(x_2, y_2, t)}$ and $\Psi(x, y, \bar{y}) = \overline{\psi'(x_1, y_1, t)\psi'(x_2, y_2, t)}$ are the two-point single time correlation functions of the vorticity and streamfunction respectively, while $x = x_1 - x_2$, $y = y_1 - y_2$ and $\bar{y} = (y_1 + y_2)/2$ are the collective co-ordinates introduced in Chapter 2.

The Reynolds stress obtained from Ψ using,

$$\overline{u'v'}(\bar{y}, t) = \partial_x\partial_y\Psi(x, y, \bar{y}, t)\big|_{x=y=0}\,, \qquad (3.22)$$

is then used to solve the mean-flow evolution equation, (3.19). However, the complexity of the correlation equation, (3.21) leaves any direct solution untenable.

Instead, following *Bakas and Ioannou* [2013], we make the following assumptions that allow us to obtain approximate solutions to (3.21):

1. **The adiabiatic approximation**: The eddies adjust instantaneously to the mean flow so that the time derivative term in (3.21) is neglected. As a result of this assumption, the Reynolds stress, (3.22) is only a function of the mean flow, $U(y,t)$ and all its y-derivatives, and not of time.
2. **Scale-separation between mean-flow and forced modes** : i.e. $U \equiv U(\epsilon y)$, where $\epsilon = k_f L_J^{-1} \ll 1$, where L_J is the jet scale. In other words, the forcing varies slowly over the scale of the forced modes.
3. **Near laminar flow**: We assume that the parameters (μ_*, β_*) are chosen so that the jets are are just beginning to emerge and are close to the zonostrophic stability boundary evaluated in Chapter 2. In other words, the dominant balance in (3.21) is the homogenous solution

$$\mathcal{Z}_{\mathsf{H}} = \frac{\Xi}{2\mu}\,. \tag{3.23}$$

As a consequence of scale separation, the mean flow at the two points y_1 and y_2 can be written as

$$U_{1,2} \equiv U(\epsilon y_{1,2}) = U(Y \pm \epsilon y)\,, \tag{3.24}$$

where the 'slow' variable $Y = \epsilon\bar{y}$ tracks the variation over the jet scale. The structure of the mean flow in (3.24) allows a perturbation expansion in the form,

$$U_{1,2} = U(Y) \pm \epsilon y U_Y + \frac{\epsilon^2 y^2}{2} U_{YY} + O(\epsilon^3)\,. \tag{3.25}$$

We now substitute (3.25) in (3.21) and using the adiabatic approximation (setting $\partial_t \mathcal{Z} = 0$ in (3.21)), arrange the terms in increasing powers of ϵ (see Appendix 3.A for steps involved in the derivation) to obtain a single equation in $\mathcal{Z}$ and Ψ,

$$2\mu Z = \Xi - \epsilon\left(y U_Y \partial_x \mathcal{Z} - 2\beta \partial_Y \partial_y \partial_x \Psi\right) + O(\epsilon^3)\,. \tag{3.26}$$

$\mathcal{Z}$ and Ψ are related to each other through the double Laplacian equation, $\mathcal{Z} = \nabla_1^2 \nabla_2^2 \Psi$, which in terms of the perturbed coordinates (x, y, Y) takes the form,

$$\mathcal{Z} = \nabla^4 \Psi + \frac{\epsilon^2}{2}(\partial_x^2 - \partial_y^2)\partial_{YY}\Psi + O(\epsilon^4)\,, \tag{3.27}$$

a more detailed derivation of (3.27) is in Appendix 3.A. If we substitute for $\mathscr{Z}$ using (3.27) in (3.26), we get a single differential equation for Ψ involving the perturbation parameter ϵ. This equation in Ψ can be solved iteratively after assuming the lowest order balance to be the homogenous laminar flow solution (assumption 3 above),

$$\nabla^4 \Psi_{\mathsf{H}} = \frac{\Xi}{2\mu}\,, \tag{3.28}$$

where Ξ is the homogenous anisotropic forcing defined in (3.12) and (3.14). The iterative solution to (3.26), starting from (3.28) is best accomplished in Fourier space and the interested reader is referred to Appendix 3.A for details. Here we just note that once this solution is obtained, we can find the Reynolds stress using (3.22) in the form,

$$\overline{u'v'} = b_0\,\alpha_s + \epsilon\alpha_c\,b_1 U_Y + \epsilon^2\,\alpha_s\,\left[b_{21}U_{YY} + b_{22}U_Y^2\right] + O(\epsilon^3)\,. \tag{3.29}$$

Here the coefficients b_0, b_1, b_{21} and b_{22} are functions of (μ, β) and turn out to be,

$$b_0 = -\frac{\varepsilon}{4\mu}\,,\,, \qquad b_1 = \frac{\varepsilon}{8\mu^2}\,, \tag{3.30}$$

$$b_{21} = \frac{\beta}{k_f^2}\frac{\varepsilon}{32\mu^3}\,, \qquad b_{22} = \frac{3\varepsilon}{32\mu^3}\,. \tag{3.31}$$

Note that when solving the mean-flow equation, we need to go back to the 'real' coordinate, $\bar{y} = Y/\epsilon$, so

$$\epsilon U_Y = U_{\bar{y}}\,, \quad \epsilon^2 U_{YY} = U_{\bar{y}\bar{y}}\,, \quad \epsilon^2 U_Y^2 = U_{\bar{y}}^2\,, \tag{3.32}$$

and ϵ does not appear explicitly when the Reynolds stress, (3.29) is used in the mean-flow equation, (3.19).

The Reynolds stress expression, (3.29) leads to some important inferences. First if we isolate the U_{YY} term in (3.29) and after using (3.32), substitute it in the mean-flow equation, (3.19), and neglect the friction terms, we get,

$$\frac{\partial U}{\partial t} = -\frac{\varepsilon}{32k_f^2}\frac{\alpha_s\beta}{\mu^3}\frac{\partial^3 U}{\partial y^3}\,. \tag{3.33}$$

(3.33) is a one-dimensional dispersive wave-equation and is in fact the term that accounts for jet drift observed in this chapter. This wave moves in the positive

y-direction when $\alpha_s < 0$, and in the negative y-direction when $\alpha_s > 0$, and there is no propagation when $\alpha_s = 0$ (mirror-symmetric forcing). Thus the basic features of jet-drift, pertaining to the results shown in Figures 3.2 and 3.8 are qualitatively explained by the CE2 theory. We should also mention here that there are no other dispersive terms in the Reynolds stress, at this order in (3.29).

However, the problem with (3.33), is that it predicts the wrong *scaling* for the jet drift compared to the observed scaling in Figure 3.5 and (3.18). This is reminiscent of the theoretical predictions for zonation (jet emergence) in Chapter 2 where the incorrect scaling for jet size is found. The reason here for the incorrect scaling is probably the same as the one speculated in Chapter 2: our perturbation theory is based around the neutral stability curve of the quasi-linear system, which is rather far (in (μ_*, β_*) parameter space) from the parameter values when turbulent jets actually exist in the non-linear equation. To get a realistic estimate for the drift scaling, we speculate that equation (3.26) must be solved directly instead of a perturbative expansion around the homogenous, laminar solution. Another reason for the quantitative failure of the perturbation theory approach is that we have assumed that ϵ is *independent* of the parameters μ_* and β_*, which is hard to justify. For example, if the jet scale (characterized by its wave-number m) is given by the Rhines scale, which in terms of the parameters μ_* and β_* is

$$m_{Rh} = k_f \mu_*^{1/4} \beta_*^{1/2} \, , \tag{3.34}$$

then, $\epsilon = m_{Rh}/k_f$ is clearly *not* independent of μ_* and β_*. To make matters worse, the magnitude of mean-flow velocity is also a strong function of μ_* (and consequently of ϵ) and cannot be treated to be independent either.

A second observation from (3.29), is that when $\alpha_s \neq 0$, the forcing itself has a *non-zero* Reynolds stress in absence of the mean-flow or β. This is evident from the structure of the correlation function in Figure 3.1(c) but is still somewhat surprising. This constant, mean-flow independent Reynolds stress is however not dynamically relevant for the mean flow equation, (3.19), as it is the divergence of Reynolds stress that drives the mean-flow.

Finally, the second term in the right-hand-side of (3.29), recovers the weak-shear result from Chapter 4 (4.41) and justifies the slowly varying flow interpretations put forth in (4.45). As in the case of Chapter 4, the shear (U_Y) term in (3.29) admits a effective viscosity interpretation,

$$\nu_e = -\frac{\varepsilon \alpha_c}{8\mu^2}\,, \tag{3.35}$$

which is obviously identical to (4.41). The effective viscosity, (3.35), offers an possible explanation for why the $\alpha_c = 1$ jets are stronger than the $\alpha_c = -1$ jets in Section 3.3.3: the $\alpha_c = 1$ forcing has a *negative* viscosity to the lowest order and is therefore more efficient at transferring energy to the mean-flow than the $\alpha_c = -1$ forcing which has a net *positive* viscosity at this order (so energy is transferred from the mean-flow to the forced modes).

3.5 Conclusion

In this Chapter, we have demonstrated the phenomenon of meridional jet-drift on a forced-dissipative barotropic β-plane. The occurrence of jet drift is determined by the spatial structure of the stochastic forcing, though its magnitude is controlled by the flow parameters, β and the bottom friction, μ (which is also the dominant dissipation mechanism in this study). Drift occurs whenever the forcing breaks a particular kind of spatial symmetry that we refer to as mirror, or reflexional symmetry. Physically, this means that the phase lines of the forcing are inclined at an angle (not 0° or 90°) to the lines of constant background potential vorticity, i.e. the zonal direction. This interpretation also allows us to explain the occurrence of jet drift in the two-layer quasi-geostrophic model on a β-plane in the presence of zonally varying topography, as found by *Boland et al.* [2012]. The presence of zonally varying topography, results in unstable baroclinic modes that are slanted with respect to the background barotropic gradient [*Chen and Kamenkovich*, 2013] to cause jet drift in a fashion similar to that found in our barotropic simulations. The magnitude of drift speed in our results shows a strong variation with both μ and β: while the drift speed decreases almost linearly with decreasing μ, it actually increases as β decreases.

In conjunction with the numerical results from the barotropic vorticity equation, we also study jet drift in a simpler quasi-linear model. The quasi-linear equation governs the evolution of eddy vorticity, that is only modified due to interactions with the zonal-mean flow and not with other eddies, so that non-linear eddy-eddy interactions are suppressed. Chapter 2 presents detailed comparisons between the isotropically forced jets obtained from quasilinear and non-linear equations, and considerable agreement is found between the jet scales and strength over a wide range of the (μ, β) parameter space. In this study, the quasi-linear equation is forced with the anisotropic mirror-symmetry breaking forcing and as in the case of the nonlinear runs, drifting jets are observed, with the same direction (i.e. northward or southward) and similar magnitude as nonlinear jet-drift.

In light of the agreement between the quasilinear and nonlinear jet drift, we construct a theory based on the second order cumulant equation [*Marston et al.*, 2008; *Srinivasan and Young*, 2012], that is essentially a statistical equivalent of the stochastically forced quasilinear equation. Starting from the laminar solution, and assuming a mean-flow that varies slowly with reference to the scale of the eddies, we obtain an approximate equation for the vorticity correlation function that is then solved perturbatively. The Reynolds stress of the pertubative solution can then be expressed as a function of the mean-flow and its y-derivatives. In particular, it is shown that as long as the forcing breaks mirror-symmetry, the Reynolds stress has a wave-like term, as a result of which the mean-flow is governed by a dispersive wave equation. The drift speed predicted by the wave-equation has the correct direction of drift observed in the numerical simulations but the wrong dependence on the parameters μ and β.

3.A The perturbation expansion

Using (3.25), we have the following expressions:

$$U_1 - U_2 = U_Y \epsilon y + \frac{U_{YYY} \epsilon^3 y^3}{24} + O(\epsilon^5)\,, \tag{3.36}$$

$$U_1 + U_2 = 2U(Y) + \frac{U_{YY} \epsilon^2 y^2}{4} + O(\epsilon^4)\,, \tag{3.37}$$

and

$$U_1'' - U_2'' = U_{YYY}\epsilon^3 y + O(\epsilon^5)\,, \tag{3.38}$$

$$U_1'' + U_2'' = 2U_{YY}\epsilon^2 + O(\epsilon^4)\,, \tag{3.39}$$

The left hand side of the correlation equation (3.21), accurate to $O(\epsilon^5)$ expands to,

$$\left(U_Y\epsilon y + \frac{U_{YYY}\epsilon^3 y^3}{24}\right)\partial_x\mathscr{Z} - U_{YYY}\epsilon^3 y\nabla^2\partial_x\Psi - \epsilon\left(2\beta - 2U_{YY}\epsilon^2\right)\partial_Y\partial_y\partial_x\Psi. \tag{3.40}$$

We then substitute (3.40) in (3.21) and arrange the terms in increasing powers of ϵ to get (3.26). Remember that $\mathscr{Z}$ and Ψ are related by

$$\mathscr{Z} = \nabla_1^2\nabla_2^2\Psi\,, \tag{3.41}$$

which in collective coordinates is (from Chapter 2),

$$\mathscr{Z} = \nabla^4\Psi + \tfrac{1}{2}\left(\partial_x^2 - \partial_y^2\right)\partial_{\bar{y}}^2\Psi + \tfrac{1}{16}\partial_{\bar{y}}^4\Psi\,. \tag{3.42}$$

The next step is to write this in terms of the slow variable $Y = \epsilon\bar{y}$,

$$\mathscr{Z} = \nabla^4\Psi + \frac{\epsilon^2}{2}(\partial_x^2 - \partial_y^2)\partial_{YY}\Psi + \frac{\epsilon^4}{16}\partial_{YYYY}\Psi\,. \tag{3.43}$$

which accurate to $O(\epsilon^2)$ is precisely (3.27).

Now, Fourier transform (3.26) and (3.27), noting the identity,

$$\mathbb{F}\left\{y^n f(x,y,\bar{y})\right\} = i^n\frac{\partial\tilde{f}(p,q,\bar{y})}{\partial q^n}\,, \tag{3.44}$$

where $\mathbb{F}$ denotes the Fourier transform that takes functions from $(x,y,\bar{y})$ to $(p,q,\bar{y})$ space. The relation between $\tilde{\Psi}$ and $\tilde{\mathscr{Z}}$, (3.43) is now

$$\tilde{\mathscr{Z}} = k^4\tilde{\Psi} + \frac{\epsilon^2}{2}(q^2 - p^2)\partial_{YY}\tilde{\Psi} + O(\epsilon^4)\,, \tag{3.45}$$

where we have defined, $k^2 = p^2 + k^2$ the correlation equation is,

$$2\mu\tilde{\mathscr{Z}} = \tilde{\Xi} - \epsilon\left(-pU_Y\tilde{\mathscr{Z}}_q + 2\beta pq\tilde{\Psi}_Y\right) + O(\epsilon^3)\,. \tag{3.46}$$

Substituting, (3.45) in (3.47), we finally get the equation in Ψ that we need to solve,

$$2\mu k^4\tilde{\Psi} = \tilde{\Xi} + \epsilon\underbrace{\left[pU_Y(k^4\tilde{\Psi})_q - 2\beta pq\tilde{\Psi}_Y\right]}_{\overset{\text{def}}{=}\mathsf{L}_1\tilde{\Psi}} + \epsilon^2\underbrace{\left[\mu(p^2 - q^2)\partial_{YY}\tilde{\Psi}\right]}_{\overset{\text{def}}{=}\mathsf{L}_2\tilde{\Psi}} + O(\epsilon^3)\,, \tag{3.47}$$

and for future reference, we have introduced the linear operators L_1 and L_2.

3.B Solution of perturbed equation by iteration

Our lowest order solution is the homogenous laminar solution,

$$\tilde{\Psi}_{\mathsf{H}}(p,q) = \frac{\tilde{\Xi}}{2\mu h^4}\,. \tag{3.48}$$

Starting from $\tilde{\Psi}_{\mathsf{H}}$, we can obtain a solution of (3.47) by iteration and in terms of the operators L_1 and L_2, we get

$$\tilde{\Psi} = \tilde{\Psi}_{\mathsf{H}} + \epsilon \mathsf{L}_1 \tilde{\Psi}_{\mathsf{H}} + \epsilon^2 (\mathsf{L}_1 \mathsf{L}_1 \tilde{\Psi}_{\mathsf{H}} + \cancelto{0}{\mathsf{L}_2 \tilde{\Psi}_{\mathsf{H}}}\ ) + O(\epsilon^3)\,. \tag{3.49}$$

The reason the $\mathsf{L}_2\tilde{\Psi}_{\mathsf{H}}$ term vanishes is because $\tilde{\Psi}_{\mathsf{H}}$ is only a function of (p,q) whereas L_2 contains a double Y-derivative. Now we need to calculate the Reynolds stress, which can be obtained, starting from the Fourier space equivalent of (3.22),

$$\sigma = \overline{u'v'} = -\iint pq\tilde{\Psi} \mathrm{d}\,p\,\mathrm{d}\,q\,. \tag{3.50}$$

To find the Reynolds stress, we subsitute (3.49) in (3.50) and evaluate the integrals at each order in ϵ in the form,

$$\sigma = \sigma_0 + \epsilon\sigma_1 + \epsilon^2\sigma_2 + O(\epsilon^3)\,. \tag{3.51}$$

The integrals involved in σ_0, σ_1 and σ_3 are rather laborious but the general approach is as follows: since the operator, L_1 does not involve p-derivatives, the procedure is to repeatedly integrate by parts in q till no derivatives of $\tilde{\Xi}$ remain for each term in the integrand of (3.50). Then we transform to polar coordinates $(p,q) = k(\cos\phi, \sin\phi)$ and get

$$\sigma_0 = -\frac{1}{4\mu}\int_0^\infty \frac{1}{k}\oint \sin 2\phi\,\tilde{\Xi}(k,\phi)\frac{\mathrm{d}\,\phi\,\mathrm{d}\,k}{4\pi^2}\,, \tag{3.52}$$

$$\sigma_1 = -\frac{U_Y}{4\mu^2}\int_0^\infty \frac{1}{k}\oint \cos\phi\cos 3\phi\,\tilde{\Xi}(k,\phi)\frac{\mathrm{d}\,\phi\,\mathrm{d}\,k}{4\pi^2}\,, \tag{3.53}$$

$$\begin{aligned}\sigma_2 = \frac{1}{8\mu^3}\Bigg[&3U_Y^2 \int_0^\infty \frac{1}{k}\oint \cos^2\phi\sin 4\phi\,\tilde{\Xi}(k,\phi)\,\frac{\mathrm{d}\,\phi\,\mathrm{d}\,k}{4\pi^2} \\ &-\beta U_{YY}\int_0^\infty \frac{1}{k^3}\oint \cos\phi\cos 3\phi\sin 2\phi\,\tilde{\Xi}(k,\phi)\,\frac{\mathrm{d}\,\phi\,\mathrm{d}\,k}{4\pi^2}\Bigg]\,.\end{aligned} \tag{3.54}$$

Now, using the radial δ-function dependence of $\tilde{\Xi}(p, q)$ in (3.12) to evaluate the k-integral trivially, we are only left with an integral in ϕ, which is also fairly simple. If this procedure is followed then we finally get the result shown in (3.29).

Chapter 3 is currently being prepared for submission for publication of the material. The dissertation author was the primary investigator and author of this material. W.R. Young supervised and directed this research.

4 Reynolds stress and eddy diffusivity of β-plane shear flows

Abstract. The Reynolds stress induced by anisotropically forcing an unbounded Couette flow, with uniform shear γ, on a β-plane, is calculated in conjunction with the eddy diffusivity of a co-evolving passive tracer. The flow is damped by linear drag on a time scale μ^{-1}. The stochastic forcing is white-noise in time and its spatial anisotropy is controlled by a parameter α, that characterizes whether eddies are elongated along the zonal direction ($\alpha < 0$), along the meridional direction ($\alpha > 0$) or are isotropic ($\alpha = 0$). The Reynolds stress varies linearly with α and non-linearly and non-monotonically with γ; but the Reynolds stress is independent of β. For positive values of α, the Reynolds stress displays a "anti-frictional" effect (energy is transferred from the eddies to the mean flow) and a frictional effect for negative values of α. When $\gamma/\mu \ll 1$, these transfers can be identified as negative and positive eddy-viscosities, respectively. With $\gamma = \beta = 0$, the meridional tracer eddy diffusivity is $\overline{v'^2}/(2\mu)$, where v' is the meridional eddy velocity. In general, non-zero β and γ suppress the eddy diffusivity below $\overline{v'^2}/(2\mu)$. When the shear is strong, the suppression due to γ varies as γ^{-1} while the suppression due to β varies between β^{-1} and β^{-2} depending on whether the shear is strong or weak, respectively.

4.1 Introduction

In this work we consider a canonical linear problem: the stochastically forced, linearized β-plane vorticity equation with a background mean shear γ

$$\zeta'_t + \gamma y \zeta'_x + \beta v' + \mu \zeta' = \xi \, . \tag{4.1}$$

The eddy vorticity is related to the eddy stream function by $\zeta' = \psi'_{xx} + \psi'_{yy}$, and the eddy velocities are $(u', v') = (-\psi'_y, \psi'_x)$. The random forcing, $\xi(x, y, t)$ is spatially homogenous and white-noise in time, and characterized more precisely in section 2. Drag, with coefficient μ, is the dissipative mechanism.

Our main concern is the eddy transport of momentum, potential vorticity and tracer in the ultimate statistically steady state of the model (4.1). Despite the evident importance of this linear problem, to our knowledge it has only been discussed previously by *Farrell and Ioannou* [1993b] and *Bakas and Ioannou* [2013], for the case of weak background shear. The problem is, however, closely related to the initial value problem for the evolution of linearized disturbances on an unbounded viscous Couette flow, first considered by *Kelvin* [1887] and *Orr* [1907]. A main result of these early studies is that an initial sinusoidal disturbance with crests "leaning" into the shear is amplified for some time. Various aspects of the Kelvin-Orr initial value problem, such as the inclusion of planetary vorticity gradient β and a spectrum of initial disturbances, were subsequently discussed by *Rosen* [1971], *Tung* [1983], *Boyd* [1983] and *Shepherd* [1985]. The transient amplification of Kelvin and Orr is now understood as one consequence of the non-normality of the linear vorticity equation [*Farrell*, 1982].

In conjunction with the vorticity equation (4.1), it is instructive to consider the co-evolution of a passive tracer $c'(x, y, t)$ satisfying the linearized tracer equation

$$c'_t + \gamma y c'_x + \beta_c v' + \mu c' = 0 \, . \tag{4.2}$$

where β_c is the large-scale tracer gradient. For simplicity, we assume that the scalar damping rate, μ, is the same as that of the vorticity. The tracer c' differs from the vorticity ζ' because there is no stochastic forcing in (4.2). Instead, scalar fluctuations are created by the eddy velocity v' stirring the mean gradient β_c.

Statistically steady solutions of (4.1) and (4.2) are characterized by the Reynolds stress

$$\sigma \stackrel{\text{def}}{=} \overline{u'v'}\,, \tag{4.3}$$

and the tracer eddy diffusivity

$$\kappa_{\mathrm{e}} \stackrel{\text{def}}{=} -\frac{\overline{v'c'}}{\beta_c}\,. \tag{4.4}$$

The overline above indicates either a zonal or an ensemble average. Using the correlation-function formalism of *Srinivasan and Young* [2012] we provide explicit analytic results for σ, κ_{e}, and other quadratic statistics, such as the eddy kinetic energy and enstrophy, and the anisotropy of the velocity field.

The correlation-function formalism — introduced in sections 2 and 4 — is an economical framework for analysis of the statistically steady flow. Rather than solving (4.1) and (4.2) explicitly and then averaging the solution, one averages at the outset, and then solves steady deterministic equations that directly provide σ and κ_{e}.

Farrell and Ioannou [1993b] have previously discussed the statistically steady flow corresponding to (4.1) with $\beta = 0$. *Farrell and Ioannou* [1993b] use the eddy kinetic energy (rather than σ and κ_{e}) as the main statistical descriptor of the flow and they emphasize viscosity (rather than Ekman drag) as the dissipative mechanism. In the related context of surface geostrophy, the tracer equation has recently been considered (with $\gamma = 0$) by Ferrari & Nikurashin (2010) and Klocker, Ferrari & LaCasce (2012).

The forcing and drag terms in (4.1) incorporate the effects of two different processes, that we characterize as *external* and *internal.* External processes, such as small-scale convection in planetary atmospheres [*Smith*, 2004; *Scott and Polvani*, 2007] or baroclinic instability [*Williams*, 1978], are often modeled as a stochastic driving agent combined with a damping term representing Ekman friction (Vallis 2006, section 2.12.6). On the other hand, internal nonlinear interactions — that is $J(\psi', \zeta')$ — are sometimes represented using a stochastic turbulence model [*DelSole*, 2001]. This is the interpretation of ξ and μ in the studies of *Farrell and Ioannou* [2003, 2007], *Ferrari and Nikurashin* [2010] and *Klocker et al.* [2012].

As suggested by fluctuation-dissipation arguments, the turbulence model has a stochastic forcing term and eddy-damping; the combination ensures energy conservation. In section 2 we introduce a forcing which is distributed anisotropically around a circle in wavenumber space.

Section 4.2 contains a description of the forcing structure and symmetries of the correlation functions. Section 4.3 shows that (4.1) and (4.2) have a statistical Galilean symmetry implying that all quadratic statistics, in particular σ and κ_{e}, are independent of y. Section 4.4 summarizes the quadratic power integrals that follow from taking quadratic averages of (4.1) and (4.2). These power integrals are used to obtain some simple and general bounds on σ and κ_{e}. Analytic expressions for σ and κ_{e} are presented in sections 4.5 and 4.6. Section 4.7 is a conclusion and discussion of the results. Technical details are relegated to the appendices.

4.2 Correlation functions and statistical symmetries

We assume that the stochastic forcing $\xi(x, y, t)$ in (4.1) is temporal white-noise, with a two-point, two-time correlation function

$$\overline{\xi(\boldsymbol{x}_1, t_1)\xi(\boldsymbol{x}_2, t_2)} = \delta(t_1 - t_2)\,\Xi(\boldsymbol{x})\,. \tag{4.5}$$

We restrict attention to spatially homogeneous forcing, so that Ξ depends only on the difference $\boldsymbol{x} = \boldsymbol{x}_1 - \boldsymbol{x}_2$.

We do not assume that the forcing is isotropic: $\Xi(\boldsymbol{x})$ might depend on the direction of the two-point separation $\boldsymbol{x} = (x, y)$. One motivation for examining the effect of anisotropy is that in many studies of zonal jets on the β-plane [*Vallis and Maltrud*, 1993; *Smith*, 2004] and on the sphere [*Williams*, 1978; *Scott and Polvani*, 2007; *Showman*, 2007], the small scale-forcing used to drive the jets is assumed to be isotropic, even though the physical processes that the forcing models, such as baroclinic instability in the ocean and moist convection in planetary atmospheres are typically not isotropic [*Arbic and Flierl*, 2004; *Li et al.*, 2006].

4.2.1 A remark on scale separation and homogeneity in y

The background mean flow, γy in (4.1) can be interpreted as a *local* approximation to a mean flow $U(y)$ that is slowly varying relative to the eddy scale and to the scale of $\Xi(\boldsymbol{x})$. At a particular position, y, the mean flow is

$$U(y) \approx U(0) + \gamma y \,, \tag{4.6}$$

where $\gamma = U'(0)$. However the constant $U(0)$ has no physical consequences in this model: one can move the origin of the coordinate system with $\tilde{y} = y + U(0)/\gamma$ to remove $U(0)$ from the problem. This removal hinges on the spatial homogeneity of the statistical properties of $\xi(x, y, t) = \xi(x, \tilde{y} - U(0)/\gamma, t)$. In particular Ξ is unaltered by this shift of the origin.

4.2.2 Statistical properties of the solution

The statistical properties of the solution are encapsulated in two-point same-time correlation functions:

$$\mathcal{Z}(\boldsymbol{x}) \stackrel{\text{def}}{=} \overline{\zeta_1' \zeta_2'} \,, \qquad \text{and} \qquad \Psi(\boldsymbol{x}) \stackrel{\text{def}}{=} \overline{\psi_1' \psi_2'} \,. \tag{4.7}$$

In (4.7), $\zeta_n' = \zeta'(x_n, y_n, t)$ is the eddy vorticity at point (x_1, y_1) and likewise for ψ_n'; x and y are the components of the two-point separation $\boldsymbol{x} = \boldsymbol{x}_1 - \boldsymbol{x}_2$. In (4.7) we have anticipated that statistical properties of the solution are spatially homogeneous so that the correlation functions $\mathcal{Z}$ and Ψ depend only on the separation $\boldsymbol{x} = \boldsymbol{x}_1 - \boldsymbol{x}_2$. The correlation functions Ψ and $\mathcal{Z}$ are connected by the biharmonic equation

$$\mathcal{Z} = (\partial_x^2 + \partial_y^2)^2 \Psi \,. \tag{4.8}$$

The statistics of the scalar are characterized by

$$P(\boldsymbol{x}) \stackrel{\text{def}}{=} \overline{\psi_1' c_2'} \,, \quad \text{and} \quad Q(\boldsymbol{x}) \stackrel{\text{def}}{=} \overline{\psi_2' c_1'} \,, \tag{4.9}$$

and

$$C(\boldsymbol{x}) \stackrel{\text{def}}{=} \overline{c_1' c_2'} \,. \tag{4.10}$$

4.2.3 Exchange symmetries

Because the notation of one point as “1” and the other point as “2” is arbitrary, the correlation function Ξ has the “exchange symmetry”

$$\Xi(x,y) = \Xi(-x,-y)\,. \tag{4.11}$$

The exchange symmetry implies that Ξ is unchanged by a rotation of 180° in the plane of $\boldsymbol{x}$, and ensures that the spectrum,

$$\tilde{\Xi}(p,q) \overset{\mathrm{def}}{=} \iint \mathrm{e}^{-\mathrm{i}px-\mathrm{i}qy}\,\Xi(x,y)\,\mathrm{d}x\mathrm{d}y\,, \tag{4.12}$$

is real.

The auto-correlations functions $\mathcal{Z}$, Ψ and C all satisfy the exchange symmetry (4.11). For the mixed statistics in (4.9), exchange implies

$$P(x,y) = Q(-x,-y)\,. \tag{4.13}$$

The Fourier transform of this relation shows that

$$\tilde{P}(p,q) = \tilde{Q}^{*}(p,q)\,. \tag{4.14}$$

4.2.4 Reflexion symmetry

If the statistics of the forcing are reflexionally symmetric in the axis of x, then the correlation function has a second symmetry

$$\Xi(x,y) = \Xi(x,-y)\,. \tag{4.15}$$

The exchange symmetry (4.11) in concert with (4.15) implies that Ξ is an even function of *both* arguments.

Now the left of (4.1) is unchanged by

$$\psi \to \psi\,, \qquad t \to t\,, \qquad x \to x\,, \tag{4.16}$$

$$\gamma \to -\gamma\,, \qquad y \to -y\,. \tag{4.17}$$

This transformation induces $(u', v') \to (-u', v')$, and therefore $\sigma \to -\sigma$. If the statistics of the forcing ξ also obey (4.15), then (4.17) is a statistical symmetry of (4.1) and therefore

$$\sigma(\gamma) = -\sigma(-\gamma)\,. \tag{4.18}$$

But the symmetry (4.15) is not compulsory e.g., the single-wave forcing of *Ferrari and Nikurashin* [2010] and *Klocker et al.* [2012] does not satisfy (4.15). However we make the assumption that the forcing is reflexionally symmetric and proceed confining attention to ξ's with statistics obeying (4.15). As a consequence of this restriction, $\sigma(\gamma)$, calculated explicitly in section 4.5, satisfies (4.18).

4.2.5 The stochastic forcing

Our main illustrative example is provided by the correlation function

$$\Xi = 2\varepsilon k_f^2 \left[J_0(k_f r) - \alpha_c J_2(k_f r)\cos 2\theta \right] , \tag{4.19}$$

where $(x, y) = r(\cos\theta, \sin\theta)$, k_f is the "forced wavenumber" and $J_m(z)$ is the Bessel function of order m. The corresponding spectrum is

$$\tilde{\Xi}(p, q) = 4\pi k_f \varepsilon \left(1 + \alpha_c \cos 2\phi\right) \delta(k - k_f)\,, \tag{4.20}$$

with $(p, q) = k(\cos\phi, \sin\phi)$. The forcing is concentrated on a circle with radius k_f in wavenumber space. To ensure that the spectrum is non-negative, the anisotropy parameter α_c must satisfy $-1 \le \alpha \le 1$. Figure 4.1 shows model correlation functions and forcing obtained by varying α_c in (4.19).

4.3 Statistical Galilean invariance

The linearized vorticity equation in (4.1), with the rapidly decorrelating forcing in (4.5), has a form of statistical Galilean invariance. To explain this, consider two observers, one of whom is stationary and at the origin of the (x, y, t) coordinate system in (4.1). The other observer is at $y = b$ and moves "with the mean flow", at speed γb along the axis of x relative to the first. Because of the rapid temporal decorrelation of the forcing ξ, these two observers see statistically

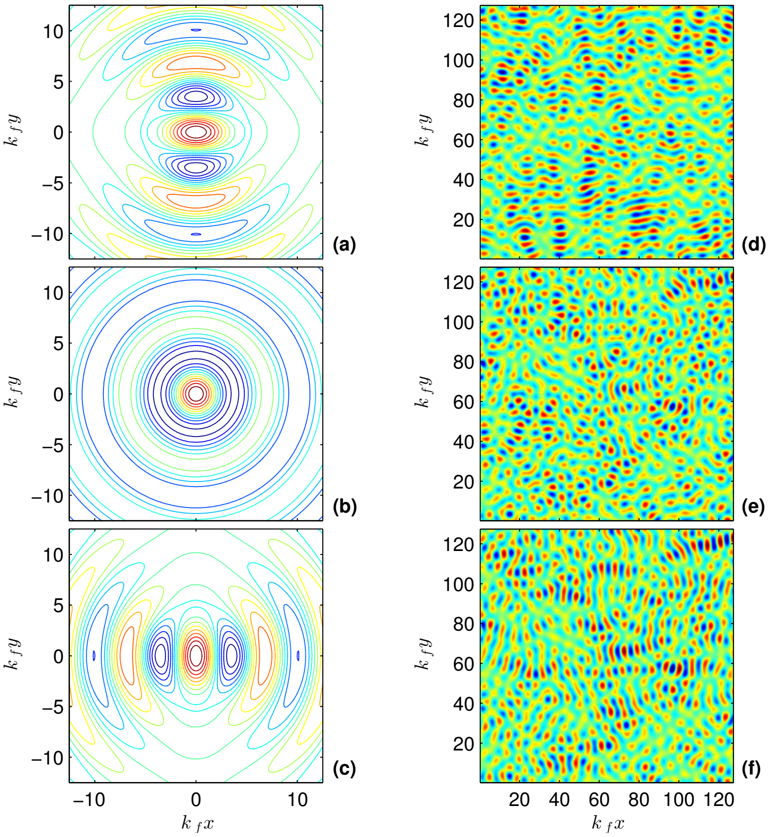

Figure 4.1: The left panels show the anisotropic ring correlation function Ξ in (4.19) and the right panels show corresponding snapshots of the forcing ξ. Panels (a) and (d) show $\alpha_c = -1$; (b) and (e) show the isotropic case $\alpha_c = 0$; panels (c) and (f) show $\alpha_c = +1$.

identical versions of the problem (4.1). Thus all zonally averaged quantities are independent of y. This simple argument allows us to anticipate some curious aspects of the detailed calculations which follow in section 4.5.

Notice that if the forcing has a non-zero temporal decorrelation time then the statistical properties of ξ are different in the two frames of reference, and consequently the problem is no longer statistically Galilean invariant (or even Galilean invariant). If there is a non-zero decorrelation time then averaged quantities do depend on y. A clear example is steady forcing, such as $\xi = \cos k_f x$ used by *Manfroi and Young* [1999]. In the frame of the observer at $y = b$ this forcing is periodic in time. In this example the forcing breaks Galilean invariance because there is a special frame in which the forcing is steady (or has the longest decorrelation time in the stochastic case).

To formally prove statistical Galilean invariance, suppose that the second observer above uses coordinates $(\tilde{x}, \tilde{y}, \tilde{t})$. The relation between the two coordinate systems is

$$\tilde{x} = x - \gamma b t\,, \qquad \tilde{y} = y - b\,, \qquad \tilde{t} = t\,. \tag{4.21}$$

In the "tilde frame" the equation of motion (4.1) is

$$\zeta'_{\tilde{t}} + \gamma \tilde{y} \zeta'_{\tilde{x}} + \beta v' + \mu \zeta' = \xi(\tilde{x} + \gamma b t, \tilde{y} + b, \tilde{t})\,. \tag{4.22}$$

If the right hand side of (4.22) has the same statistical properties as $\xi(x, y, t)$ in (4.1) then this Galilean transformation is a statistical symmetry. And indeed, because of the $\delta(t_1 - t_2)$ correlation in (4.5), this is the case.

The important consequence of statistical Galilean invariance is that zonally averaged quantities are independent of y, despite the explicit y-dependence in (4.1) and (4.2). As an application of this result, the eddy vorticity flux is related to the Reynolds stress by the Taylor identity

$$\overline{v'\zeta'} = -\left(\overline{u'v'}\right)_y\,. \tag{4.23}$$

Because $\overline{u'v'}$ is independent of y it follows that the statistically steady solution of (4.1) must have

$$\overline{v'\zeta'} = 0\,. \tag{4.24}$$

That is, there is no eddy flux of vorticity, even though the planetary vorticity βy is stirred by eddies (but see the discussion surrounding (4.45)).

4.4 Power integrals

4.4.1 Enstrophy

The enstrophy power integral is obtained by multiplying (4.1) by ζ' and zonally averaging. Using (4.24), the result is

$$\mu \overline{\zeta'^2} = \overline{\xi \zeta'}\,. \tag{4.25}$$

Because there is no production of eddy enstrophy by stirring of the β-gradient, there is a strict balance in (4.25) between local eddy enstrophy production on the right and enstrophy dissipation by drag on the left.

4.4.2 Energy

The energy power integral is obtained by multiplying the vorticity equation (4.1) by ψ' and zonally averaging. Again, because of statistical Galilean symmetry, zonally averaged quantities, such as $\overline{u'^2}$, are independent of y and one finds

$$\gamma\overline{u'v'} = \varepsilon - \mu \left(\overline{u'^2} + \overline{v'^2}\right) . \tag{4.26}$$

The left of (4.26) is the transfer of energy between the eddies and the shear flow. The first term on the right of (4.26),

$$\varepsilon \overset{\text{def}}{=} -\overline{\psi'\xi} \, , \tag{4.27}$$

is the rate of working of the stochastic force. Because the forcing is white-in-time, ε in (4.27) is the same as ε in (4.19) and (4.20). A more detailed discussion of this aspect can be found in *Srinivasan and Young* [2012].

4.4.3 Tracer variance

The tracer variance equation is obtained by multiplying the scalar equation (4.2) by c' and zonally averaging:

$$\beta_c \, \overline{v'c'} + \mu\overline{c'^2} = 0 \, . \tag{4.28}$$

Thus $\kappa_{\mathrm{e}} = \mu\overline{c'^2}/\beta_c^2$: the tracer eddy diffusivity is non-zero and positive. Taylor's analogy between eddy transport of vorticity and eddy transport of scalars fails: according to (4.24) there is no eddy flux of vorticity, while from (4.28) there must be a down-gradient tracer flux.

4.4.4 Covariance of tracer and vorticity

The fourth and final power integral is obtained by "cross-multiplying" the vorticity equation (4.1) and the scalar equation (4.2):

$$\beta\,\overline{v'c'} + 2\mu\overline{c'\zeta'} = 0\,, \tag{4.29}$$

and therefore $\kappa_\mathrm{e} = 2\mu\overline{\zeta'c'}/\beta\beta_c$. The power integral (4.29) relates the tracer eddy flux to the covariance $\overline{c'\zeta'}$ and, in combination with (4.28), shows that $2\beta_c\overline{c'\zeta'} = \beta\overline{c'^2} > 0$.

4.4.5 A bound on the Reynolds stress

Combining the energy power integral (4.26) with the inequality $\overline{u'^2} + \overline{v'^2} \le 2\overline{u'v'}$ we obtain

$$\sigma \le \frac{\varepsilon}{\gamma + 2\mu}\,. \tag{4.30}$$

This bound on the Reynolds stress is important because it is independent of the details of the forcing (i.e., the model for Ξ) and because in (4.44) below, the bound is saturated.

4.4.6 Bounds on the eddy diffusivity

Combining the tracer variance power integral (4.28) with the Cauchy-Schwarz inequality,

$$|\overline{v'c'}| \le \sqrt{\overline{c'^2}\,\overline{v'^2}}\,, \tag{4.31}$$

we obtain

$$\kappa_\mathrm{e} \le 2\kappa_v\,, \tag{4.32}$$

where

$$\kappa_v \overset{\mathrm{def}}{=} \frac{\overline{v'^2}}{2\mu}\,. \tag{4.33}$$

Another bound on κ_e is obtained by combining the covariance integral (4.29) with the Cauchy-Schwarz inequality for $\overline{\zeta'c'}$. One finds

$$\kappa_\mathrm{e} \le 2\kappa_\zeta\,, \tag{4.34}$$

where

$$\kappa_\zeta \overset{\text{def}}{=} \frac{2\mu\overline{\zeta'^2}}{\beta^2}\,. \tag{4.35}$$

A more elaborate analysis in Appendix A shows that (4.33) and (4.35) can be combined into a single stronger inequality

$$\kappa_{\mathrm{e}} \le \frac{2\kappa_v\kappa_\zeta}{\kappa_v+\kappa_\zeta}\,, \tag{4.36}$$

or equivalently in terms of harmonic averages

$$\frac{1}{\kappa_{\mathrm{e}}} \ge \frac{1}{2}\left(\frac{1}{\kappa_v}+\frac{1}{\kappa_\zeta}\right)\,. \tag{4.37}$$

We will see later that the bounds above are typically too generous by a factor of two.

The four power integrals, and the ensuing bounds on σ and κ_{e}, provide important and general connections between quadratic statistics characterizing the main properties of the flow. However these relations are unclosed and to make further progress we consider the dynamics of correlation functions.

4.5 Reynolds stress and anisotropy

An evolution equation for the correlation function $\mathcal{Z}$ in (4.7) is obtained using the replica trick: take (4.1) at point 1 and multiply by ζ_2' and vice versa. Adding these two expressions and then zonally averaging one finds

$$\gamma y\partial_x\mathcal{Z} = \Xi - 2\mu\mathcal{Z}\,. \tag{4.38}$$

The enstrophy and energy power integrals in (4.25) and (4.26) are recovered by evaluating (4.38), and the inverse laplacian of (4.38), at zero separation. A surprising aspect of (4.38) is the lack of a term containing β: the β-term that would appear in the left hand side of (4.38), on performing the replica trick mentioned above is,

$$\beta\left(\overline{v_1'\zeta_2'}+\overline{v_2'\zeta_1'}\right) = \beta(\partial_{x_1}+\partial_{x_2})\nabla^2\Psi\,. \tag{4.39}$$

The term above is zero because, owing to the homogeniety property of Ψ section 4.2a, $\partial_{x_1} = -\partial_{x_2} = \partial_x$. For a more detailed and general derivation of (4.38), see *Srinivasan and Young* [2012].

Once one has the solution of (4.38), the Reynolds stress is given by

$$\overline{u'v'} = \Psi_{xy}(0,0)\,. \tag{4.40}$$

It is remarkable that the vorticity correlation equation (4.38) is independent of β i.e., anisotropic Rossby wave propagation does not affect the vorticity correlation function $\mathcal{Z}(x,y)$, nor the Reynolds stress in (4.40). Thus all results in this section, which follow from the solution of (4.38) alone, apply to β-plane flows, even though the parameter β does not appear.

4.5.1 Reynolds stress

A general solution of (4.38) is detailed in Appendix B. With the anisotropic ring forcing in (4.15), the Reynolds stress $\sigma = \overline{u'v'}$ obtained from (4.40) is

$$\sigma = \frac{\varepsilon\alpha_c}{4\mu}\,F_1\left(\frac{\gamma}{\mu}\right)\,, \tag{4.41}$$

where the function F_1 is

$$F_1\left(\frac{\gamma}{\mu}\right) \overset{\text{def}}{=} 4\mu\gamma\int_0^\infty \frac{\tau^2\mathrm{e}^{-\tau}}{16\mu^2+\gamma^2\tau^2}\,\mathrm{d}\tau\,. \tag{4.42}$$

The function F_1 can be expressed in terms of the exponential integral (see Appendix C), and is shown in Figure 4.2.

We emphasize the linear dependence of σ in (4.41) on the forcing anisotropy parameter α. In particular, if $\alpha = 0$ (isotropic forcing), there is no Reynolds stress. This recapitulates the result that anisotropic forcing, or initial conditions, are essential to the generation non-zero Reynolds stress [*Kraichnan*, 1976; *Shepherd*, 1985; *Farrell and Ioannou*, 1993b; *Holloway*, 2010; *Cummins and Holloway*, 2010; *Srinivasan and Young*, 2012].

The Reynolds stress (4.41) depends nonlinearly on the shear γ and thus the concept of an eddy viscosity is not generally useful. Instead, there is a nonlinear,

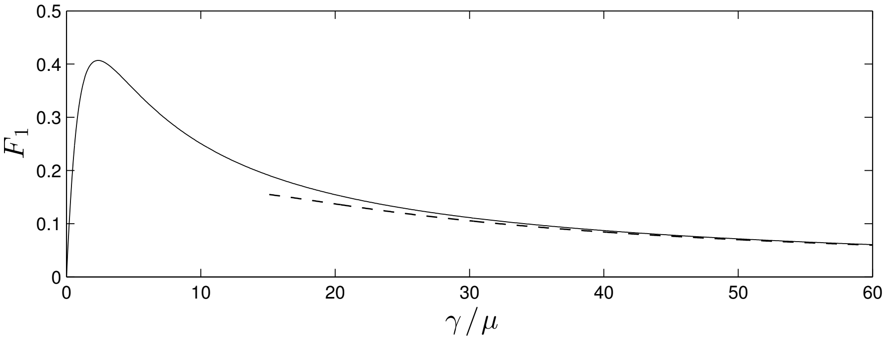

Figure 4.2: F_1 in (4.42) as a function of the non-dimensional shear γ/μ. The dashed curve is the approximation $F_1(\gamma/\mu) = 4\mu/\gamma + O(\mu/\gamma)^2$.

and non-monotonic, stress-strain relation encoded in F_1. However in the weak-shear limit, $\gamma/\mu \ll 1$, the integral in (4.42) simplifies and the Reynolds stress is then

$$\sigma \approx \underbrace{\frac{\varepsilon\alpha_c}{8\mu^2}}_{=-\nu_\mathrm{e}} \gamma \,. \tag{4.43}$$

The sign of the eddy viscosity ν_e is determined by the anisotropy parameter α_c, with $\alpha_c > 0$ being the antifrictional case. A negative viscosity in the weak shear limit, with the same form as (4.43), was also found by *Bakas and Ioannou* [2013] using a forcing function that is similar to the $\alpha = 1$ case in this paper.

The integral in (4.42) also simplifies in the strong shear limit $\gamma/\mu \gg 1$, reducing to

$$\sigma \approx \frac{\varepsilon\alpha_c}{\gamma} \,. \tag{4.44}$$

The inverse dependence of stress on shear in the strong-shear limit is striking. This might be interpreted as an indication that strong shear is rapidly pushing wavy disturbances into the Farrell and Ioannou's "unfavorable" sector of the wavenumber plane, where they damp away due to the Kelvin-Orr mechanism[1]. But as we show in the next section, a complicating factor is the dependence of the kinetic energy density on the shear.

---

[1] In the solution in Appendix B the sheared wavenumber is $q = \hat{q} - p\gamma t$, where $\hat{q}$ is the initial meridional wavenumber. The unfavorable sector is $q < 0$. In this sector, according to the solution of the Kelvin-Orr initial value problem, the energy of the disturbances decreases.

Another interpretation of (4.44) is that if $\alpha = \pm 1$ then the Reynolds-stress bound in (4.30) is an asymptotic equality as $\gamma/2\mu \to \infty$. One might say that the γ^{-1} dependence in (4.44) is the strongest possible Reynolds stress that can be achieved, consistent with the energy power integral (4.26) and the associated bound (4.30). Notice that (4.44) was obtained with the ansiotropic ring forcing in (4.19), but the bound (4.30), which makes no assumptions about the structure of the forcing, indicates that $\sigma \propto \gamma^{-1}$ is a general result in the strongly sheared limit.

4.5.2 The vorticity flux of a slowly varying mean flow

In the discussion surrounding (4.23) and (4.24) we argued that the vorticity flux $\overline{v'\zeta'}$ is zero. However, if following (4.6), we view γ as the shear of a slowly varying mean flow $U(y)$ then a non-zero $\overline{v'\zeta'}$ can be calculated with our results. Using this “slowly-varying” argument we can write the Reynolds stress as a function of the shear,

$$\overline{u'v'} = \sigma(U_y)\,, \tag{4.45}$$

where σ is the function in (4.41). Then using the Taylor identity (4.23) one has

$$\overline{v'\zeta'} = -\sigma'(U_y)\,U_{yy}\,, \tag{4.46}$$

where σ' is the derivative with respect to γ.

4.5.3 Eddy kinetic energy and enstrophy

In addition to the Reynolds stress, the statistically steady solution is characterized by the eddy enstrophy and the eddy kinetic energy. The eddy enstrophy is obtained by evaluating (4.38) at $\boldsymbol{x} = 0$ and is simply

$$\overline{\zeta'^2} = \frac{\Xi(0,0)}{2\mu} = \frac{\varepsilon k_f^2}{\mu}\,. \tag{4.47}$$

There is no dependence of the eddy enstrophy on the parameter γ/μ (nor on β).

The eddy kinetic energy is obtained from the energy power integral (4.26). For anisotropic ring forcing, the result is

$$\underbrace{\tfrac{1}{2}\left(\overline{u'^2} + \overline{v'^2}\right)}_{\overset{\text{def}}{=}E'} = \frac{\varepsilon}{2\mu}\left(1 - \frac{\gamma\alpha_c}{4\mu}\,F_1\right)\,. \tag{4.48}$$

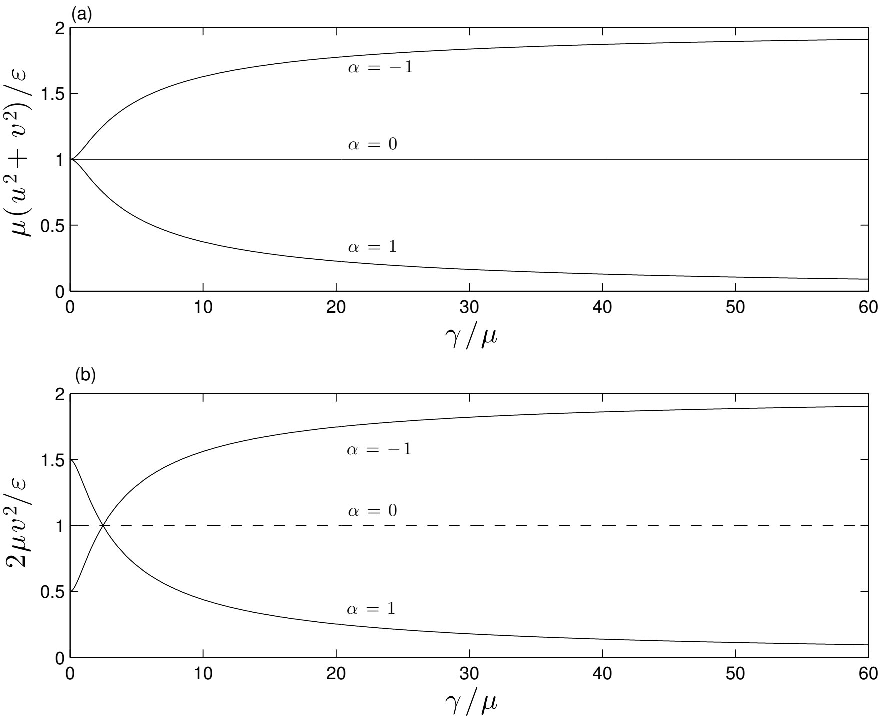

Figure 4.3: (a) The non-dimensional eddy kinetic energy as a function of γ/μ, calculated from (4.48). (b) The non-dimensional meridional velocity variance as a function of γ/μ.

Figure 4.3(a) shows the scaled eddy kinetic energy, $2\mu E'/\varepsilon$, as a function of γ/μ. The anti-frictional case is $\alpha = +1$, with $2\mu E'/\varepsilon < 1$ i.e., the eddy kinetic energy is depleted below the unsheared value by transfer to the large-scale shear flow. In the frictional case ($\alpha = -1$) the eddy kinetic energy is enhanced by transfer from the mean flow: the energy level approaches twice that of the isotropically forced flow as the shear increases.

In the strong-shear limit in Figure 4.3(a) there is much more eddy energy in the frictional flow ($\alpha_c = -1$) than in the anti-frictional flow ($\alpha_c = +1$). Yet the amplitude of the Reynolds stress in (4.44) is the same in the two cases. The relatively energetic $\alpha_c = -1$ eddies are inefficient at forming the requisite correlation to produce a Reynolds stress. This motivates further examination of the anisotropy of the eddies.

4.5.4 Velocity anisotropy

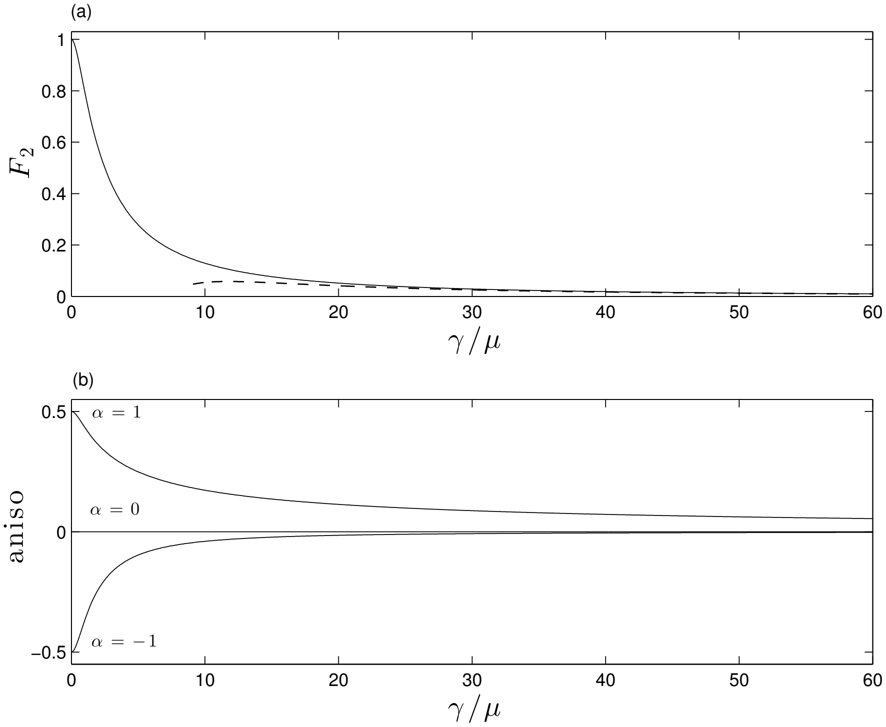

Figure 4.4: (a) The function $F_2(\gamma/\mu)$ defined in (4.50). The dashed curve is the asymptotic approximation $(16\mu^2/\gamma^2)[\ln(\gamma/4\mu) - \gamma_E]$, where $\gamma_E = 0.57721\cdots$ is Euler's constant. (b) The index aniso in (4.51), with $\alpha = -1$, 0 and 1.

In Appendix B we show that the mean square meridional velocity is

$$\overline{v'^2} = \frac{\varepsilon}{2\mu}\left[1 + \frac{\alpha}{2}\left(F_2 - \frac{\gamma}{2\mu}F_1\right)\right], \tag{4.49}$$

where F_1 is in (4.42) and

$$F_2\left(\frac{\gamma}{\mu}\right) = 16\mu^2 \int_0^\infty \frac{\tau \mathrm{e}^{-\tau}}{16\mu^2 + \gamma^2\tau^2}\,\mathrm{d}\tau\,. \tag{4.50}$$

Figure 4.4(a) shows F_2 as a function of the non-dimensional shear, γ/μ and Figure 4.3(b) shows the variation of the mean square meridional velocity with γ/μ.

As a non-dimensional index of the flow anisotropy, we use the quantity

$$\text{aniso} \overset{\text{def}}{=} \frac{\overline{v'^2} - \overline{u'^2}}{\overline{v'^2} + \overline{u'^2}}\,, \tag{4.51}$$

or equivalently

$$\frac{\overline{v'^2}}{\overline{u'^2}} = \frac{1 + \mathrm{aniso}}{1 - \mathrm{aniso}} \,. \tag{4.52}$$

Using (4.49), the numerator in (4.51) is

$$\overline{v'^2} - \overline{u'^2} = \frac{\varepsilon \alpha_c}{2\mu} F_2 \left(\frac{\gamma}{\mu} \right) \,. \tag{4.53}$$

The dependence of the index aniso in (4.51) on the shear is shown in Figure 4.4(b).

In the large-shear limit, the case $\alpha = -1$ in Figure 4.4(b) rapidly tends to isotropy. This is consistent with the earlier result that the amplitude of the Reynolds stress in (4.44) is the same for $\alpha_c = +1$, as for $\alpha_c = -1$, despite the great difference in the energy level of the two flows as $\gamma/\mu \to \infty$. In other words, with $\alpha = -1$ the eddies are energetic but almost isotropic and are therefore not very efficient at producing a non-zero Reynolds stress.

4.5.5 Tenacity of isotropy

Figure 4.4(b) shows that if the forcing is isotropic ($\alpha = 0$) then the flow is also isotropic i.e., if the flow is isotropically forced then neither the mean shear nor the β-effect induces anisotropy of the eddies. Moreover, if the forcing is anisotropic, then the effect of shear is to make the flow more isotropic: in both panels of Figure 4.4 the index of flow anisotropy approaches zero monotonically as the shear γ/μ increases. We cannot provide an intuitive explanation of this result.

For a recent discussion of isotropy in the context of fully nonlinear sheared turbulence see *Cummins and Holloway* [2010]: a main point is that nonlinear eddy-eddy interactions also decrease anisotropy. We summarize all these results by saying that isotropy is tenacious.

4.6 The eddy diffusivity $\kappa_{\mathrm{e}}(\alpha_c, \beta, \gamma, \mu)$

We turn now to the eddy diffusivity, viewed as a function of the four main parameters: $\kappa_{\mathrm{e}}(\alpha_c, \beta, \gamma, \mu)$. Using the replica trick, one can obtain evolution equations for the tracer correlation functions defined in (4.9) and (4.10). Combining

(4.1) and (4.2) one has

$$\gamma y \nabla^2 P_x + \beta P_x + 2\mu \nabla^2 P = \beta_c \nabla^2 \Psi_x \,, \tag{4.54}$$

and from (4.2) alone one has

$$\gamma y C_x + 2\mu C = -\beta_c (P_x - Q_x) \,. \tag{4.55}$$

The equation for Q is obtained by $P \to Q$ and $(x, y) \to -(x, y)$ in (4.54). After solving (4.54), the tracer diffusivity, κ_{e} defined in (4.4), is obtained as

$$\kappa_{\mathrm{e}} = -\frac{P_x(0,0)}{\beta_c} \,. \tag{4.56}$$

The solution of (4.54), and the calculation of the tracer diffusivity κ_{e} defined in (4.4), is summarized in Appendix D. The result is

$$\kappa_{\mathrm{e}} = \frac{1}{\beta^2} \iint \tilde{\Xi}(p,q) \tilde{M}(p,q) \, \frac{\mathrm{d}p \mathrm{d}q}{(2\pi)^2} \,; \tag{4.57}$$

the kernel in (4.57) is

$$\tilde{M}(p,q;\beta,\gamma,\mu) = 1 - 2\mu \int_0^\infty \mathrm{e}^{-2\mu t} \cos\chi \, \mathrm{d}t \,, \tag{4.58}$$

with the phase

$$\chi = \frac{\beta}{\gamma p} \left[\arctan\left(\frac{q}{p} - \gamma t \right) - \arctan\left(\frac{q}{p} \right) \right] \,. \tag{4.59}$$

4.6.1 The case $\gamma = \beta = 0$

If $\beta = \gamma = 0$ then we don't need the complicated expressions for κ_{e} above: cancel the ∇^2 in (4.54) and then take an x-derivative to obtain

$$\kappa_{\mathrm{e}}(\alpha, 0, 0, \mu) = \underbrace{\frac{\overline{v'^2}}{2\mu}}_{\kappa_v} \,, \tag{4.60}$$

where we have used $\overline{v'^2} = \Psi_{xx}(0,0)$, and recalled the definition of κ_v in (4.33). Notice that the upper bound on κ_{e} in (4.32) is too generous by a factor of two relative to (4.60). Using results from section 4.5, the eddy diffusivity in (4.60) can also be written as

$$\kappa_{\mathrm{e}}(\alpha, 0, 0, \mu) = \frac{\varepsilon}{4\mu^2} \left(1 + \frac{\alpha}{2} \right) \,; \tag{4.61}$$

the dependence of κ_{e} on the anisotropy α reflects that of $\overline{v'^2}$.

4.6.2 The suppression factor, S

One can view (4.60) as saying that the eddy diffusivity is the product of a typical meridional eddy velocity, equal to the root mean square of v', times the mixing length

$$\sqrt{\overline{v'^2}}/2\mu\,. \tag{4.62}$$

We adopt this interpretation and express κ_e in terms of κ_v and *Ferrari and Nikurashin* [2010] suppression factor S as

$$\kappa_\mathrm{e} = \kappa_v\, S\,. \tag{4.63}$$

In (4.60), $S = 1$. But the effect of non-zero β and γ is usually to make κ_e less than κ_v.

4.6.3 The case $\gamma = 0$

Unlike the Reynolds stress in (4.41) and the anisotropy in (4.51), the eddy diffusivity κ_e depends on the planetary vorticity gradient β. This dependence is illustrated by the special case $\gamma = 0$. With no mean shear, the phase in (4.59) simplifies to $\chi = \omega t$, where

$$\omega = -\frac{\beta p}{p^2+q^2} \tag{4.64}$$

is the Rossby wave frequency. Thus the kernel in (4.58) reduces to

$$\tilde{M}(p,q;\beta,0,\mu) = \frac{\omega^2}{(2\mu)^2+\omega^2}\,. \tag{4.65}$$

For the anisotropic ring forcing in (4.19), the $\gamma = 0$ tracer diffusivity obtained from the integral in (4.57) is then

$$\kappa_\mathrm{e}(\alpha,\beta,0,\mu) = \frac{\varepsilon}{4\mu^2}\left(B_0 + \frac{\alpha_c}{2}\sqrt{1+\tilde{\beta}^2}\,B_0^2\right)\,, \tag{4.66}$$

where

$$\tilde{\beta} \overset{\mathrm{def}}{=} \frac{\beta}{2\mu k_f}\,, \tag{4.67}$$

is a non-dimensional planetary vorticity gradient and

$$B_0(\tilde{\beta}) \overset{\mathrm{def}}{=} \frac{2}{\tilde{\beta}^2}\left(1 - \frac{1}{\sqrt{1+\tilde{\beta}^2}}\right)\,. \tag{4.68}$$

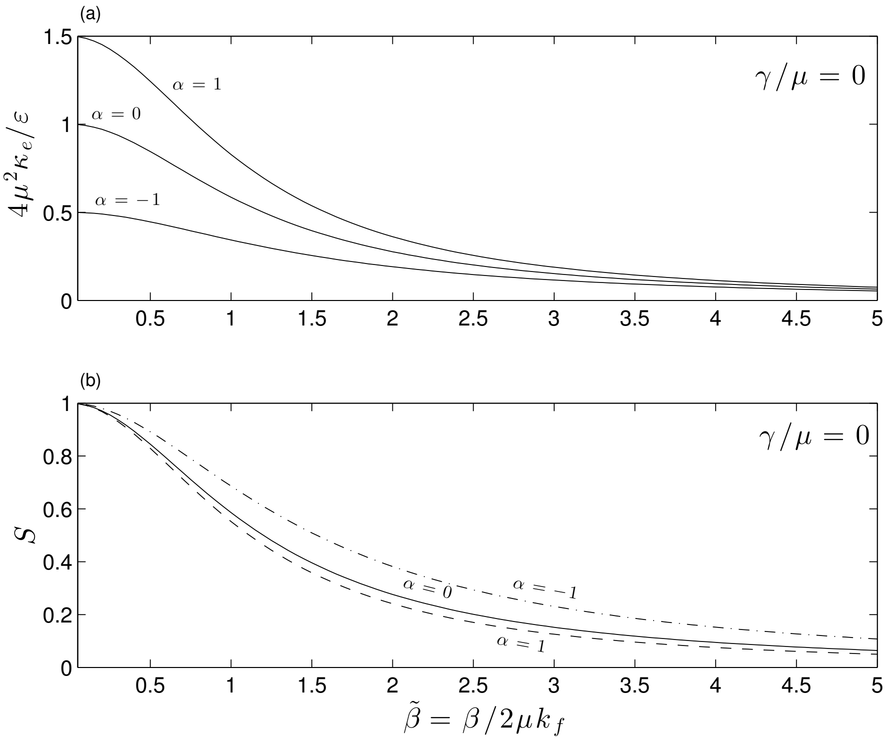

Figure 4.5: (a) The non-dimensional $\gamma = 0$ tracer diffusivity in (4.66) as a function of $\tilde{\beta} = \beta/(2\mu k_f)$. (b) The suppression factor, S defined in (4.69).

Following (4.63), the eddy diffusivity in (4.66) can alternatively be written as

$$\kappa_{\mathrm{e}}(\alpha, \beta, 0, \mu) = \underbrace{\frac{\overline{v'^2}}{2\mu}}_{\kappa_v} \underbrace{\frac{2B_0 + \alpha_c\sqrt{1+\tilde{\beta}^2}\,B_0^2}{2+\alpha_c}}_{S}, \tag{4.69}$$

Figure 4.5(a) shows the eddy diffusivity in (4.66) as a function of β, and Figure 4.5(b) shows the factor S in (4.69). Increasing β reduces both measures of the tracer diffusivity.

The dependence of κ_{e} on α in Figure 4.5(a) is intuitive: in Figure 4.1(f) $\alpha_c > 0$ forces meridionally elongated eddies resulting in enhanced diffusive fluxes in the y-direction. The difference between $\alpha_c = 1$ and $\alpha_c = -1$ is a factor of three in diffusivity at $\tilde{\beta} = 0$, but the dependence on forcing anisotropy α is reduced as $\tilde{\beta}$ increases.

When $\tilde{\beta} \to \infty$:

$$B_0(\tilde{\beta}) = 2\tilde{\beta}^{-2} + O\left(\tilde{\beta}^{-3}\right) , \tag{4.70}$$

and therefore for large $\tilde{\beta}$ the eddy diffusivity is

$$\kappa_{\mathrm{e}}(\alpha, \beta \to \infty, 0, \mu) = \frac{\varepsilon}{4\mu^2} \frac{2}{\tilde{\beta}^2} , \tag{4.71}$$

$$= \underbrace{\frac{2\mu\overline{\zeta'^2}}{\beta^2}}_{\kappa_\zeta} , \tag{4.72}$$

where we have recalled the definition of κ_ζ in (4.35). The bound (4.34) is too generous by a factor of two relative to (4.72).

The $\beta \to \infty$ diffusivity in (4.72) is a general result that is not specific to the anisotropic-ring forcing in (4.20). To see this, we note that if $\beta \to \infty$ then the kernel $\tilde{M}$ in (4.65) simplifies to

$$\tilde{M}(p, q; \beta \to \infty, 0, \mu) \to 1 . \tag{4.73}$$

Setting $\tilde{M} = 1$ in (4.69) and substituting for the enstrophy from (4.47), we arrive at (4.72).

4.6.4 Comparison with Klocker, Ferrari & LaCasce (2012)

The β^{-2} suppression of transport in (4.72) is via the mechanism of *Ferrari and Nikurashin* [2010] and *Klocker et al.* [2012]: nonzero β enables Rossby wave propagation so that eddies drift relative to the mean flow. We have used the anisotropic ring forcing in (4.20), whereas Klocker et al. force a single wave. To fully explain the connection we briefly consider the single-wave forcing of Klocker et al., with correlation function

$$\Xi(x, y) = 2\varepsilon k_f^2 \cos(p_f x + q_f y) . \tag{4.74}$$

The spectrum is

$$\begin{aligned}\tilde{\Xi}(p, q) = 4\varepsilon\pi^2 k_f^2 \,&[\delta(p - p_f)\delta(q - q_f) \\ &+ \delta(p + p_f)\delta(q + q_f)] ,\end{aligned} \tag{4.75}$$

where $k_f^2 = p_f^2 + q_f^2$. *Ferrari and Nikurashin* [2010] and *Klocker et al.* [2012] do not have damping in the scalar equation (4.2), so to see the connection to their work we replace $\mu c'$ in (4.2) by $\mu_c c'$. *Ferrari and Nikurashin* [2010] and *Klocker et al.* [2012] take $\mu_c = 0$. With $\gamma \neq 0$ this change complicates the expression for the diffusivity in (4.57). But, for comparison with *Klocker et al.* [2012] we restrict attention to $\gamma = 0$. Then there is only a minor modification in the tracer correlation equation (4.54) and the diffusivity formula in (4.125): every 2μ term is just replaced by $\mu + \mu_c$. In particular the kernel $\tilde{M}$ is modified from (4.65) to

$$\tilde{M}(p, q; \beta, 0, \mu) = \frac{\omega^2}{(\mu + \mu_c)^2 + \omega^2}\,, \tag{4.76}$$

The diffusivity integral (4.57) is modified by a factor of $(\mu + \mu_c)/2\mu$ and the diffusivity then evaluates to

$$\kappa_{\mathrm{e}} = \frac{p_f^2}{k_f^2}\frac{\mu + \mu_c}{\mu}\frac{\varepsilon}{(\mu + \mu_c)^2 + c_R^2 p_f^2}\,, \tag{4.77}$$

where

$$c_R = -\frac{\beta}{k_f^2} \tag{4.78}$$

is the intrinsic Rossby wave phase speed in the zonal direction. Alternatively, we can express (4.77) in terms of the meridional velocity variance, $\overline{v'^2}$ obtained from (4.101),

$$\overline{v'^2} = \frac{\varepsilon p_f^2}{\mu k_f^2}\,, \tag{4.79}$$

in the form

$$\kappa_{\mathrm{e}} = \underbrace{\frac{\overline{v'^2}}{\mu + \mu_c}}_{\kappa_v}\underbrace{\frac{1}{1 + c_R^2 p_f^2/(\mu + \mu_c)^2}}_{S}\,. \tag{4.80}$$

If $\mu = \mu_c$ the expression above has the same form as the anisotropic-ring diffusivity in (4.69); if $\mu_c = 0$ the expression in (4.77) is identical to equation (20) in *Klocker et al.* [2012]. Further, in the limit of $\beta \to \infty$, the general result $\kappa_{\mathrm{e}} \propto \beta^{-2}$ in (4.72) is recovered by using $\overline{\zeta'^2} = \varepsilon k_f^2/\mu$.

There are two important remarks to make about (4.80). First, and intuitively, it is $\overline{v'^2}$, rather than the eddy kinetic energy, that determines the unsuppressed eddy diffusivity. Second, it is the intrinsic Rossby wave speed, proportional to the base state potential vorticity gradient, that appears in the suppression factor. In the model of *Klocker et al.* [2012] the intrinsic zonal phase speed is

$$c_R = -\frac{\beta + UL_d^{-2}}{k_f^2 + L_d^{-2}}\,, \tag{4.81}$$

where U is the background mean flow in the upper layer of their equivalent barotropic model (the lower layer is quiescent) and L_d is the deformation length. Because the potential vorticity gradient, $\beta + UL_d^{-2}$, is modified by the background mean flow, strong mean flow increases c_R and therefore suppresses κ_{e}. By comparison in (4.78), our c_R does not depend on a background mean flow. In both models it is the meridional potential vorticity gradient, β in (4.78) and $\beta + UL_d^{-2}$ in (4.81), that enables eddies to move relative to the mean flow, results in a non-zero $c_R = c - U$, and the associated suppression of κ_{e}. (Note that the Doppler-shifted phase speed c is the *observed* zonal speed of eddies, as seen, for example, in satellite altimetry.)

4.6.5 The case $\beta = 0$

With $\beta = 0$ we evaluate the integrals for κ_{e} in (4.57) and (4.58) numerically. Figure 4.6(a) shows the diffusivity $\kappa_{\mathrm{e}}(\alpha, 0, \gamma, \mu)$ as a function of the shear γ/μ. In Figure 4.6(b) we express the diffusivity in terms of the suppression factor S in (4.63). The three curves are much closer together in (b) than in (a) and therefore the variation in κ_{e} with α_c and γ/μ is due mainly to variation in $\overline{v'^2}$.

The case $\alpha = -1$ in Figure 4.6(b) shows a slight enhancement of κ_{e} above κ_v. Thus, in some cases at least, shear can enhance eddy diffusivity, so that S is slightly greater than 1. This weak effect is due to the Kelvin-Orr mechanism: $\alpha = -1$ loads the forcing variance deep in the Farrell & Ioannou's (1993) favorable sector of the wavenumber plane. The diffusivity in (4.57) through (4.59) is given by a weighted time-integral of the v'^2 associated with a sheared wave. Apparently this time integral is not necessarily bounded above κ_v (though it is by $2\kappa_v$).

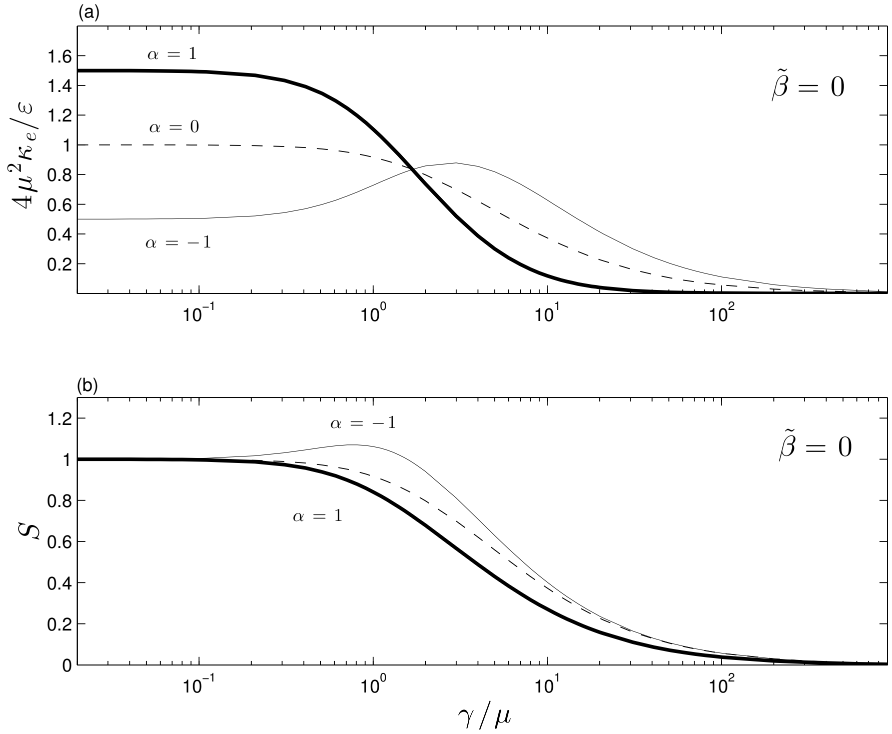

Figure 4.6: (a) The non-dimensional tracer diffusivity as a function of γ/μ with β=0 and different values of α. (b) The corresponding suppression factor defined in (4.63).

4.6.6 Large shear

When $\tilde{\gamma} \gg 1$, and provided $\tilde{\gamma} \gg \tilde{\beta}$, the kernel $\tilde{M}$ in (4.58) is concentrated near $\phi = \pi/2$ and the integrals can be evaluated approximately (see Appendix E). In this large-shear limit the eddy diffusivity is

$$\kappa_{\mathrm{e}}(\alpha, \beta, \gamma \to \infty, \mu) \approx (1 - \alpha_c)\frac{\pi\varepsilon}{2\gamma\mu}\, B_1(\pi\tilde{\beta})\,, \tag{4.82}$$

where the function B_1 is

$$B_1(b) \overset{\mathrm{def}}{=} b^{-2}\left[\pi b - 2b\,\arctan\frac{1}{b} - \ln(1+b^2)\right]\,. \tag{4.83}$$

Figure 4.7(a) shows the variation of the function $B_1(\pi\tilde{\beta})$ with $\tilde{\beta}$ while Figure 4.7(b) shows that the approximate expression in (4.82) is in good agreement with numerical computation of κ_{e} using (4.57).

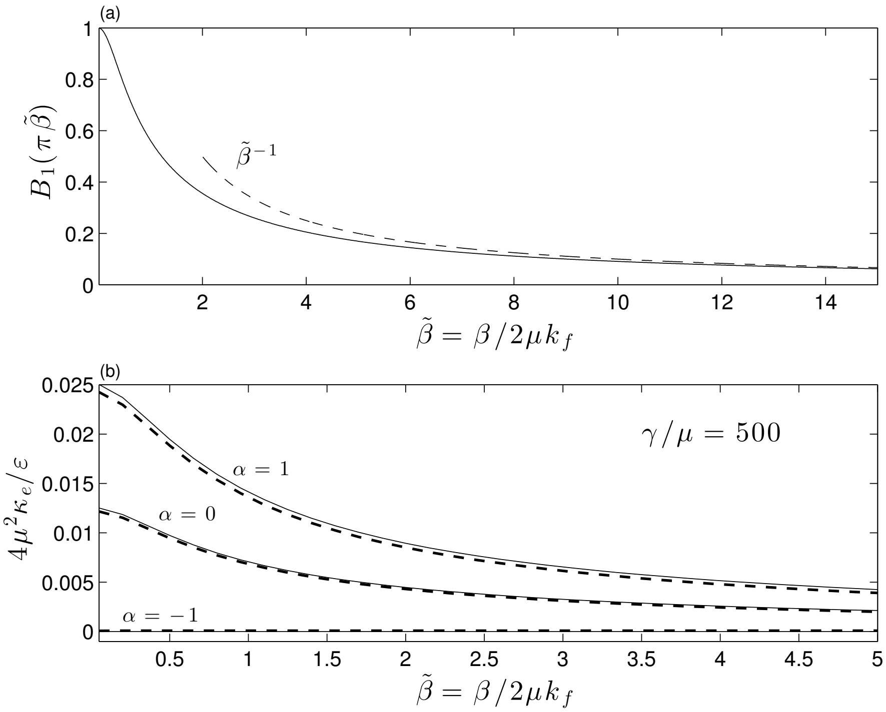

Figure 4.7: (a) The function $B_1(\pi\tilde{\beta})$ given in (4.83) shown as a function of $\tilde{\beta}$. The large $\tilde{\beta}$ approximation is the dashed curve. (b) A comparison of the numerically computed non-dimensional tracer diffusivity for γ/μ=500 (dashed curve) with the approximate expression in (4.82) (solid curve).

In the limit of large shear, the meridional velocity variance in (4.49), becomes

$$\overline{v'^2} = \frac{\varepsilon}{2\mu}(1-\alpha) + O(\tilde{\gamma}^{-1})\,, \tag{4.84}$$

and can be used to rewrite the eddy diffusivity in terms of the suppression factor S in the form

$$\kappa_{\mathrm{e}}(\alpha,\beta,\gamma\to\infty,\mu) \approx \kappa_v\ \underbrace{\frac{2\pi}{\tilde{\gamma}}B_1(\pi\tilde{\beta})}_{S}\ . \tag{4.85}$$

This result leads to two important conclusions: first that $S \propto \gamma^{-1}$ i.e., large shear suppresses eddy diffusivity and in the large-shear limit the γ^{-1} dependence is the same as the earlier result for the Reynolds stress in (4.44). Second, the effect of anisotropy on the diffusivity is completely included in the meridional velocity variance $\overline{v'^2}$, so that S is independent of α. Limiting forms of the suppression

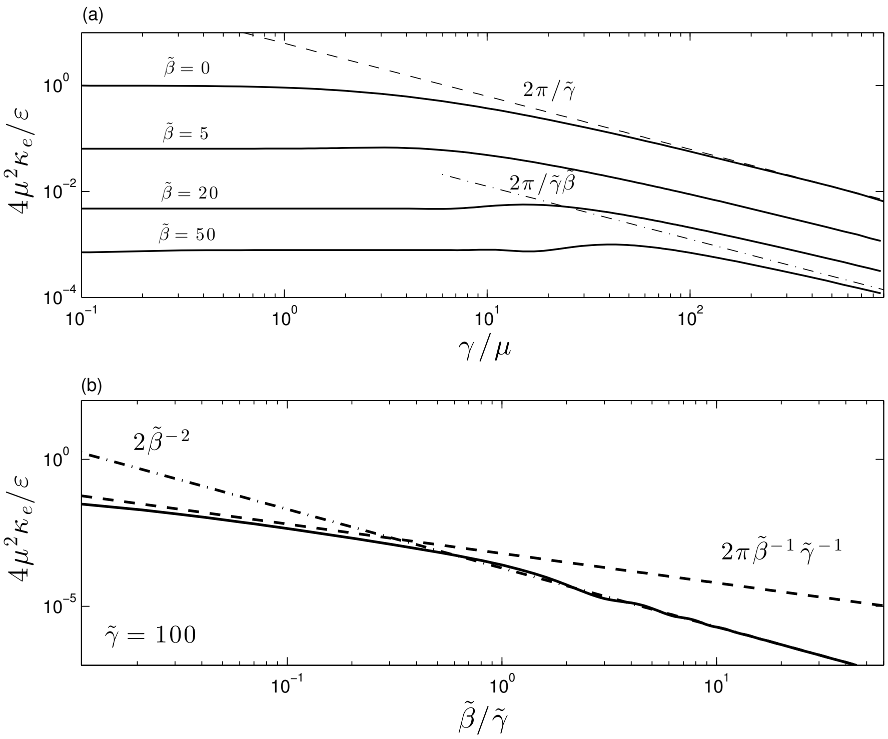

Figure 4.8: (a) The numerically computed non-dimensional tracer diffusivity as a function of γ/μ, with different values of β, and isotropic forcing $\alpha = 0$. Also plotted are the large γ asymptotes for $\tilde\beta = 0$ (dashed line) and $\tilde\beta = 50$ (dot-dashed line) in (4.86). (b) Comparison of the numerically computed non-dimensional κ_{e} for $\tilde\gamma = 100$ (solid line) as a function of $\tilde\beta/\tilde\gamma$, with asymptotes corresponding to the limits $\tilde\beta \gg \tilde\gamma \gg 1$ (dot-dashed line) and $\tilde\gamma \gg \tilde\beta \gg 1$ (dashed line).

factor in (4.85) for large and small $\tilde\beta$ can be inferred from Figure 4.7 (a) as

$$S \approx \begin{cases} \dfrac{2\pi}{\tilde\gamma} & \text{if } \tilde\beta \to 0\,, \\[2em] \dfrac{2\pi}{\tilde\gamma\tilde\beta} & \text{if } \tilde\gamma \gg \tilde\beta \gg 1\,. \end{cases} \tag{4.86}$$

Figure 4.8 (a) shows comparisons of the numerically computed diffusivity integral in (4.57) for isotropic forcing ($\alpha = 0$), with the asymptotic forms displayed in (4.86).

Finally, we note that in the limit $\tilde\beta \gg \tilde\gamma \gg 1$, the general result of (4.72) is recovered, i.e.

$$\kappa_{\mathrm{e}} = \kappa_\zeta \quad \text{if } \tilde{\beta} \gg \tilde{\gamma} \gg 1\,. \tag{4.87}$$

In Figure 4.8 (b), the normalized eddy diffusivity is plotted as a function of $\tilde{\beta}/\tilde{\gamma}$ for a large value of the shear, $\tilde{\gamma} = 100$. It is clear that when $\tilde{\beta}/\tilde{\gamma}$ is small, the diffusivity asymptotes to the lower result in (4.86), and to (4.87) (written in the equivalent form, (4.71)) for large values of $\tilde{\beta}/\tilde{\gamma}$.

4.7 Discussion and conclusion

The model (4.1) and (4.2) has a special status as an analytically tractable example whose solution sheds light on eddy transport of momentum, vorticity and tracer. To be sure, the model is linear and, unless one has strong faith in stochastic turbulence models, the results might therefore apply only in the case of weak, externally forced, eddies on a strong mean flow.

Key results for (4.1) and (4.2) detailed in this paper emphasize the dependence of the statistical properties of the solutions of linear vorticity equation (4.1) and the scalar equation (4.2) on the spatial structure of the forcing, ξ, and the shear, γ. However, the role of β is peculiar: a great and unexpected simplification is that the eddy kinetic energy level and the Reynolds stress, σ, are independent of β. But σ is a non-linear and non-monotonic function of the γ. Thus, while it is sensible to define an eddy diffusivity according to (4.4), one cannot define an analogous eddy viscosity because σ is not linearly proportional to γ. Thus our result for σ in (4.41) provides an explicit analytic example of *Dritschel and McIntyre* [2010]'s "anti-friction" (as opposed to negative eddy viscosity).

The spatial structure of the stochastic forcing, ξ, is characterized by the anisotropy parameter α in (4.19). The Reynolds stress is found to be directly proportional to α, so "frictional" and "anti-frictional" stresses are obtained when α is negative and positive, respectively. And if the forcing is isotropic then the Reynolds stress is identically zero. When the background shear, γ is weak, the Reynolds stress is proportional to γ. Thus, in this special case, one can identify an effective viscosity, ν_{e}, whose sign is opposite to that of α. The expression for ν_{e}

in (4.43) connects with a similar result obtained by Bakas and Ioannou (2013) for a forcing function resembling our $\alpha = 1$: in this case $\nu_{\mathrm{e}} < 0$.

In general, the most important determinants of the tracer eddy diffusivity, κ_{e}, are the meridional kinetic energy, $\overline{v'^2}$, and the drag μ. With $\beta = \gamma = 0$, the diffusivity is precisely $\overline{v'^2}/(2\mu)$. But typically, κ_{e} is smaller than $\overline{v'^2}/(2\mu)$ whenever β or γ are non-zero. In other words, both γ and β suppress eddy diffusivity. If $\gamma = 0$ the suppression due to β is a consequence of propagation of Rossby waves relative to a background mean flow. The suppression of diffusivity due to β (or more generally, any background potential vorticity gradient) has been discussed previously by *Klocker et al.* [2012], and their results can be interpreted as a special case of ours with $\gamma = 0$. Strong shear also causes the diffusivity to decrease as γ^{-1}, and this inverse proportionality mirrors the γ^{-1} variation of the Reynolds stress for large γ.

We caution against summarizing the results above by saying that "mean flow suppresses eddy diffusivity". The mean flow is γy and "mean flow suppression" invites the incorrect conclusion that κ_{e} would decrease as $|y|$ increases. Instead, fundamentally because of the Galiliean invariance in section 4.3, κ_{e} is independent of y. The "mean-flow suppression" explained in *Klocker et al.* [2012] and *Ferrari and Nikurashin* [2010] is caused by the relative motion of eddies with respect to the mean flow. However, this relative motion is due to a non-zero potential vorticity gradient, which in the case of *Klocker et al.* [2012] includes both β and a term resulting from the *baroclinic* shear of the mean flow. If a barotropic mean flow $U(y)$ has $U_{yy} \neq 0$ then the background potential vorticity gradient is modified to $\beta - U_{yy}$, and it is this total gradient (rather than just β) that is relevant for eddy suppression. Thus it is not the mean flow directly, but rather the contribution of the mean flow to the PV gradient that results in suppression of diffusivity.

We close by remarking that our results bear on the historical controversy between Prandtl's theory of momentum transfer and Taylor's theory based on vorticity transfer. The debate migrated into geophysical fluid dynamics in the seventies [*Welander*, 1973; *Thomson and Stewart*, 1977; *Stewart and Thomson*, 1977] and has recently been recalled by *Maddison and Marshall* [2013]. The results here do not support Taylor's view. Taylor argued that in ideal two-dimensional fluid dynamics, vorticity should be transferred much like a passive scalar and thus advocated an eddy closure which, in our notation, is

$$\overline{v'\zeta'} = -\kappa_{\mathrm{e}}\beta \, . \tag{4.88}$$

A prominent problem with this proposal has always been that because of the identity (4.23) momentum is not conserved on a β-plane. Our results pile on more: although the passive scalar eddy diffusivity κ_{e} is non-zero, the vorticity flux on the left of (4.88) is zero. Moreover, in general agreement with Prandtl's views, there is a non-zero momentum flux which is, painfully for Taylor, independent of mean potential vorticity gradient, β. Thus, in the model solved here, β is an important control on passive-scalar transport, but it is irrelevant for momentum transport.

4.A A bound on eddy diffusivity

In addition to the definition in (4.4), the eddy diffusivity can be obtained from the power integrals in (4.28) and (4.29). Thus we can write the eddy diffusivity as a linear combination of three different expressions:

$$\kappa_{\mathrm{e}} = p \, \frac{\mu \, \overline{c'^2}}{\beta \beta_c} + 2q \, \frac{\mu \, \overline{\zeta' c'}}{\beta \beta_c} - r \, \frac{\overline{v' c'}}{\beta_c} \, , \tag{4.89}$$

where $p+q+r=1$. Completing the square involving c', assuming that $p<0$, and then dropping the squared term (which has the same sign as p) gives the inequality

$$\kappa_{\mathrm{e}} \le \frac{1}{2} \frac{q^2 \kappa_\zeta + r^2 \kappa_v}{q+r-1} \, , \tag{4.90}$$

where κ_v and κ_ζ are defined in (4.33) and (4.35). Minimizing the right hand side of (4.90) over q and r we find

$$q = \frac{2\kappa_v}{\kappa_v + \kappa_\zeta} \, , \qquad r = \frac{2\kappa_\zeta}{\kappa_v + \kappa_\zeta} \, , \tag{4.91}$$

and therefore $p=-1$. The smallest value of the right hand side of (4.90) produces the best upper bound on κ_{e}, which is the result in (4.36).

4.B Details of the $\mathcal{Z}$ solution

Using the convention in (4.12), the Fourier transform of (4.38) is

$$-\gamma p \tilde{\mathcal{Z}}_q = \tilde{\Xi} - 2\mu \tilde{\mathcal{Z}} \,. \tag{4.92}$$

The solution of the ordinary differential equation (4.92) can be written as the time integral of a "sheared disturbance":

$$\tilde{\mathcal{Z}}(p, q) = \int_0^\infty \mathrm{e}^{-2\mu t}\, \tilde{\Xi}(p, \hat{q})\, \mathrm{d}t \,, \tag{4.93}$$

where

$$\hat{q} \overset{\text{def}}{=} q + p\gamma t \,. \tag{4.94}$$

4.B.1 A polar representation of $\tilde{\Xi}$

It is convenient to use a polar representation of the spectrum:

$$\tilde{\Xi} = \tilde{\Xi}_0(k) + \sum_{n=1}^{\infty} \tilde{\Xi}_{2n}(k) \cos 2n\phi; \tag{4.95}$$

above $p = k\cos\phi$ and $q = k\sin\phi$. The anisotropic ring forcing in (4.12) has this form. Because of the exchange symmetry (4.11), only even terms appear within the sum on the right of (4.95). And because of the assumed reflexion symmetry in (4.15) there are no $\sin 2n\phi$ terms in (4.95).

4.B.2 The Reynolds stress

In wavenumber space, the Reynolds stress in (4.40) is

$$\overline{u'v'} = -\iint \frac{pq\, \tilde{\mathcal{Z}}(p, q)}{(p^2 + q^2)^2} \frac{\mathrm{d}p\mathrm{d}q}{(2\pi)^2} \,. \tag{4.96}$$

Combining (4.93) and (4.96) we obtain

$$\gamma \overline{u'v'} = \varepsilon - \mu \iint J_1(p, q)\, \tilde{\Xi}(p, q)\, \frac{\mathrm{d}p\mathrm{d}q}{(2\pi)^2} \,, \tag{4.97}$$

where the kernel is

$$J_1(p, q) \overset{\text{def}}{=} \int_0^\infty \frac{\mathrm{e}^{-2\mu t}}{p^2 + (q - p\gamma t)^2}\, \mathrm{d}t \,. \tag{4.98}$$

The three terms in (4.97) correspond to the three terms in the energy power integral (4.26).

Substituting the Fourier series expansion of $\tilde{\Xi}(p,q)$ in (4.95) into (4.97), and performing the ϕ-integrals using (4.107) below, one finds

$$\overline{u'v'} = \frac{\mu}{\gamma^2}\sum_{n=1}^{\infty}(-1)^{n+1}\mathcal{T}_{2n}\int_0^{\infty}\frac{\tilde{\Xi}_{2n}(k)}{2\pi k}\,\mathrm{d}k\,. \tag{4.99}$$

The coefficients in (4.99) are

$$\mathcal{T}_{2n} = \int_0^{\infty}\mathrm{e}^{-m\tau/2}\left[\frac{\tau}{\sqrt{\tau^2+4}}\right]^n \mathrm{T}_n\left(\frac{\tau}{\sqrt{\tau^2+4}}\right)\mathrm{d}\tau\,, \tag{4.100}$$

where $m \overset{\text{def}}{=} 4\mu/\gamma$ and T_n is the Chebyshev polynomial of order n.

When the forcing $\tilde{\Xi}$ is specialized to the anisotropic ring spectrum in (4.20), only the $n = 1$ term in (4.99) is non-zero, and the k-integral is trivial. The expression for $\overline{u'v'}$ in (4.41) is obtained from (4.100) with $n = 1$.

Notice that the isotropic part of the spectrum i.e., $\tilde{\Xi}_0(k)$ in (4.95), does not contribute to the Reynolds stresses in (4.99). This recapitulates the result that isotropic forcing of a Couette flow does not produce Reynolds stresses [*Farrell and Ioannou*, 1993b; *Srinivasan and Young*, 2012].

4.B.3 Anisotropy

We first compute $\overline{v'^2}$ starting from

$$\overline{v'^2} = \iint \frac{p^2\,\tilde{\mathcal{Z}}(p,q)}{(p^2+q^2)^2}\,\frac{\mathrm{d}p\mathrm{d}q}{(2\pi)^2}\,. \tag{4.101}$$

Combining (4.93) and (4.101), we have

$$\overline{v'^2} = \iint J_2(p,q)\,\tilde{\Xi}(p,q)\,\frac{\mathrm{d}p\mathrm{d}q}{(2\pi)^2}\,, \tag{4.102}$$

where the kernel is,

$$J_2(p,q) \overset{\text{def}}{=} \int_0^{\infty}\frac{p^2\mathrm{e}^{-2\mu t}}{[p^2+(q-p\gamma t)^2]^2}\,\mathrm{d}t\,. \tag{4.103}$$

Owing to the complexity of the kernel $J_2(p, q)$, we compute $\overline{v'^2}$ only for the special case of the anisotropic ring spectrum in (4.20). On combining with (4.102) and evaluating the angular integral as a special case of (4.108) gives

$$\overline{v'^2} = \frac{\varepsilon}{2\mu}\left[1 + 2\alpha_c \int_0^\infty \mathrm{e}^{-\tau} B\left(\frac{\gamma\tau}{2\mu}\right) \mathrm{d}\tau\right] . \tag{4.104}$$

where the function B is defined in (4.111). Using $\overline{v'^2} - \overline{u'^2} = 2\overline{v'^2} - (\overline{u'^2} + \overline{v'^2})$, and the expression for the eddy kinetic energy in (4.48), we obtain $\overline{v'^2} - \overline{u'^2}$ in (4.53).

4.B.4 Two angular integrals

Although the Fourier integral

$$A_n(t) \overset{\text{def}}{=} \oint \frac{\mathrm{e}^{2in\phi}}{\cos^2\phi + (\sin\phi - t\cos\phi)^2} \frac{\mathrm{d}\phi}{2\pi} \tag{4.105}$$

defeats Mathematica, $A_n(t)$ can be evaluated using the method of residues:

$$A_n(t) = \left[-\frac{t(t-2\mathrm{i})}{t^2+4}\right]^n , \qquad (n = 0,\ 1,\ 2, \cdots) \tag{4.106}$$

If $n \geq 1$, real and imaginary parts of (4.106) are separated as

$$\begin{aligned} A_n(t) = (-1)^n \left(\frac{t}{\sqrt{t^2+4}}\right)^n \Bigg[&\mathrm{T}_n\left(\frac{t}{\sqrt{t^2+4}}\right) \\ &- \frac{2\mathrm{i}}{\sqrt{t^2+4}} \mathrm{U}_{n-1}\left(\frac{t}{\sqrt{t^2+4}}\right)\Bigg] , \end{aligned} \tag{4.107}$$

where T_n is the Chebyshev polynomial of order n and U_{n-1} is the modified Chebyshev polynomial.

An integral required for the evaluation of $\overline{v'^2}$ is

$$B_n(t) \overset{\text{def}}{=} \oint \frac{\cos^2\phi\, \mathrm{e}^{2in\phi}}{[\cos^2\phi + (\sin\phi - t\cos\phi)^2]^2} \frac{\mathrm{d}\phi}{2\pi} . \tag{4.108}$$

The method of residues gives

$$B_0(t) = \frac{1}{2} , \tag{4.109}$$

and

$$B_n(t) = -\left[-\frac{t(t-2\mathrm{i})}{t^2+4}\right]^n \left[\frac{1}{2} + \frac{n}{t(t+2i)}\right] , \tag{4.110}$$

where $n = 1,\ 2, \cdots$ Although (4.110) can be separated into real and imaginary parts along the lines of (4.107), the resulting expression is long and is not stated here. Instead, for the special case of $n = 1$, we have

$$B(t) \overset{\text{def}}{=} \Re B_1(t) = \frac{8}{(t^2+4)^2} - \frac{t^2}{4(t^2+4)} - \frac{1}{4}\,. \tag{4.111}$$

4.C Properties of F_1 and F_2

The functions F_1 in (4.42) and F_2 in (4.50) can be written compactly in terms of the exponential integral

$$\mathrm{E}(z) \overset{\text{def}}{=} \int_z^\infty \frac{\mathrm{e}^{-u}}{u}\,\mathrm{d}u\,, \tag{4.112}$$

and the parameter $m \overset{\text{def}}{=} 4\mu/\gamma$, as

$$F_1 = m + m^2 \Im \mathrm{e}^{\mathrm{i}m}\mathrm{E}(\mathrm{i}m)\,, \tag{4.113}$$

$$F_2 = m^2 \Re \mathrm{e}^{\mathrm{i}m}\mathrm{E}(\mathrm{i}m) \tag{4.114}$$

Standard properties of the exponential integral can then be used to deduce the dependence of $\overline{u'v'}$ on the non-dimensional shear γ/μ in various limits.

4.D Details of the solution for κ_e

It is convenient to use the tracer-vorticity correlation function

$$H \overset{\text{def}}{=} \overline{\zeta_1 c_2} = \nabla^2 P\,. \tag{4.115}$$

In terms of H, the Fourier transform of (4.54) is

$$-\gamma p \tilde{H}_q + (\mathrm{i}\omega + 2\mu)\,\tilde{H} = \mathrm{i}\frac{\beta_c}{\beta}\omega\tilde{\mathcal{Z}}\,, \tag{4.116}$$

where

$$\omega(p,q) \overset{\text{def}}{=} -\frac{\beta p}{p^2+q^2} \tag{4.117}$$

is the Rossby wave frequency. Using the method of characteristics, the solution of (4.116) is

$$\tilde{H}(p,q) = \mathrm{i}\frac{\beta_c}{\beta}\int_0^\infty \tilde{Z}(p,\hat{q})\omega(p,\hat{q})\mathrm{e}^{-2\mu t - \mathrm{i}\eta(p,q,t)}\,\mathrm{d}t\,, \tag{4.118}$$

where $\hat{q} \overset{\mathrm{def}}{=} q + p\gamma t$ and

$$\eta(p, q, t) \overset{\mathrm{def}}{=} \int_0^t \omega(p, q + p\gamma t')\, \mathrm{d}t' \,. \tag{4.119}$$

Noting that $\omega(p, \hat{q}) = \partial_t \eta$, one can integrate by parts in (4.118) and obtain a simpler expression for $\tilde{H}$:

$$\tilde{H}(p, q) = \frac{\beta_c}{\beta} \left[\tilde{Z}(p, q) - \int_0^\infty \mathrm{e}^{-2\mu t - \mathrm{i}\eta}\, \tilde{\Xi}(p, \hat{q})\, \mathrm{d}t \right] . \tag{4.120}$$

To calculate the eddy diffusivity in (4.125) below one needs the integral of $\tilde{H}$ in (4.120) over the wavenumbers p and q. The ensuing triple integral is disentangled by changing variables in the wavenumber integrals from (p, q) to $\hat{p} = p$ and $\hat{q} = q + p\gamma t$. One finds

$$\iint \tilde{H}(p, q)\, \frac{\mathrm{d}p\mathrm{d}q}{(2\pi)^2} = \frac{\beta_c}{\beta} \left[\overline{\zeta'^2} - \iint \tilde{K}(p, q)\, \tilde{\Xi}(p, q) \frac{\mathrm{d}p\mathrm{d}q}{(2\pi)^2} \right] , \tag{4.121}$$

where $\tilde{K}(p, q) = \tilde{K}_r(p, q) + \mathrm{i}\tilde{K}_i(p, q)$ is the kernel

$$\tilde{K}(p, q) \overset{\mathrm{def}}{=} \int_0^\infty \mathrm{e}^{-2\mu t - \mathrm{i}\chi(p,q,t)}\, \mathrm{d}t \,, \tag{4.122}$$

with

$$\chi(p, q, t) \overset{\mathrm{def}}{=} \int_0^t \omega(p, q - p\gamma t')\, \mathrm{d}t' \,. \tag{4.123}$$

The phase χ is evaluated explicitly in (4.59). The kernel in (4.122) has the symmetry

$$\tilde{K}(p, q) = \tilde{K}^*(-p, -q) \,, \tag{4.124}$$

which shows that $\tilde{K}$ is the Fourier transform of a real function.

Our main goal is to calculate the tracer eddy diffusivity κ_e in (4.4). Using the power integral (4.29) this is

$$\kappa_\mathrm{e} = \frac{2\mu}{\beta\beta_c} \iint \tilde{H}_r(p, q)\, \frac{\mathrm{d}p\mathrm{d}q}{(2\pi)^2} \,, \tag{4.125}$$

where $\tilde{H}_r$ is the real part of $\tilde{H}$. Taking the real part of (4.121) we obtain from (4.125)

$$\kappa_\mathrm{e} = \frac{2\mu\overline{\zeta'^2}}{\beta^2} - \frac{2\mu}{\beta^2} \iint \tilde{K}_r(p, q)\tilde{\Xi}(p, q)\, \frac{\mathrm{d}p\mathrm{d}q}{(2\pi)^2} \,. \tag{4.126}$$

Using

$$\overline{\zeta'^2} = \iint \frac{\tilde{\Xi}(p, q)}{2\mu}\, \frac{\mathrm{d}p\mathrm{d}q}{(2\pi)^2} \tag{4.127}$$

the result in (4.126) is rewritten in (4.57).

4.E Tracer diffusivity in the limit $\gamma/\mu \to \infty$

Using the exchange symmetry we can perform the p and q integrals in (4.57) over the right half plane $p > 0$, and then multiply by two. In polar coordinates, we therefore limit attention to $-\pi/2 < \phi < \pi/2$, so that the $\arctan(q/p) = \phi$. As $\gamma/\mu \to \infty$ and $\tilde{\gamma} \gg \tilde{\beta}$, the kernel $\tilde{M}$ in (4.58) becomes increasingly concentrated close to $\phi = \pi/2$. Indeed, in the distinguished limit $\gamma/\mu \to \infty$, with

$$t_* \overset{\text{def}}{=} \frac{1}{\gamma\left(\frac{\pi}{2} - \phi\right)} \tag{4.128}$$

fixed and order unity, the phase function in (4.59) simplifies to

$$\chi \approx -\frac{\beta t_*}{k}\left(\frac{\pi}{2} + \arctan\gamma(t - t_*)\right) . \tag{4.129}$$

Moreover, as γ becomes large, the arctangent above approaches a discontinuous step function with a jump at $t = t_*$. In this limit the function $\cos\chi(t)$ in (4.58) is constant on either side of the jump at t_*. This observations enables one to easily perform the integral in (4.59) with the result

$$\tilde{M}(k, \phi) \approx \mathrm{e}^{-2\mu t_*}\left[1 - \cos\left(\frac{\pi\beta t_*}{k}\right)\right] . \tag{4.130}$$

The errors are probably $O(\gamma^{-1})$.

Using the anisotropic ring forcing in (4.19), we have therefore

$$\kappa_{\mathrm{e}} \approx \frac{2k_f^2\varepsilon}{\pi\beta^2}\int_{-\pi/2}^{\pi/2}\tilde{M}(k_f, \phi)\left(1 + \alpha_c\cos 2\phi\right)\,\mathrm{d}\phi\,. \tag{4.131}$$

The main contribution comes from the neighborhood of $\phi = \pi/2$, and after some approximations and transformations

$$\kappa_{\mathrm{e}} \approx (1 - \alpha_c)\frac{2k_f^2\varepsilon}{\pi\beta^2}\int_0^\infty \mathrm{e}^{-2\mu v/\gamma}\left[1 - \cos\left(\frac{\pi\beta v}{k_f\gamma}\right)\right]\frac{\mathrm{d}v}{v^2}\,. \tag{4.132}$$

The integral above can be evaluated exactly:

$$\begin{aligned}&\int_0^\infty \mathrm{e}^{-nx}\left(1 - \cos mx\right)\frac{\mathrm{d}x}{x^2}\\ &\qquad = \frac{m}{2}\left[\pi - 2\arctan\frac{n}{m} - \frac{n}{m}\ln\left(1 + \frac{m^2}{n^2}\right)\right]\end{aligned} \tag{4.133}$$

The result for κ_{e} is (4.69).

Chapter 4 has been accepted for publication in the *Journal of Atmospheric Sciences*. The dissertation author was the primary investigator and author of this material. W.R. Young directed and supervised this research.

References

Arbic, B. K., and G. R. Flierl, Effects of mean flow direction on energy, isotropy, and coherence of baroclinically unstable beta-plane geostrophic turbulence., *J. Phys. Oceanogr.*, *34*, 77–93, 2004.

Aurnou, J., M. Heimpel, and J. Wicht, The effects of vigorous mixing in a convective model of zonal flow on the ice giants, *Icarus*, *190*(1), 110–126, 2007.

Bakas, N. A., and P. J. Ioannou, Structural stability theory of two-dimensional fluid flow under stochastic forcing, *J. Fluid Mech.*, *682*, 332–261, 2011.

Bakas, N. A., and P. J. Ioannou, On the mechanism underlying the spontaneous generation of barotropic zonal jets, *J. Atmos. Sci.*, *70*, 22512271, 2013.

Beebe, R. F., Comparative study of the dynamics of the outer planets, *Space science reviews*, *116*(1-2), 137–154, 2005.

Berloff, P., I. Kamenkovich, and J. Pedlosky, A mechanism of formation of multiple zonal jets in the oceans, *J. Fluid Mech.*, *628*, 395–425, 2009.

Boland, E. J., A. F. Thompson, E. Shuckburgh, and P. H. Haynes, The formation of nonzonal jets over sloped topography, *J. Phys. Oceanogr.*, *42*(10), 1635–1651, 2012.

Boyd, J. P., The continuous spectrum of linear Couette flow with the beta effect, *J. Atmos. Sci.*, *40*, 2304–2308, 1983.

Carnevale, G. F., and P. C. Martin, Field theoretical techniques in statistical fluid dynamics: with applications to nonlinear wave dynamics, *Geophys. Astrophys. Fluid Dynamics*, *20*, 131–164, 1982.

Chan, C. J., R. A. Plumb, and I. Cerovecki, Annular modes in a multiple migrating zonal jet regime, *J. Atmos. Sci.*, *64*(11), 4053–4068, 2007.

Chen, C., and I. Kamenkovich, Effects of topography on baroclinic instability, *J. Phys. Oceanogr.*, *43*(4), 790–804, 2013.

Constantinou, N. C., P. J. Ioannou, and B. F. Farrell, Emergence and equilibration of jets in beta-plane turbulence, *arXiv preprint arXiv:1208.5665*, 2012.

Cox, S. M., and P. C. Matthews, Exponential time differencing for stiff systems, *J. Comp. Phys.*, *176*, 430–455, 2005.

Cummins, P. F., and G. Holloway, Reynolds stress and eddy viscosity in direct numerical simulation of sheared-two-dimensional turbulence, *J. Fluid Mech.*, *657*, 394–412, 2010.

Danilov, S., and V. M. Gryanik, Barotropic beta-plane turbulence in a regime with strong zonal jets revisited, *J. Atmos. Sci.*, *61*, 2283–2295, 2004.

Danilov, S., and D. Gurarie, Scaling, spectra and zonal jets in beta-plane turbulence, *Phys. Fluids*, *16*, 2592–2603, 2004.

DelSole, T., A theory for the forcing and dissipation in stochastic turbulence models, *J. Atmos. Sci.*, *58*, 3762–3775, 2001.

Diamond, P. H., S.-I. Itoh, K. Itoh, and T. S. Hahm, Zonal flows in plasmas — a review, *Plasma Physics and Controlled Fusion.*, *47*, R35–R161, 2005.

Dritschel, D. G., and M. E. McIntyre, Multiple jets as pv staircases: the phillips effect and the resilience of eddy-transport barriers, *J. Atmos. Sci.*, *65*, 855–874, 2010.

Farrell, B. F., The initial growth of disturbances in a baroclinic flow, *J. Atmos. Sci.*, *39*(8), 1663–1686, 1982.

Farrell, B. F., and P. J. Ioannou, Stochastic forcing of the linearized Navier-Stokes equations, *Phys. Fluids A*, *5*, 2600–2609, 1993a.

Farrell, B. F., and P. J. Ioannou, Stochastic forcing of perturbation variance in unbounded shear and deformation flows, *J. Atmos. Sci.*, *50*, 200–211, 1993b.

Farrell, B. F., and P. J. Ioannou, Structural stability of turbulent jets, *J. Atmos. Sci.*, *50*, 2101–2118, 2003.

Farrell, B. F., and P. J. Ioannou, Structure and spacing of jets in barotropic turbulence, *J. Atmos. Sci.*, *64*, 3652–3665, 2007.

Ferrari, R., and M. Nikurashin, Suppression of eddy diffusivity across jets in the Southern Ocean, *J. Phys. Oceanogr.*, *40*, 1501–1519, 2010.

Ferrari, R., and C. Wunsch, The distribution of eddy kinetic and potential energies in the global ocean, *Tellus A*, *62*(2), 92–108, 2010.

Galperin, B., H. Nakano, H.-P. Huang, and S. Sukoriansky, The ubiquitous zonal jets in the atmospheres of giant planets and earth's oceans, *Geophysical research letters*, *31*(13), L13,303, 2004.

Galperin, B., S. Sukoriansky, N. Dikovskaya, P. L. Read, Y. H. Yamazaki, and R. Wordsworth, Anisotropic turbulence and zonal jets in rotating flows with a β-effect, *Nonlinear Processes in Geophysics*, *13*, 1–16, 2006.

Gierasch, P., et al., Observation of moist convection in Jupiter's atmosphere, *Nature*, *403*(6770), 628–630, 2000.

Hartmann, D. L., The atmospheric general circulation and its variability, *Journal of the Meteorological Society of Japan. Ser. II*, *85B*, 123–143, 2007.

Heimpel, M., J. Aurnou, and J. Wicht, Simulation of equatorial and high-latitude jets on Jupiter in a deep convection model, *Nature*, *438*(7065), 193–196, 2005.

Held, I., The general circulation of the atmosphere, paper presented at 2000 Woods Hole Oceanographic institute Geophysical Fluid Dynamics Program, Woods Hole Oceanographic Institute, Woods Hole, MA, *Woods Hole Oceanogr. Inst., Woods Hole, Mass.(Available at http://gfd. whoi. edu/proceedings/2000/PDFvol2000. html)*, 2000.

Holloway, G., Eddy stress and shear in 2d flows, *J. Turbulence*, *11*, 1–14, 2010.

Huang, H. P., and W. A. Robinson, Two-dimensional turbulence and persistent zonal jets in a global barotropic model, *Nonlinear Processes in Geophysics*, *55*, 611–632, 1998.

Kaspi, Y., A. P. Showman, W. B. Hubbard, O. Aharonson, and R. Helled, Atmospheric confinement of jet streams on Uranus and Neptune, *Nature*, *497*(7449), 344–347, 2013.

Kelvin, L., Stability of fluid motion: rectilinear motion of viscous fluid between two parallel plates, *Phil. Mag*, *24*(5), 188–196, 1887.

Klocker, A., R. Ferrari, and J. H. LaCasce, Estimating suppression of eddy mixing by mean flows, *J. Phys. Oceanogr.*, *42*, 1566–1576, 2012.

Kraichnan, R. H., Inertial ranges in two-dimensional turbulence, *Physics of fluids*, *10*(7), 1417–1423, 1967.

Kraichnan, R. H., Eddy viscosity in two and three-dimensional turbulence, *J. Atmos. Sci.*, *33*, 1521–1536, 1976.

Li, L., A. P. Ingersoll, and X. Huang, Interaction of moist convection with zonal jets on Jupiter and Saturn, *Icarus*, *180*, 113–123, 2006.

Lilly, D. K., Numerical simulation of two-dimensional turbulence, *Phys. Fluids*, *I2(supplement)*, II240–II249, 1969.

Maddison, J., and D. Marshall, The Eliassen-Palm flux tensor, *J. Fluid Mech.*, *729*, 69–102, 2013.

Maltrud, M. E., and G. K. Vallis, Energy spectra and coherent structures in forced two-dimensional and beta-plane turbulence, *J. Fluid Mech.*, *228*, 321–342, 1991.

Manfroi, A. J., and W. R. Young, Slow evolution of zonal jets on the beta-plane, *J. Atmos. Sci.*, *56*, 784–800, 1999.

Marshall, J., E. Shuckburgh, H. Jones, and C. Hill, Estimates and implications of surface eddy diffusivity in the Southern Ocean derived from tracer transport, *J. Phys. Ocean.*, *36*(9), 1806–1821, 2006.

Marston, J. B., E. Conover, and T. Schneider, Statistics of an unstable barotropic jet from a cumulant expansion, *J. Atmos. Sci.*, *65*, 1955–1966, 2008.

Maximenko, N. A., O. V. Melnichenko, P. P. Niiler, and H. Sasaki, Stationary mesoscale jet-like features in the ocean, *Geophys. Res. Lett.*, *35*(8), L08,603, 2008.

Nozawa, T., and S. Yoden, Formation of zonal-band structure in forced two-dimensional turbulence on a rotating sphere, *Phys. Fluids*, *9*, 2081–2093, 1997.

O'Gorman, P. A., and T. Schneider, Recovery of atmospheric flow statistics in a general circulation model without nonlinear eddy-eddy interactions, *Geophys. Res. Lett.*, *34*(22), 2007.

O'Gorman, P. A., and T. Schneider, Weather-layer dynamics of baroclinic eddies and multiple jets in an idealized general circulation model, *J. Atmos. Sci.*, *65*(2), 524–535, 2008.

Orr, W. M. F., The stability or instability of the steady motions of a perfect liquid and of a viscous liquid. part I: A perfect liquid, in *Proceedings of the Royal Irish Academy. Section A: Mathematical and Physical Sciences*, vol. 27, pp. 9–68, JSTOR, 1907.

Panetta, L., Zonal jets in wide baroclinically unstable regions: persistence and scale selection, *J. Atmos. Sci.*, *50*, 2073–2106, 1993.

Parker, J. B., and J. A. Krommes, Zonal flow as pattern formation: Merging jets and the ultimate jet length scale, *arXiv preprint arXiv:1301.5059*, 2013.

Pedlosky, J., Geophysical fluid dynamics, *New York and Berlin, Springer-Verlag, 1982. 636 p.*, *1*, 1982.

Porco, C. C., et al., Cassini imaging of Jupiter's atmosphere, satellites, and rings, *Science*, *299*(5612), 1541–1547, 2003.

Prandtl, L., Bericht über untersuchungen zur ausgebildeten turbulenz, *Z. Angew. Math. Mech*, *5*(2), 136–139, 1925.

Rhines, P. B., Waves and turbulence on a beta-plane, *J. Fluid Mech.*, *69*, 417–443, 1975.

Rhines, P. B., and W. R. Young, Homogenization of potential vorticity in planetary gyres, *J. Fluid Mech.*, *122*, 347–367, 1982.

Rosen, G., General solution for perturbed plane Couette flow, *Phys. Fluids*, *14*, 2767–2769, 1971.

Salmon, R., *Lectures on Geophysical Fluid Dynamics*, xiii+379 pp., Oxford University Press, 1998.

Schneider, T., and J. Liu, Formation of jets and equatorial superrotation on Jupiter, *J. Atmos. Sci.*, *66*(3), 579–601, 2009.

Schneider, T., and C. C. Walker, Scaling laws and regime transitions of macroturbulence in dry atmospheres, *J. Atmos. Sci.*, *65*(7), 2153–2173, 2008.

Scott, R. K., and L. M. Polvani, Forced-dissipative shallow-water turbulence on the sphere and the atmospheric circulation of the giant planets, *J. Atmos. Sci.*, *64*, 3158–3176, 2007.

Shepherd, T. G., Time development of small disturbances to plane Couette flow, *J. Atmos. Sci.*, *42*, 1868–1871, 1985.

Showman, A. P., Numerical simulations of forced shallow-water turbulence: Effects of moist convection on large-scale circulation of Jupiter and Saturn., *J. Atmos. Sci.*, *64*, 3132–3157, 2007.

Showman, A. P., Y. Kaspi, and G. R. Flierl, Scaling laws for convection and jet speeds in the giant planets, *Icarus*, *211*(2), 1258–1273, 2011.

Smith, K. S., A local model for planetary atmospheres forced by small-scale convection, *J. Atmos. Sci.*, *61*, 1420–1433, 2004.

Smith, K. S., The geography of linear baroclinic instability in earth's oceans, *Journal of Marine Research*, *65*(5), 655–683, 2007.

Sokolov, S., and S. R. Rintoul, Multiple jets of the Antarctic Circumpolar Current south of Australia*, *J. Phys. Oceanogr.*, *37*(5), 1394–1412, 2007.

Srinivasan, K., and W. R. Young, Zonostrophic instability, *J. Atmos. Sci.*, *69*(5), 1633–1656, 2012.

Stammer, D., On eddy characteristics, eddy transports, and mean flow properties, *J. Phys. Oceanogr.*, *28*(4), 727–739, 1998.

Stewart, R., and R. Thomson, Re-examination of vorticity transfer theory, *Proceedings of the Royal Society of London. A. Mathematical and Physical Sciences*, *354*(1676), 1–8, 1977.

Thompson, A. F., Jet formation and evolution in baroclinic turbulence with simple topography, *J. Phys. Oceanogr.*, *40*(2), 257–278, 2010.

Thompson, A. F., and K. J. Richards, Low frequency variability of southern ocean jets, *Journal of Geophysical Research*, *116*(C9), C09,022, 2011.

Thomson, R. E., and R. Stewart, The balance and redistribution of potential vorticity within the ocean, *Dynamics of Atmospheres and Oceans*, *1*(4), 299–321, 1977.

Tobias, S., and J. Marston, Direct statistical simulation of out-of-equilibrium jets, *Phys. Rev. Lett.*, *110*(10), 104,502, 2013.

Tobias, S. M., K. Dagon, and J. B. Marston, Astrophysical fluid dynamics via direct statistical simulation, *Astrophysical J.*, *727*, 1–12, 2011.

Tsang, Y.-K., and W. R. Young, Energy-enstrophy stability of β-plane kolmogorov flow with drag, *Phys. Fluids*, *20*(8), 084,102–084,102, 2008.

Tulloch, R., J. Marshall, C. Hill, and K. S. Smith, Scales, growth rates, and spectral fluxes of baroclinic instability in the ocean, *J. Phys. Oceanogr.*, *41*(6), 1057–1076, 2011.

Tung, K. K., Initial-value problems for Rossby waves in a shear flow with critical level., *J. Fluid Mech.*, *133*, 443—469., 1983.

Vallis, G. K., *Atmospheric and oceanic fluid dynamics: fundamentals and large-scale circulation*, Cambridge University Press, 2006.

Vallis, G. K., and M. E. Maltrud, Generation of mean flow and jets on a beta plane and over topography, *J. Phys. Oceanogr.*, *23*, 1346–1362, 1993.

Vasavada, A. R., and A. P. Showman, Jovian atmospheric dynamics: an update after *galileo* and *cassini*, *Reports on Progress in Physics*, *68*, 1935–1996, 2005.

Welander, P., Lateral friction in the oceans as an effect of potential vorticity mixing, *Geophysical & Astrophysical Fluid Dynamics*, *5*(1), 173–189, 1973.

Whitehead, J. A., Mean flow generated by circulation on a beta-plane: An analogy with the moving flame experiment, *Tellus*, *27*, 358–363, 1975.

Williams, G. P., Planetary circulations: 1. Barotropic representation of Jovian and terrestrial turbulence, *J. Atmos. Sci.*, *35*, 1399–1426, 1978.

Williams, G. P., Jovian dynamics. Part iii: Multiple, migrating, and equatorial jets, *J. Atmos. Sci.*, *60*(10), 1270–1296, 2003.